DESIGN, ANALYSIS, OPERATION, AND ADVANCED CONTROL OF HYBRID RENEWABLE ENERGY SYSTEMS

by

Zachary S. Whiteman

A dissertation submitted to the Faculty of the University of Delaware in partial fulfillment of the requirements for the degree of Doctor of Philosophy in Chemical Engineering

Summer 2015

DESIGN, ANALYSIS, OPERATION, AND ADVANCED CONTROL OF HYBRID RENEWABLE ENERGY SYSTEMS

by

Zachary S. Whiteman

Approved: _____
Abraham M. Lenhoff, Ph.D.
Chair of the Department of Chemical and Biomolecular Engineering

Approved: _____
Babatunde A. Ogunnaike, Ph.D.
Dean of the College of Engineering

Approved: _____
James G. Richards, Ph.D.
Vice Provost for Graduate and Professional Education

I certify that I have read this dissertation and that in my opinion it meets the academic and professional standard required by the University as a dissertation for the degree of Doctor of Philosophy.

Signed: _____

Babatunde A. Ogunnaike, Ph.D.
Professor in charge of dissertation

I certify that I have read this dissertation and that in my opinion it meets the academic and professional standard required by the University as a dissertation for the degree of Doctor of Philosophy.

Signed: _____

Michael T. Klein, Ph.D.
Member of dissertation committee

I certify that I have read this dissertation and that in my opinion it meets the academic and professional standard required by the University as a dissertation for the degree of Doctor of Philosophy.

Signed: _____

Raul F. Lobo, Ph.D.
Member of dissertation committee

I certify that I have read this dissertation and that in my opinion it meets the academic and professional standard required by the University as a dissertation for the degree of Doctor of Philosophy.

Signed: _____

Ajay K. Prasad, Ph.D.
Member of dissertation committee

I certify that I have read this dissertation and that in my opinion it meets the academic and professional standard required by the University as a dissertation for the degree of Doctor of Philosophy.

Signed: _____

Stephens Thé, Ph.D.
Member of dissertation committee

ACKNOWLEDGMENTS

This dissertation was a collaborative endeavor and could not have been completed without the assistance provided by many individuals. First and foremost, I would like to thank my advisor, Prof. Babatunde Ogunnaike. His guidance, advice, and unparalleled knowledge in the field of process systems engineering undoubtedly improved my skills as an engineer and helped produce this dissertation.

I would also like to thank my research group members: Dr. Melissa St. Amand, Dr. Jacob McGill, Dr. Qian Gou, Chia-Hung Tsai, Devesh Radhakrishnan, Dan Cook, James Park, and Robert Lovelett. Each provided an outstanding source of constructive feedback and support throughout my tenure at the University of Delaware.

Prof. Ajay Prasad, Piyush Bubna, Doug Brunner, Jingliang Zhang, Prof. Arun Tangirala, Prof. Daniel Lees, Dr. Stephens Thé, Dr. Madhu Annapragada, Andrew McDermott, and Steven Hegedus each furnished strong technical assistance during various parts of this dissertation.

My undergraduate students, Ki Heok Chae, Justin Kurian, and Kyle Tucker, must also be acknowledged for their notable contributions towards this dissertation.

I thank my family for their love and support throughout my academic career. Finally, I dedicate this dissertation to Lizzy for her continuous encouragement and inspiration during the course of this work.

TABLE OF CONTENTS

LIST OF TABLES

LIST OF FIGURES

ABSTRACT

Because using non-renewable energy systems (e.g., coal-powered co-generation power plants) to generate electricity is an unsustainable, environmentally hazardous practice, it is important to develop cost-effective and reliable renewable energy systems, such as photovoltaics (PVs), wind turbines (WTs), and fuel cells (FCs). Non-renewable energy systems, however, are currently less expensive than individual renewable energy systems (IRESs). Furthermore, IRESs based on intermittent natural resources (e.g., solar irradiance and wind) are incapable of meeting continuous energy demands. Such shortcomings can be mitigated by judiciously combining two or more complementary IRESs to form a hybrid renewable energy system (HRES). Although previous research efforts focused on the design, operation, and control of HRESs has proven useful, no prior HRES research endeavor has taken a systematic and comprehensive approach towards establishing guidelines by which HRESs should be designed, operated, and controlled. The overall goal of this dissertation, therefore, is to establish the principles governing the design, operation, and control of HRESs resulting in cost-effective and reliable energy solutions for stationary and mobile applications.

The first empirical part of this dissertation focuses on HRES equipment selection and sizing using an economic and feasibility analysis. We determined that HRES components and their sizes should be rationally selected using knowledge of component costs, availability of renewable energy resources, and expected power demands of the application. To demonstrate this statement, we ascertained the economically preferred and feasible renewable energy system types and sizes for a range of average annual wind speed, average annual solar irradiance, power demand

and minimum renewable fraction. We found that under some combinations of these variables HRESs are less expensive than IRESs and grid-supplied energy. This result has a significant implication for renewable energy systems becoming increasingly ubiquitous.

After HRES type and sizes are selected, it is necessary to determined how the components are arranged and what control systems are best for coordinating the entire system to meet a set of operating objectives (typically satisfy a power demand while storing excess power for later use). This was demonstrated by way of a case study involving the design, control, and economics of a University of Delaware FC/battery bus retrofitted with a roof-installed PV array. The preferred arrangement of HRES components is the FC in series with the battery (the FC is committed to maintaining a desired battery state of charge (SOC) while the battery meets the majority of the bus power demand) while the PV array is used to assist the battery in meeting the bus power demand, with excess PV power being used to charge the battery. Simulation results indicate that under a variety of operating conditions, a PID control strategy is best for enabling the bus to satisfy required power demands and maintain a desired battery SOC. An economic analysis of the PV investment necessary to realize the HRES design objectives indicates that the investment will pay for itself in Newark, DE, establishing the economic viability of the proposed addition of a PV array to the existing University of Delaware FC/battery bus.

Although the performance of standard controllers for HRESs is generally satisfactory, operating objectives can be met more reliably and efficiently when information-rich data is used to coordinate HRES component. Two such data-driven control paradigms were developed in separate case studies. In the first case study, we

developed and evaluated a method for reconfiguration of control loops in decentralized control schemes using directed spectral decomposition of collected process data. This technique was applied to a stirred mixing tank process and was shown to improve control performance under changing operating conditions. The second case study, which involved data-driven centralized control, establishes a method for adaptive data-driven MPC of a PV/WT/FC/battery/electrolyzer HRES for a single-family home using measured disturbance prediction and model adaptation. This procedure was shown to enable the HRES to better track a power demand setpoint, resulting in increased system reliability and efficiency.

Finally, a PV/WT/battery HRES called an OMNi-Charger, which is intended for small-scale (~1 W) remote power applications) was experimentally validated under varying power demand, wind speed, and solar irradiance during controlled and field tests. The OMNi-Charger controller—a simple state controller that enacts a pre-specified control action depending on the current state or operating conditions of the system—was shown to enable the OMNi-Charger to meet varying power demands nearly instantaneously and consistently despite rapid and unknown fluctuations in wind speed and solar irradiance. Although the OMNi-Charger warrants some future investigation, the device should prove useful as a cell phone charging station or a power source for lighted ocean buoys.

Chapter 1

INTRODUCTION TO HYBRID RENEWABLE ENERGY SYSTEMS

1.1 Introduction

In the year 2014, the Earth's human population consumed an all-time high of 580 quadrillion Btu of energy and energy consumption is projected to increase by ~40% over the next 25 years [1]. The rise in global energy demand is expected to be satisfied not only using traditional, non-renewable energy resources, (e.g., coal, oil, natural gas, and nuclear fuel) but also by renewable energy resources (e.g., solar irradiance and wind). In fact, by 2040, renewable energy production is expected to increase by ~80% while supplying ~15% of the world's energy demand (Fig. 1.1). On the contrary, energy production via oil and coal are each only expected to increase by ~30% while supplying ~3% less of the world's energy demand than they do today.

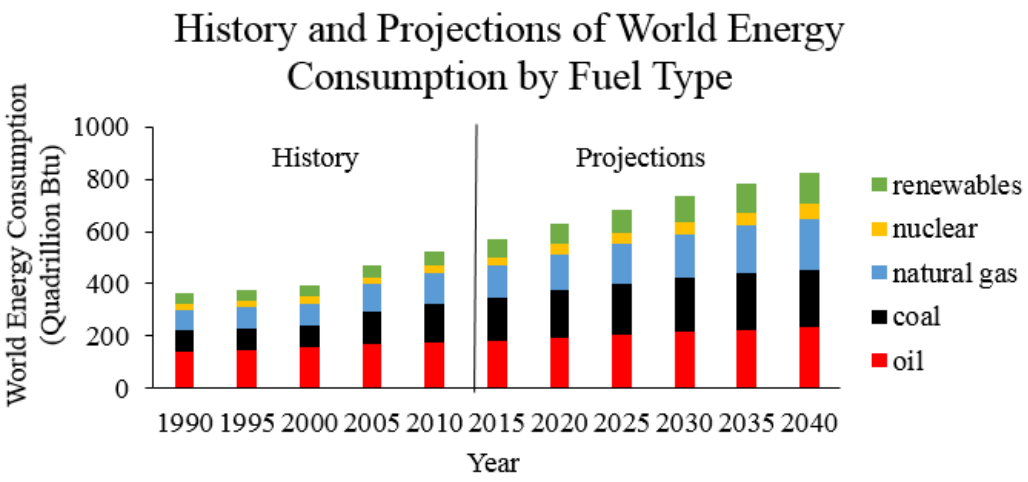

Figure 1.1 History and projections of world energy consumption by fuel type (renewables, nuclear, natural gas, coal, and oil). Consistent growth in energy consumption is expected through 2040, with renewables accounting for ~15% of energy production by 2040.

The shift in future energy resource use is partially propelled by the inherent disadvantages of non-renewable energy resources. The cost of oil, coal, natural gas, and nuclear fuel (namely, uranium oxide), for instance, is expected to increase by an average of ~70% over the next 10 years, with costs continuing to rise further into the future (Fig. 1.2) [2,3]. Additionally, non-renewable energy resources are a major contributor towards greenhouse gas emissions (e.g., CO_2, NO_x, SO_x, etc.), which are responsible for the Earth's climate change to some extent [4]. Lastly, it is well-known that the supply of non-renewable energy reserves is limited and continues to diminish.

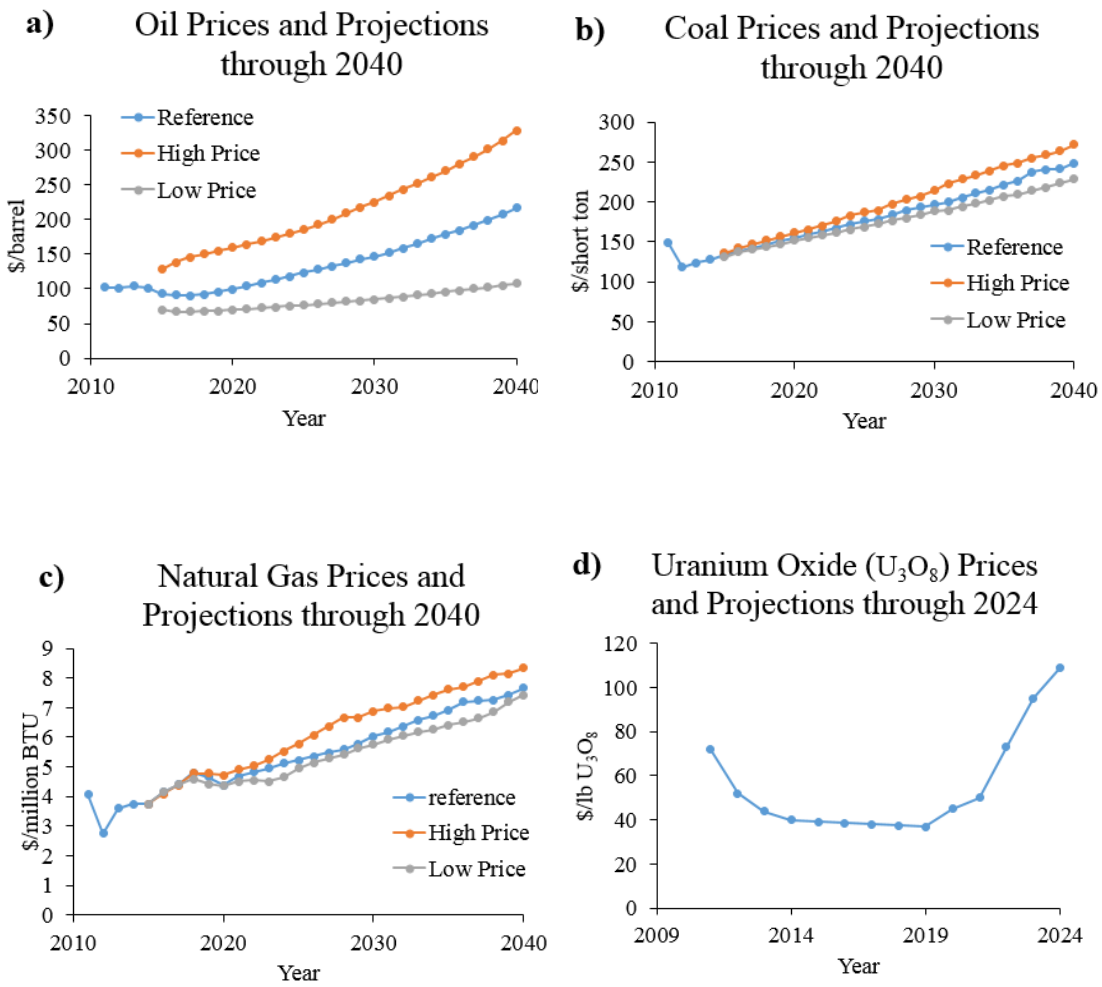

Figure 1.2 Historical and projected prices for various non-renewable fuel types: **a)** oil; **b)** coal; **c)** natural gas; and **d)** uranium oxide. The reference case (blue line), high price projection (orange line), and low price projection (grey line) are shown for oil, coal, and natural gas. Only reference case projections are available for uranium oxide. Note that the price of each non-renewable fuel is expected to increase over the next several decades.

Another contributing factor towards the expected increase in use of renewables is the advantages of systems that harness renewable energy resources. For example, photovoltaics (PVs) and wind turbines (WTs) are projected to be ~20% cheaper in 10 years than they are today (Fig. 1.3a and 1.3b) [5–8]. The cost of hydrogen-powered

fuel cells (FCs) is also expected to reduce by as much as 25% by 2017 (Fig. 1.3c) [9]. Furthermore, low-emission renewable energy systems, such as PVs, WTs, and FCs, produce zero greenhouse gas emissions and their energy resources are practically limitless.

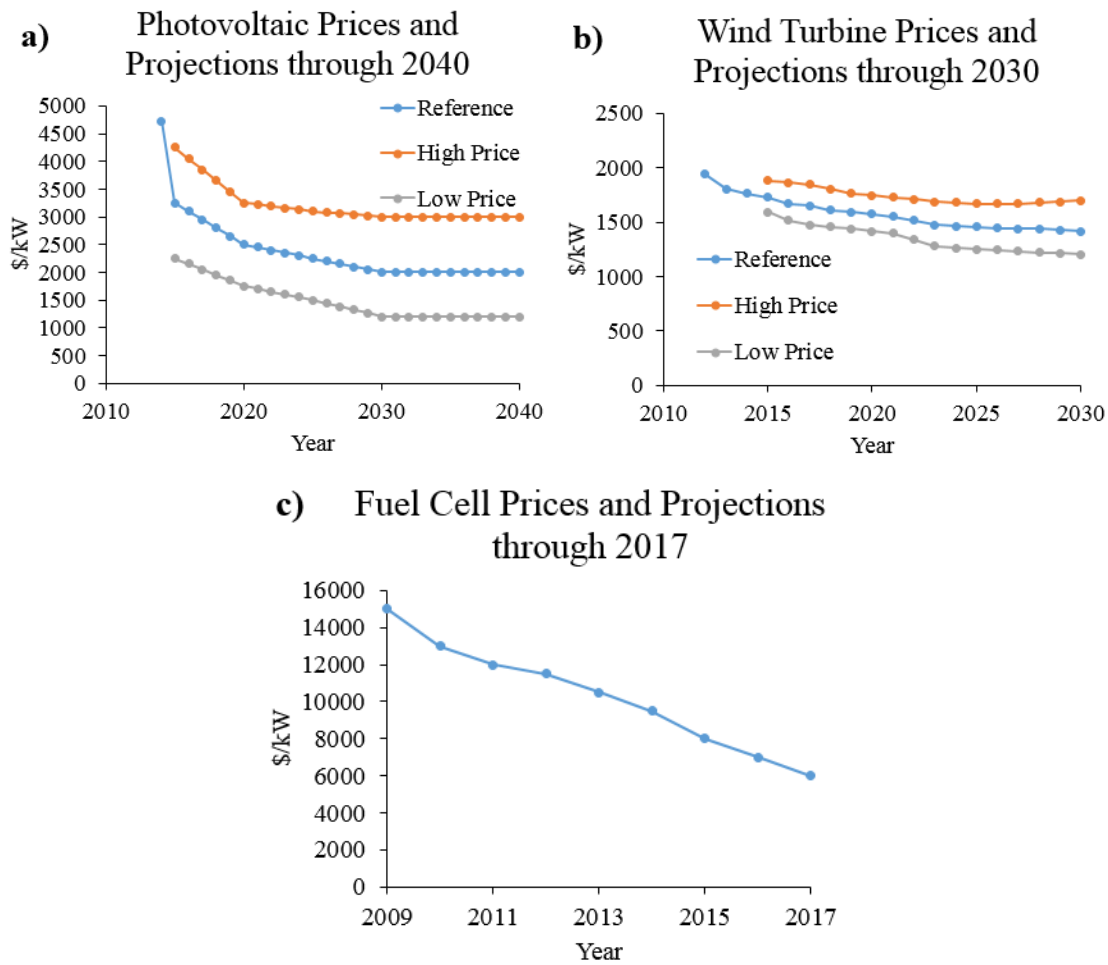

Figure 1.3 Historical and projected prices for various renewable energy systems: **a)** photovoltaics (PVs); **b)** wind turbines (WTs); and **c)** fuel cells (FCs). The reference case (blue line), high price projection (orange line), and low price projection (grey line) are shown for PVs and WTs. Only reference case projections are available for FCs. Note that the price of PVs, WTs, and FCs is expected to diminish in the coming years.

Despite the advantages of low-emission renewable energy systems, they are not ubiquitous for two reasons: their prohibitively high cost and intermittent power production. Still, these problems may be alleviated by taking advantage of the complementary nature of certain renewable energy systems. Consider first the PV and the WT. As a stand-alone systems, PVs are relatively expensive, and with low energy conversion efficiency, as opposed to WTs, which are comparatively less expensive and with relatively higher energy conversion efficiency. However, even though availability of useful sunlight is limited to approximately 5-8 hours a day, solar radiation has the highest power density of all renewable energy sources and is also more consistent than the random, fluctuating and capricious nature of wind; however, wind is not limited to only a few hours a day. The two sources are therefore clearly complementary.

Similar arguments apply to FCs, whose primary advantages include high efficiency, near-zero emissions, and virtual noiselessness. However, they require fuels such as hydrogen, one of the cleanest and lightest fuels, and most efficient energy carriers, but one that does not exist naturally in sufficient amounts, and must therefore be produced from primary energy sources—making power generation via FCs expensive. Nevertheless, power from a PV or a WT can be used to produce hydrogen from water electrolyzers, and stored in a tank for later use in the FC.

Observe therefore that because they involve multiple renewable resources, a hybrid renewable energy system (HRES)—a system consisting of two or more renewable energy systems utilized simultaneously to meet a power demand—may represent a cheaper and more dependable alternative to single stand-alone renewable energy systems. An example HRES is the PV/WT/FC/battery/electrolyzer system

shown schematically in Fig. 1.4. Renewable energy resources of solar irradiance, wind, and hydrogen are converted to electrical power via a PV, WT, and FC, respectively. The electrical power is used to meet a required power demand. A battery is used to store excess power for later use, or to provide supplemental power. The electrolyzer can store excess power as hydrogen for the FC.

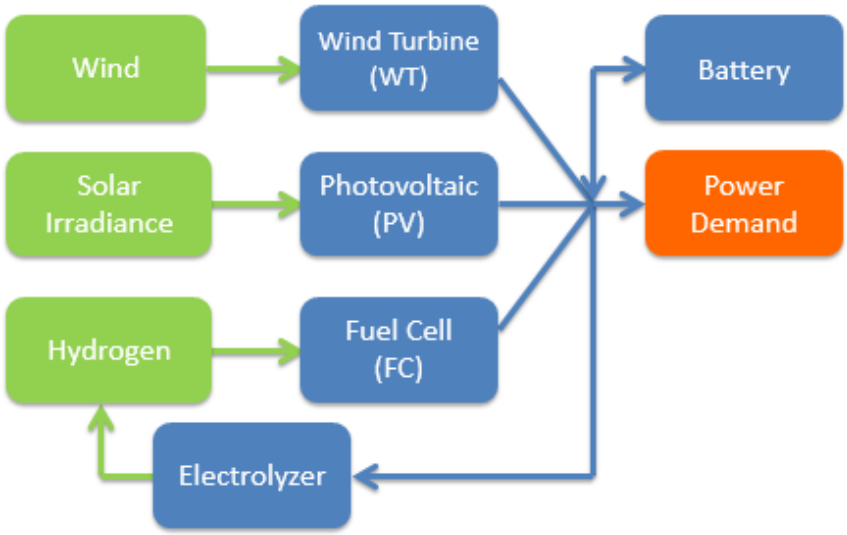

Figure 1.4 PV/WT/FC/battery/electrolyzer HRES schematic. Block color representation: green, renewable energy resource; blue, HRES component; and orange, power demand. Line color representation: green, renewable energy resource flow; and blue, electrical power.

Before a HRES can be physically realized, however, the following tasks must be completed: 1) select apposite HRES components and sizes for the desired end-use; 2) arrange the selected HRES components appropriately; and 3) design a control strategy for the HRES that maximizes system efficiency and enables the HRES to meet its operating objectives (i.e., satisfy power demands and store excess energy).

Previous research efforts in accomplishing these tasks have been sporadic, with narrow focus on a single HRES type or application. For example, HRES component selection and sizing has been completed for hybrid energy systems consisting of various PV, WT, FC, electrolyzer, battery, and diesel engine combinations with applications such as a radio repeater station and small-scale residences in Sri Lanka, India, Alaska, Egypt, Jordan, Thailand, Newfoundland, the Pacific Northwest, New England, and Saudi Arabia [10–20]. In addition, state control, PID control, and model predictive control (MPC) have each been separately designed and evaluated previously for various HRESs [17,21–27]. Despite these efforts, no prior HRES research endeavor has taken a systematic approach towards developing and demonstrating guidelines by which HRESs should be designed, operated, and controlled.

1.2 Dissertation Goal and Scope

Given the lack of a comprehensive study on HRESs, the overall goal of this dissertation is to establish the principles governing the design, operation, and advanced control of HRESs resulting is cost-effective and reliable energy solutions for stationary and mobile applications. These principles will be established by answering the following questions:

1. *How should HRES components and their sizes be selected to meet specified operating objectives?*
2. *How should HRESs be designed to meet the operating objectives consistently?*
3. *What types of control strategies are best for meeting a HRES's operating objectives?*

4. *Can data collected from a HRES be used to meet its operating objectives more effectively?*

It is important to note that in answering these questions via demonstrative case studies, we are only considering low-emission renewable energy system components in HRESs. In this context, low-emission is to be understood as emitting little or no greenhouse gases. Thus, biomass, although renewable, will not be considered in this dissertation as it is not low-emission. The components considered here are the PV, WT, FC, battery, and electrolyzer. Each of these renewable energy and auxiliary systems is described in greater detail in the following section.

1.3 Renewable Energy System Background

1.3.1 Photovoltaics

Solar cells or photovoltaic (PV) cells are semiconductor materials that exhibit the photoelectric effect: a phenomena by which electrical energy is generated when photons in sunlight bombard a semiconductor material. A PV cell typically consists of a back electrical contact, the semiconductor material, an anti-reflective protective coating that allows light to pass through to the material, and a front electrical contact (Fig. 1.5). PV cells are usually connected in series to form a PV module. PV modules are then connected together to form a PV array (Fig. 1.6).

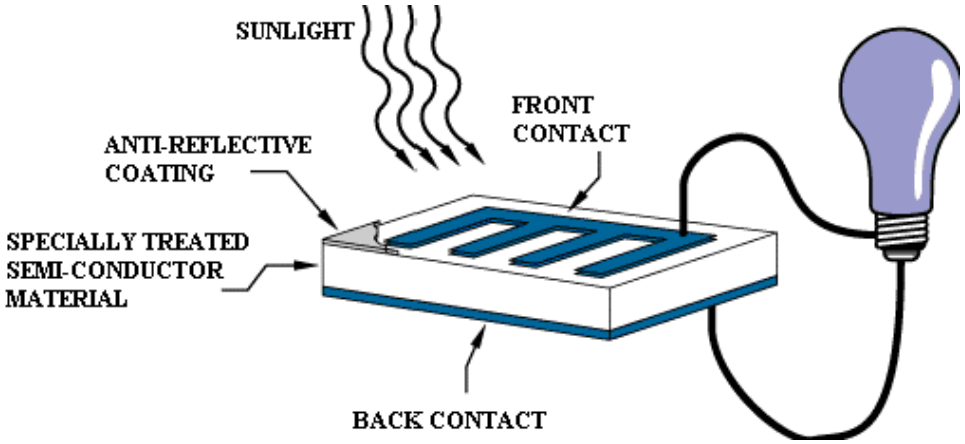

Figure 1.5 Illustration of a photovoltaic (PV) cell. The PV cell, which accepts photons in light and produces electricity, consists of a back contact, a semiconductor material, an anti-reflective coating, and a front contact. In this case, the cell provides electricity for a lightbulb [28].

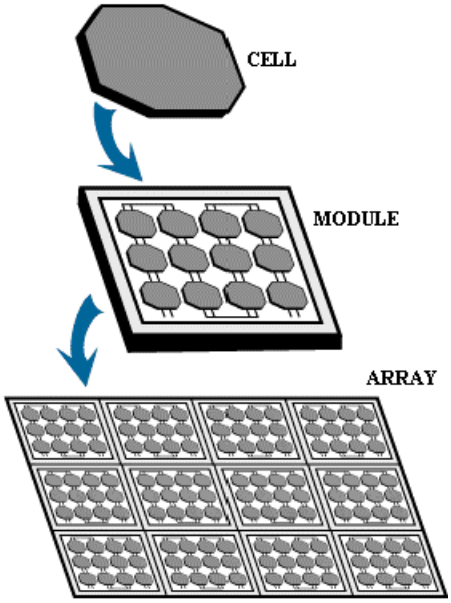

Figure 1.6 Illustration of a PV cell, array, and module. PV cells are used to make PV modules, which are in turn used to make a PV arrays [28].

There are two classes of semiconductor materials used for PVs: thin films and crystalline silicon (Fig. 1.7). Thin film PV materials are a relatively new technology and are acclaimed for their low material usage and low cost of production. Examples of thin film PV materials are amorphous silicon (a-Si), cadmium telluride (CdTe), copper indium gallium selenide (CI(G)S), nanocrystalline silicon (μc-Si), and dye-sensitized (DS), having efficiencies between 2% and 11%. On the contrary, crystalline silicon PV technology has existed for over 60 years and is used in over 90% of currently installed PV systems. Crystalline silicon PVs are composed of either monocrystalline or multicrystalline silicon, with efficiencies ranging from 11% to 19%.

Technology	Thin Film					Crystalline Silicon	
	(a-Si)	(CdTe)	CI(G)S	a-Si/ μc-Si	Dye s. cells	Mono	Multi
							
Cell efficiency	4-8%	10-11%	7-11%	7-9%	2-4% (LAB)	13-19%	11-15%
Module efficiency							

Figure 1.7 Table showing the various types of PV modules available and their typical efficiencies [29].

Regardless of the type of semiconductor material used for a PV array, the array requires a maximum power point tracking (MPPT) technique to extract as much usable power from the device as possible. As shown in Fig. 1.8, the maximum power

delivered from a PV array depends on the incident solar irradiance and the PV temperature. A PV MPPT technique aims to adjust the PV array voltage using a DC/DC converter so that the maximum power points in Fig. 1.9 are realized. A number of PV MPPT techniques exist, most notably the short-current pulse, perturb & observe, and incremental conductance methods, each of which are described in detail in [30].

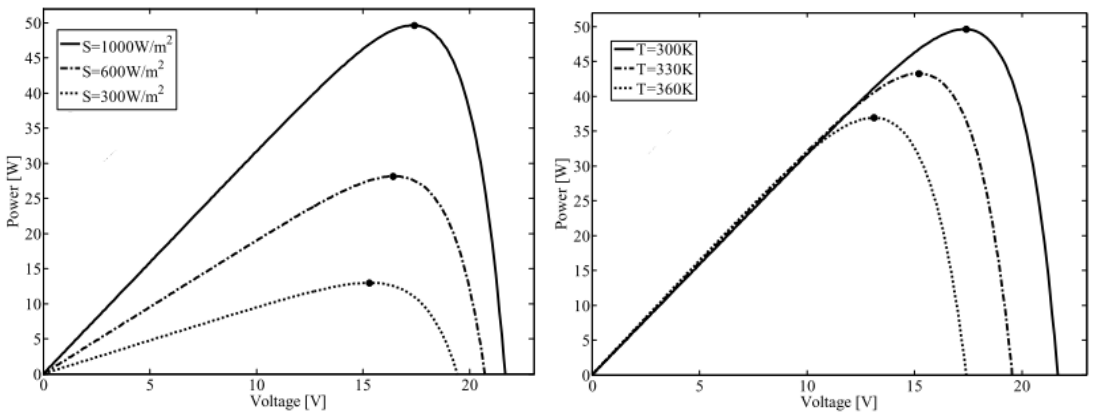

Figure 1.9 Power versus voltage for varying solar irradiance (S) (left) and PV cell temperature (T) (right). For a given S and T combination, there exists a PV voltage corresponding to maximum power output (black dots) [30].

1.3.2 Wind Turbines

A wind turbine (WT) is a device used to convert the kinetic energy from wind into electrical energy (Fig. 1.10). When wind causes the blades of a WT to turn, the kinetic energy of wind is transferred into rotational mechanical energy along the WTs low-speed shaft. The rotational mechanical energy is then transferred to the high-speed shaft via a gear box. Finally, the high-speed shaft rotates an electrical generator, thereby producing electrical energy that is carried down the tower.

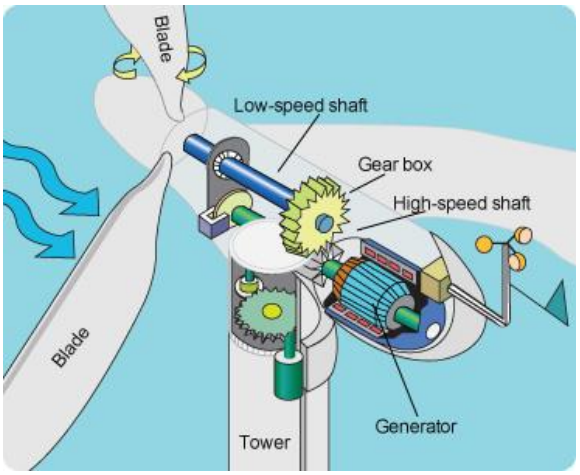

Figure 1.10 Illustration of a wind turbine. Incident wind (blue arrows) spin the blades, which causes the low-speed shaft (blue cylinder) to rotate. The rotation is transferred to the high-speed shaft (green cylinder) using a gear box. The high-speed shaft rotation causes the generator to rotate, which produces electricity [31].

The two most widely used types of WTs are horizontal axis wind turbines (HAWTs) and vertical axis wind turbines (VAWTs) (Fig. 1.11). HAWTs typically either have two or three blades and currently represent 90% of the WT market share due to their higher power efficiency over VAWTs (Fig. 1.12) [32]. Although used less frequently, VAWTs, which typically have Savonius or Darreius blade designs, are making a resurgence because they have several advantages over HAWT. More specifically, VAWTs have fewer parts, are safer for maintenance workers, are omni-directional, i.e., they can accept wind from any direction, can be efficiently scaled down, and emit less noise [33,34].

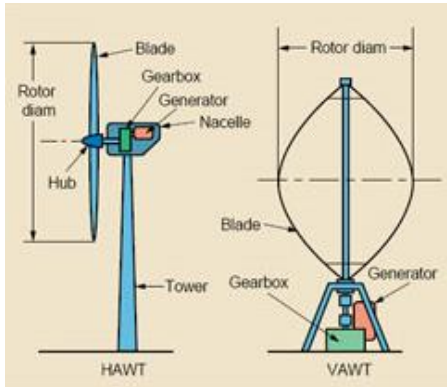

Figure 1.11 Illustration of a horizontal axis wind turbine (HAWT) and a vertical axis wind turbine (VAWT). A HAWT's rotational shaft is parallel to the ground while a VAWT's rotational shaft is perpendicular to the ground [35].

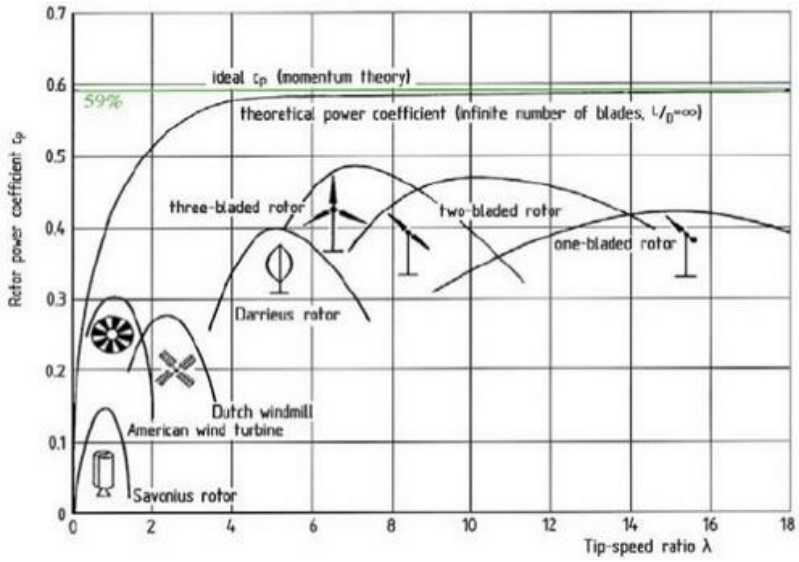

Figure 1.12 Rotor power coefficient (proportional to power efficiency) versus tip-speed ratio (ratio of rotor rotational speed to wind speed) for various wind turbine designs. The green line represents the Betz limit of 0.59. The three-bladed HAWT, which is most common, has the highest power efficiency of any existing WT technology. The VAWT designs (Darrieus and Savonius) are much less efficient [36].

In order for a WT to operate reliably, it must include a MPPT and blade pitch control scheme. For WTs, the maximum power point depends on the tip-speed ratio (λ) and the blade pitch angle (θ) (Fig. 1.13). The tip-speed ratio is defined as:

$$\lambda = {}^{\omega r}/_{v} \tag{1.1}$$

where ω is the rotor angular speed, r is the rotor radius, and v is the wind speed. Therefore, for a given v and θ, there exists a ω that results in a maximum WT power coefficient (Cp, referred to in Fig. 1.12 as the rotor power coefficient). The blade pitch angle is controlled such that the blade rotational speed, and hence WT power, is reduced to safe levels when wind speed is greater than the WT's rated wind speed.

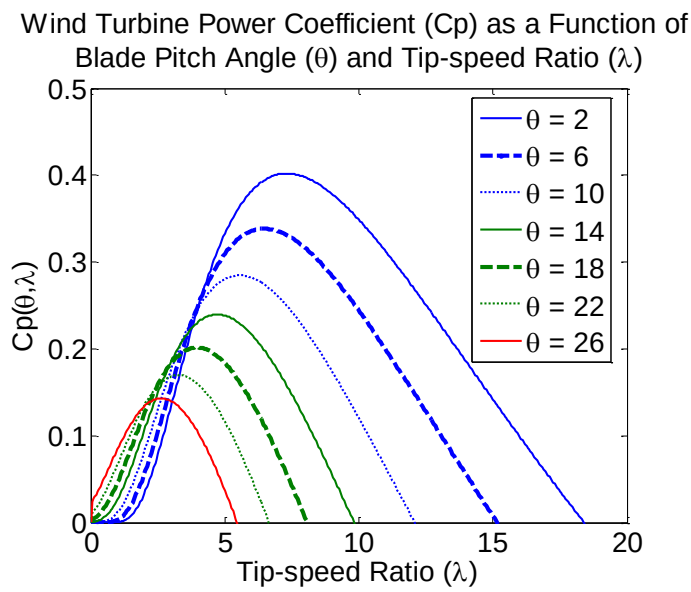

Figure 1.13 Plot of WT power coefficient (Cp) versus tip-speed ratio (λ) for varying blade pitch angles (θ). MPPT is necessary because for a given θ there exists a λ that yields a maximum Cp. Also note that as θ increases, Cp decreases—a characteristic that is exploited when the WT power output must be limited at high wind speeds.

1.3.3 Fuel Cells

A fuel cell (FC) is a device used to convert chemical energy to electrical energy. A FC's chemical reactants are commonly hydrogen and oxygen and produce water and electricity as shown below:

$$\text{Anode: } 2H_2 \rightarrow 4H^+ + 4e^-, \tag{1.2a}$$

$$\text{Cathode: } O_2 + 4H^+ + 4e^- \rightarrow 2H_2O, \tag{1.2b}$$

where the anode is the location of the hydrogen oxidation reaction (HOR) and the cathode is the location of the oxygen reduction reaction (ORR). In an acidic FC (i.e., a FC in which protons are conducted across the electrolyte), hydrogen enters a gas channel adjacent to the anode, which is responsible for conducting electrons through a circuit (Fig. 1.14). The hydrogen is decomposed into electrons and protons at a catalyst layer. The resulting electrons are passed through an external circuit while the protons are then conducted along an electrolyte to the cathode. At the cathode, the protons react with oxygen and incoming electrons from the closed external circuit on a catalyst to produce water.

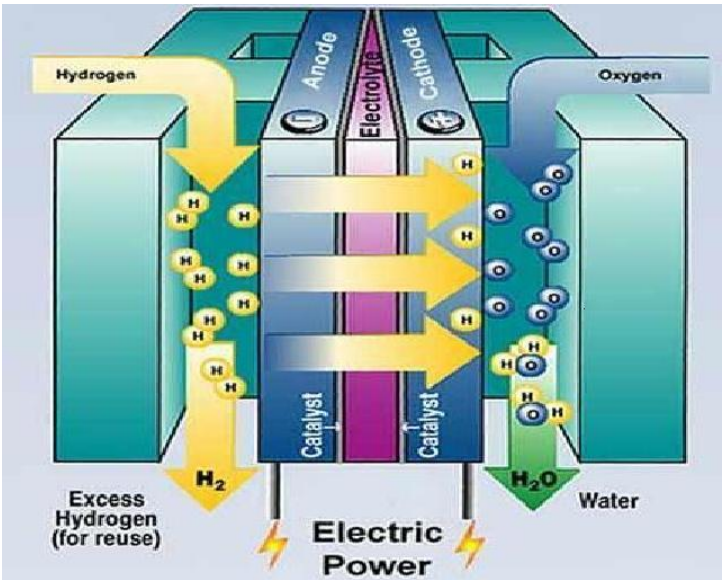

Figure 1.14 Diagram of an acid electrolyte fuel cell using hydrogen and oxygen to produce water and electric power. Protons are conducted across the electrolyte from the anode to the cathode. A catalyst is used to reduce the electrochemical activation energy at the electrolyte/anode and electrolyte/cathode interfaces [37].

The different FC types and their corresponding abbreviations, electrochemical reactions, and typical operating temperatures are provided in Fig. 1.15. The most common FC types are the polymer electrolyte membrane or proton exchange membrane (PEM) FC and the solid oxide FC (SOFC). The PEMFC is typically used for portable (5 W to 20 kW), automotive (1 kW to 100 kW), and stationary (0.5 kW to 400 kW) applications, while the SOFC is used only for stationary applications [38].

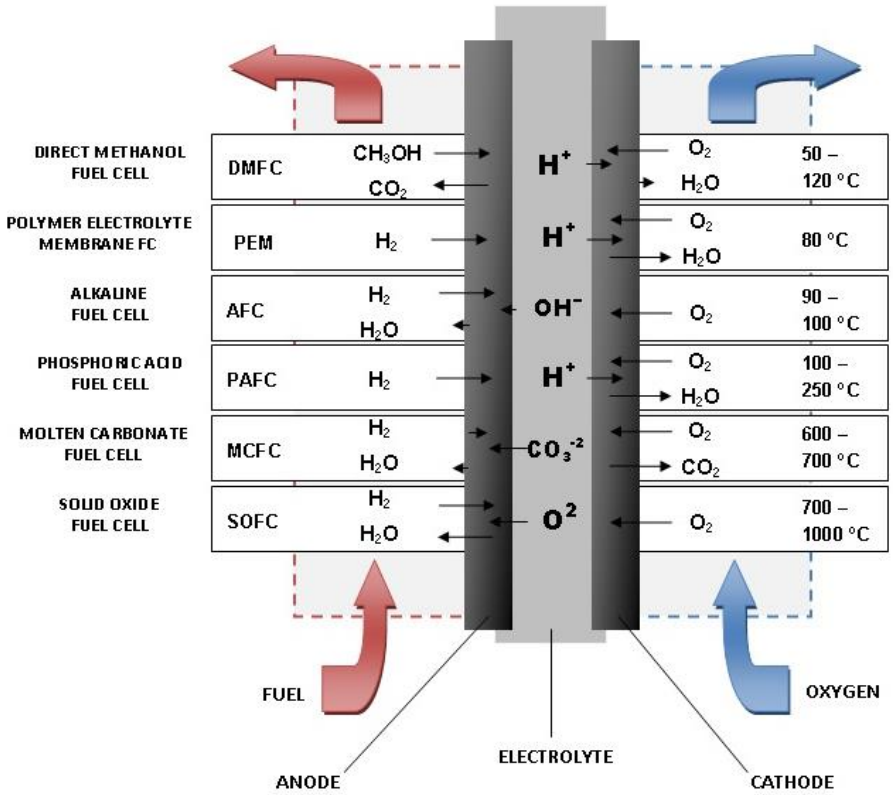

Figure 1.15 Illustration of the different FC types and their abbreviations, electrochemical reactions, and typical operating temperatures.

The PEMFC in particular is sensitive to changes in temperature, humidity, and the excess oxygen ratio[1]. Hence, these variables are often controlled to their desired values. The desired PEMFC operating temperature is often between 70°C - 80°C and is kept within this range using a heat exchanger. If the temperature is below this range, the thermodynamic efficiency of the FC is limited, whereas if the temperature is above this range, the FC membrane may dry out. When the membrane is too dry, proton

[1] The excess oxygen ratio is defined as the ratio between the oxygen supplied and the oxygen reacted in the cathode.

conductivity across the electrolyte decreases and FC power output is reduced [39]. The humidity of a PEMFC should be kept around 100% using a humidifier. If the humidity drops much below 100%, the FC membrane dries out. However, if the humidity is much higher than 100% the anode and cathode may flood, reducing the available surface area for reactant gases to participate in the electrochemical reactions shown in Eq. 1.2a and 1.2b [39]. The excess oxygen ratio is usually maintained around 2 using an air compressor. By delivering twice as much air to the cathode than is required, air is well-circulated in the cathode, thereby reducing stagnant film growth that can hinder the ORR. If the excess oxygen ratio drops below 1, then oxygen starvation occurs near the cathode exhaust, which decreases the FC lifetime and limist the FC durability [40].

1.3.4 Batteries

A battery is a device that can store electrical energy as chemical energy and vice versa. The discharge and charge operation of a battery is shown in Fig. 1.16. During the discharge operation, the battery's anodic material undergoes oxidation using the electrolyte, thereby creating electrons and cations. The electrons travel through an external circuit while the cations pass through a separator towards the cathode. The cathodic material undergoes reduction using the cations, electrons, and electrolyte, and, in doing so, the electrical circuit is completed. The charging operation is the exact opposite, with an external power source being used to force cations and electrons to react and form the anodic material at the anode.

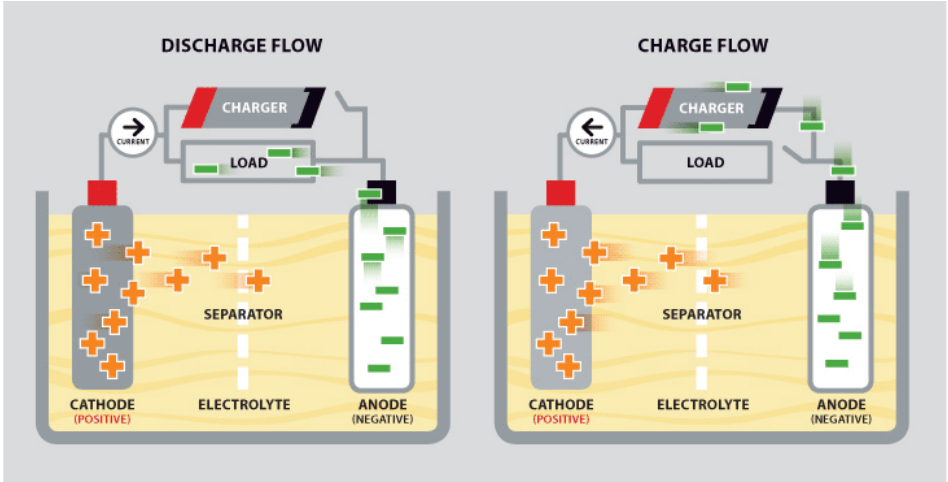

Figure 1.16 Illustration of battery discharge (left) and charge (right) operation. During the discharge operation, the anodic material reacts with an electrolyte to produce electrons (green minus signs) and cations (orange plus signs). The cations pass through a separator and react with the cathodic material and electrons to complete the circuit. The charge operation is the exact opposite [41].

Although there are many types of batteries available, the three types used in this dissertation are the lead-acid battery, the nickel cadmium (NiCd) battery, and the lithium iron phosphate ($LiFePO_4$) battery. The lead-acid battery electrochemical reactions are as follows:

$$\text{Anode: } Pb(s) + HSO_4^-(aq) \rightarrow PbSO_4(s) + H^+(aq) + 2e^-, \quad (1.3a)$$

$$\text{Cathode: } PbO_2(s) + HSO_4^-(aq) + 3H^+ + 2e^- \rightarrow PbSO_4(s) + 2H_2O. \quad (1.3b)$$

Lead-acid batteries are excellent for stationary HRES applications because they are very heavy but can be regularly discharged by as much as 80% without significant lifetime degradation [42]. This is an important characteristic since PV and WT power may be readily available or non-existent for long periods of time. The NiCd battery, on the other hand, is better suited for mobile HRES applications since it is much

lighter and has a higher energy density than lead-acid batteries [43]. The NiCd battery electrochemical reactions are given by:

$$\text{Anode: } Cd(s) + 2OH^-(aq) \rightarrow Cd(OH)_2(s) + 2e^-, \tag{1.4a}$$

$$\text{Cathode: } 2NiO(OH)(s) + 2H_2O + 2e^- \rightarrow 2Ni(OH)_2(s) + 2OH^-(aq). \tag{1.4b}$$

The $LiFePO_4$ battery is a recently developed technology having the following electrochemical reactions:

$$\text{Anode: } LiFePO_4(s) \rightarrow Li^+ + FePO_4(s) + e^-, \tag{1.5a}$$

$$\text{Cathode: } Li^+ + e^- + 6C(s) \rightarrow LiC_6(s). \tag{1.5b}$$

where the cathode material is composed of graphite (carbon). Due to its high specific energy, energy density, and cycle durability, $LiFePO_4$ batteries have the potential to replace both lead-acid and NiCd batteries. However, $LiFePO_4$ batteries remain more expensive than traditional battery technologies.

1.3.5 Electrolyzers

An electrolyzer is a reverse FC whereby electricity is used to split water into oxygen and hydrogen at the anode and cathode, respectively (Fig. 1.17). A PEM electrolyzer, the most common type of electrolyzer, has the following electrochemical reactions:

$$\text{Anode: } 2H_2O \rightarrow 4H^+ + O_2 + 4e^-, \tag{1.4a}$$

$$\text{Cathode: } 4H^+ + 4e^- \rightarrow 2H_2. \tag{1.4b}$$

A PEM electrolyzer's operating temperature can range from 20°C to 100°C, but it is most often maintained between 30°C and 50°C using a heat exchanger [44].

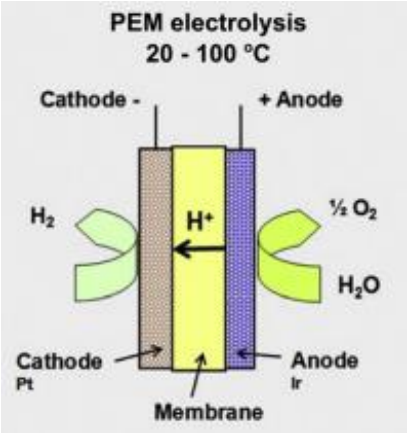

Figure 1.17 Illustration of PEM electrolysis. Water is split into protons, oxygen, and electrons at the anode using an iridium catalyst. Protons then travel across a membrane and combine with electrons on a platinum catalyst at the cathode to form hydrogen [45].

1.3.6 Hydrogen Storage

After hydrogen is produced from an electrolyzer, it must be stored for later use by a FC. The four existing techniques for storing hydrogen are pressurized hydrogen, liquid hydrogen, physisorption, and chemisorption. Physisorption of hydrogen can occur with carbon while chemisorption of hydrogen can occur with metal hydrides and complex hydrides. Among these techniques, pressurized hydrogen is perhaps the most well-developed. Currently, pressurized hydrogen is widely used because it is cheap and can operate at room temperature. The downside of pressurized hydrogen is that it has substantially lower volumetric and gravimetric hydrogen density than any other technique (Fig. 1.18). However, many other techniques are more expensive and may require temperatures in the range of 20 K to 680 K. Detailed descriptions of each technique are described in [46].

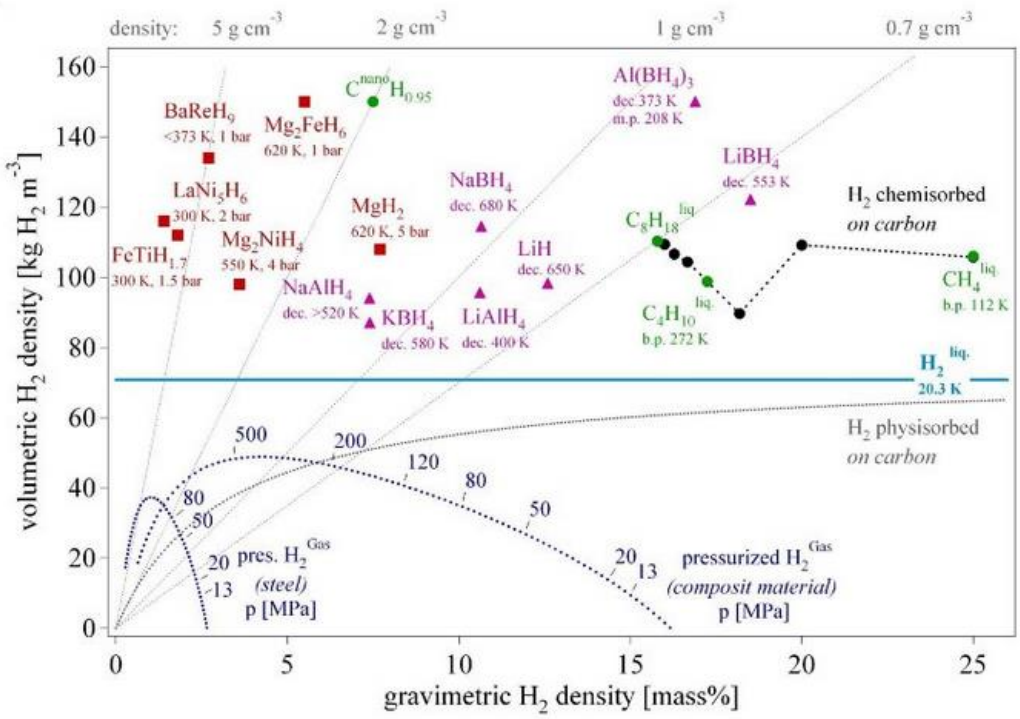

Figure 1.18 Plot of volumetric hydrogen density versus gravimetric hydrogen density for various types of storage techniques (P = 1 bar and T = 298 K unless otherwise noted). Color representation: dark blue, pressurized hydrogen; grey, physisorbed hydrogen on carbon; light blue, liquid hydrogen; black, chemisorbed hydrogen on carbon; green, liquid hydrogen chemisorbed on carbon; pink, complex hydrides; and red, metal hydrides [46].

1.4 Dissertation Organization

The remainder of this dissertation is organized as follows: Chapter 2 describes how HRES components and sizes can be rationally selected, with separate residential and industrial applications as examples. The design and control principles of HRESs are developed and demonstrated in Chapter 3 by way of a simulation study involving the UD fuel cell bus. Chapter 4 describes how data can be used to enhance the effectiveness of decentralized and centralized control schemes, while Chapter 5 presents the controller design and experimental study of a PV/WT/battery HRES for

remote power applications. The dissertation is summarized and concluded in Chapter 6.

Chapter 2

RATIONAL SELECTION OF HRES COMPONENTS VIA ECONOMIC AND FEASIBILITY ANALYSIS

2.1 Introduction

The first step in implementing a HRES is to ascertain the appropriate HRES components and sizes that are capable of meeting two operating objectives: 1) satisfy required power demands; and 2) store power that is in excess of the power demand for later use. To meet these operating objectives effectively, HRES components and their sizes cannot be selected randomly. If the selected HRES components are too small, then the operating objectives may not be met. If the selected HRES components are too large, then the cost may be prohibitively high. Therefore, it is necessary to determine an optimal combination of HRES components using a combined feasibility and economic analysis. By doing so, we can help ensure that the operating objectives are satisfied while capital and operational costs are minimized. Hence, the first HRES principle can be stated as follows:

Principle 1: *HRES components and their sizes should be rationally selected using knowledge of component costs, availability of renewable energy resources, and expected power demands of the application.*

Previously, HRES component selection and sizing has been determined from a combined economic and feasibility analysis using Hybrid Optimization Model for Electric Renewables or HOMER®, a software package developed by the National Renewable Energy Laboratory. HOMER® has been used to complete the economic and feasibility analysis of hybrid energy systems consisting of various PV, WT, FC,

electrolyzer, battery, and diesel engine combinations as mentioned in Chapter 1 [10–20]. Although using HOMER® proved to be useful in these studies, they only focused evaluating a single application (usually small-scale, off-grid energy production) or a specific system type under various conditions; no study to date has yet to provide a comprehensive evaluation of the economically optimal system type and size for varying power demand, geographic location, and minimum renewable fraction[2] (MRF). Furthermore, no economic comparison of HRESs to traditional grid energy exists.

In this chapter, we aim to complete two objectives. First, we will demonstrate the use of principle 1 by using HOMER® to determine economically optimal and feasible HRES types and sizes for varying power demand (residential-scale and industrial-scale), geographic location (i.e., varying average annual wind speed and solar irradiance), and MRF. Second, using the results from HOMER®, we will investigate the economic competitiveness of HRESs to grid energy.

2.2 Economic and Feasibility Analysis Approach

HOMER® was used to complete the economic and feasibility analysis. HOMER® determines the cheapest feasible energy solution for a given set of conditions (e.g., average annual wind speed and average annual solar irradiance) by using a set of user-defined inputs to simulate the steady-state operation of each

[2] The minimum renewable fraction, a user-defined variable, is understood as the minimum fraction of the power demand that must be met by renewables over the system lifetime.

discrete energy system combination. An example HRES system configuration that can be analyzed using HOMER® is shown in Fig. 2.1.

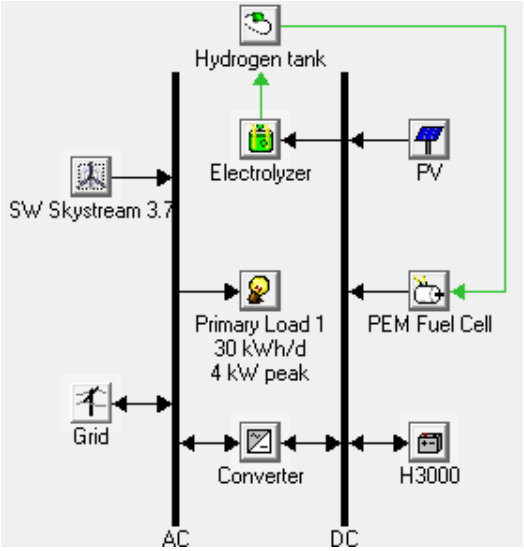

Figure 2.1 PV/WT/FC system configuration in HOMER®. The electrolyzer is used to produce hydrogen, the flow of which is represented by the green lines. The black lines represent power flow. A battery is used to capture excess energy produced and, when needed, releases supplemental energy. The primary load or power demands are typically served by alternating current (AC) power. While grid supply and most WTs provide AC power, PVs, FCs and batteries typically provide direct current (DC) power, hence the need for an AC-DC converter.

The primary inputs to HOMER® are: wind speed, solar irradiance, energy demand profile, capital costs, maintenance costs, system component efficiencies and system size, along with federal and state tax incentives, as appropriate. Our specific illustrative examples are based on the cost parameters shown in Table 2.1 for each component system, with the following additional specifications:

- **PV array:** utilized the 300W-rated LG300N1C-G3 monocrystalline silicon module with an efficiency of 18.3% for both applications.

- **Annual solar irradiance data:** collected from the National Solar Radiation Data Base for Newark, DE (coordinates: 39.68 N, 75.76 W). Solar irradiance was scaled accordingly for average values from 3 kWh/m^2/day to 8 kWh/m^2/day.

- **Power curves for WTs:** used to determine the power output of a wind turbine given wind speed, are available in HOMER® for both a WES 5 Tulipo (2.5 kW rated) WT and a WES 30 (250 kW rated) WT. The WES 5 Tulipo WT was considered in the residential application; the WES 30 WT was considered for the industrial application.

- **Wind speed:** randomly generated in HOMER® using a Weibull k distribution with an average annual wind speed varying from 3.5 m/s to 7 m/s and Weibull k value of 1.95.

- **Efficiency curves for FCs:** used to determine the FC efficiency given the FC power output (Fig. 2.2).

- **Battery:** Hoppecke 24 OPzS 3000 lead-acid battery rated at a nominal capacity of 6 kWh was used in both applications to store excess energy and release energy when needed.

- **Electrolyzer and converter efficiencies:** specified as 80% and 90% respectively.

- **Power demand profile:** assumed that a typical single-family home in the U.S. has an average daily energy demand of 30 kWh for the residential application. For the industrial application, assuming 24-hour operations, an average daily energy demand of 30 megawatt-hours is required (Fig. 2.3).

- **Component sizes:** Listed in Table 2.2 for the residential application and Table 2.3 for the industrial application.

- **Grid connection economics:** It is assumed that each system can: (i) buy grid energy at a rate of $0.11/kWh, (ii) sell energy to the grid at a rate of $0.055/kWh; and (iii) operate continuously for 25 years.

Table 2.1 Costs and tax incentives for WTs, PVs, PEMFCs and HRES supplementary components. Note that the cheapest renewable energy system is a WT while the most expensive renewable energy system is a PEMFC.

System Component	**Capital Costs** [17]	**Maintenance Costs** [17]	**U.S. Federal Tax Incentive** [47]	**Delaware State Tax Incentive** [48]
PV	$4000/kW	$0/kW/yr	30% of capital costs	$0.35/W-$1.25/W, min. 0.5kW system
WT	$3000/kW	$45/kW/yr [49]	30% of capital costs up to $1000/kW.	20% of capital costs
PEMFC (residential only)	$6700/kW	$180/kW/yr	30% of capital costs	$1.25/W and $2500 max.
SOFC (industrial only)	$4000/kW	$180/kW/yr	30% of capital costs	$1.25/W and $2500 max.
Metal Hydride Hydrogen Tank	$1400/kg H2 stored	$0/kW/yr	30% of capital costs	N/A
Electrolyzer	$6700/kW	$1.9/kg H2 produced	30% of capital costs	N/A
Converter	$670/kW	$0/yr	N/A	N/A
Battery	$180/kWh nominal capacity	$15/kWh/yr	N/A	N/A

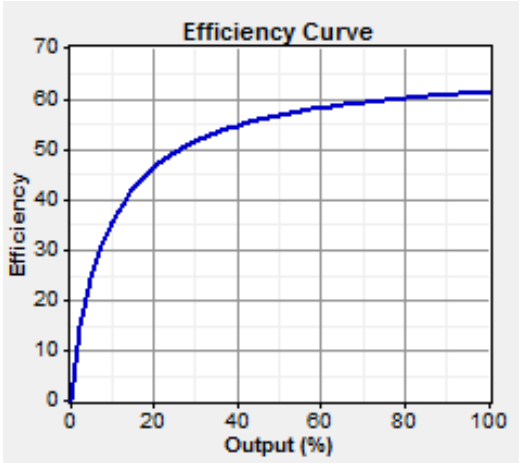

Figure 2.2 Plot of FC efficiency versus percent of maximum power output. This FC efficiency curve was used to simulate the PEMFC and SOFC in HOMER®.

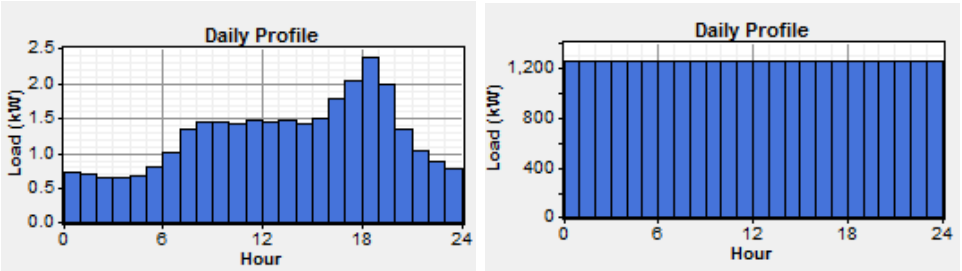

Figure 2.3 Power demand profiles used for the residential (left) and industrial (right) applications. The residential application reflects daily power demand variation in a home while the industrial application has equal power demands throughout the day.

Table 2.2 System components and sizes considered for the residential application. A value of zero indicates the absence of the component in question.

System component (size units)	**Component Sizes**
PV (kW)	0-9
WT (# of 2.5 kW)	0-3
PEMFC (kW)	0-2
Battery (# of 6 kWh nominal capacity)	0-5
Electrolyzer (kW)	0-2

H_2 Tank (kg)	0-300
Converter (kW)	0-11

Table 2.3 System components and sizes considered for the industrial application. A value of zero indicates the absence of the component in question.

System component (size units)	**Component Sizes**
PV (kW)	0-2500
WT (# of 250 kW)	0-10
SOFC (kW)	0-2000
Battery (# of 6 kWh nominal capacity)	0-100
Electrolyzer (kW)	0-2000
H_2 Tank (kg)	$0\text{-}1\text{x}10^6$
Converter (kW)	0-4500

During simulation of an energy system combination, the energy dispatch strategy in HOMER® operates assuming a perfect state controller. In other words, if a certain state or condition met at the current time step, a certain action is performed instantaneously. The energy dispatch strategy used during each HOMER® simulation is described in detail in [50].

2.3 Results and Discussion

2.3.1 Residential Application

The results of the output obtained from HOMER® for the residential application are shown in Figs. 2.4a-2.4e, where each color-coded figure depicts the economically optimal combination of component systems required to meet the MRF in question, under various environmental conditions. The superimposed numbers represent the associated system lifetime cost in $/kWh, with each red line indicating the cost of grid energy ($0.11/kWh). The red "+" in each figure indicates the average environmental conditions of Newark, DE. When the MRF is as low as 10% (Fig. 2.4a)

the only economically optimal system types are a stand-alone WT (light green area at higher wind speeds) and a stand-alone PV (yellow are at higher solar irradiance), indicating that HRESs are too expensive when the MRF is so low. When the MRF is 30%, however, we notice for a small range of wind speed (~4.5 m/s to ~5.25 m/s) and solar irradiance (3 kWh/m^2/day to ~5.5 kWh/m^2/day) the PV/WT HRES (shown in blue) is economically preferred over a stand-alone WT or PV (Fig. 2.4b). Unfortunately, because the blue area representing the PV/WT HRES lies below the red line, these systems are more expensive than grid energy. At a 50% MRF (Fig. 2.4c), there are two results worth noting. First, the blue area representing the PV/WT HRES is now partially above the red line (between ~5.75 m/s to ~6.5 m/s and ~5.5 kWh/m^2/day to 8 kWh/m^2/day), indicating that this particular HRES combination is cost-competitive to grid energy under these conditions for a residential application. Second, the blue area representing the PV/WT HRES has grown to cover over a third of the entire graphical area. After increasing the MRF to 70%, observe that the blue area has grown to cover more than half of the graphical area. Also, when low wind speed (3.5 m/s to 4 m/s) and solar irradiance (3 kWh/m^2/day to 4 kWh/m^2/day) are expected, a PV/WT/PEMFC/electrolyzer system (dark green area) is required due to the lack of renewable resources (Fig. 2.4d). At a 90% MRF, a HRES is required for all environmental conditions, with the PV/WT/PEMFC/electrolyzer HRES required for most of them. Because the FC and electrolyzer are so expensive, almost all geographic locations do not provide a HRES with an economic advantage to grid energy at a MRF as high as 90%.

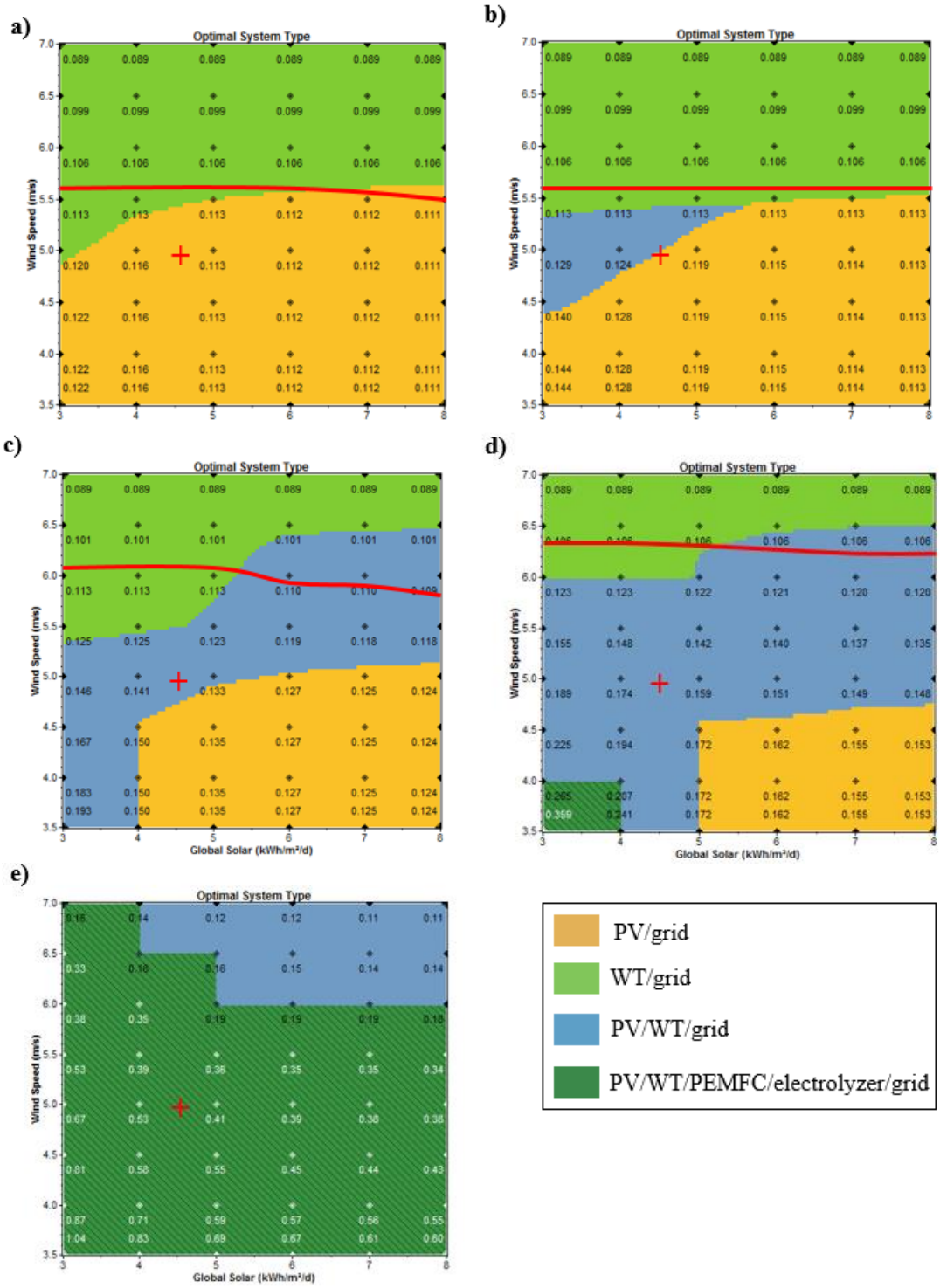
a)
b)
c)
d)
e)
Optimal System Type
Wind Speed (m/s)
Global Solar (kWh/m²/d)
PV/grid
WT/grid
PV/WT/grid
PV/WT/PEMFC/electrolyzer/grid

Figure 2.4 Economically optimal system types for the residential application under varying wind speed and solar irradiance combinations with a MRF of **a)** 10%, **b)** 30%, **c)** 50%, **d)** 70%, and **e)** 90%. The lifetime cost of each system, in $/kWh, is superimposed on each graph. The red line represents the cost of grid energy ($0.11/kWh) and the red "+" indicates the average environmental conditions for Newark, DE.

2.3.2 Industrial Application

The results of the output obtained from HOMER® for the industrial application are shown in Figs. 2.5a-2.5e. Similar to the residential application results, each color-coded figure indicates the economically optimal combination of component systems required to meet the MRF in question under varying average annual wind speed and solar irradiance. The superimposed numbers represent the associated system lifetime cost in $/kWh, each red line indicates the cost of grid energy ($0.11/kWh), and the red "+" signs show the average environmental conditions of Newark, DE. For a MRF of 10% (Fig. 2.5a), notice that the PV/WT HRES (shown in blue) is economically preferred even at such a low MRF for a narrow band of wind speed and solar irradiance combinations, but such systems are more expensive than grid energy. When the MRF increases to 30% MRF (Fig. 2.5b), the PV/WT HRES becomes more prevalent and cost-competitive to grid energy when the wind speed and solar irradiance is greater than 5.5 m/s and 5 kWh/m^2/day, respectively. We also notice that when wind speed and solar irradiance are relatively low (less than 4.5 m/s and 4 kWh/m^2/day, respectively), the SOFC/electrolyzer system is economically preferred—a logical result knowing that renewable resources are low and the SOFC is cheaper than a PEMFC. At a 50% MRF (Fig. 2.5c), most geographic locations would require either a PV/WT, PV/SOFC/electrolyzer (shown in red), or a WT/SOFC/electrolyzer (shown in cyan) HRES, with a significant portion of the PV/WT systems costing less

than grid energy. As the MRF increases to 70% (Fig. 2.5d), observe that a SOFC and an electrolyzer is required for all combinations of wind speed and solar irradiance, with the PV/WT/SOFC/electrolyzer HRES (shown in dark green) economically preferred when the wind speed and solar irradiance is greater than 6 m/s and 5 kWh/m^2/day, respectively. It is also important to note that no systems at a 70% MRF are economically competitive to grid energy. When the MRF reaches as high at 90% (Fig. 2.5e), the SOFC/electrolyzer HRES is ubiquitous across most wind speed and solar irradiance combinations.

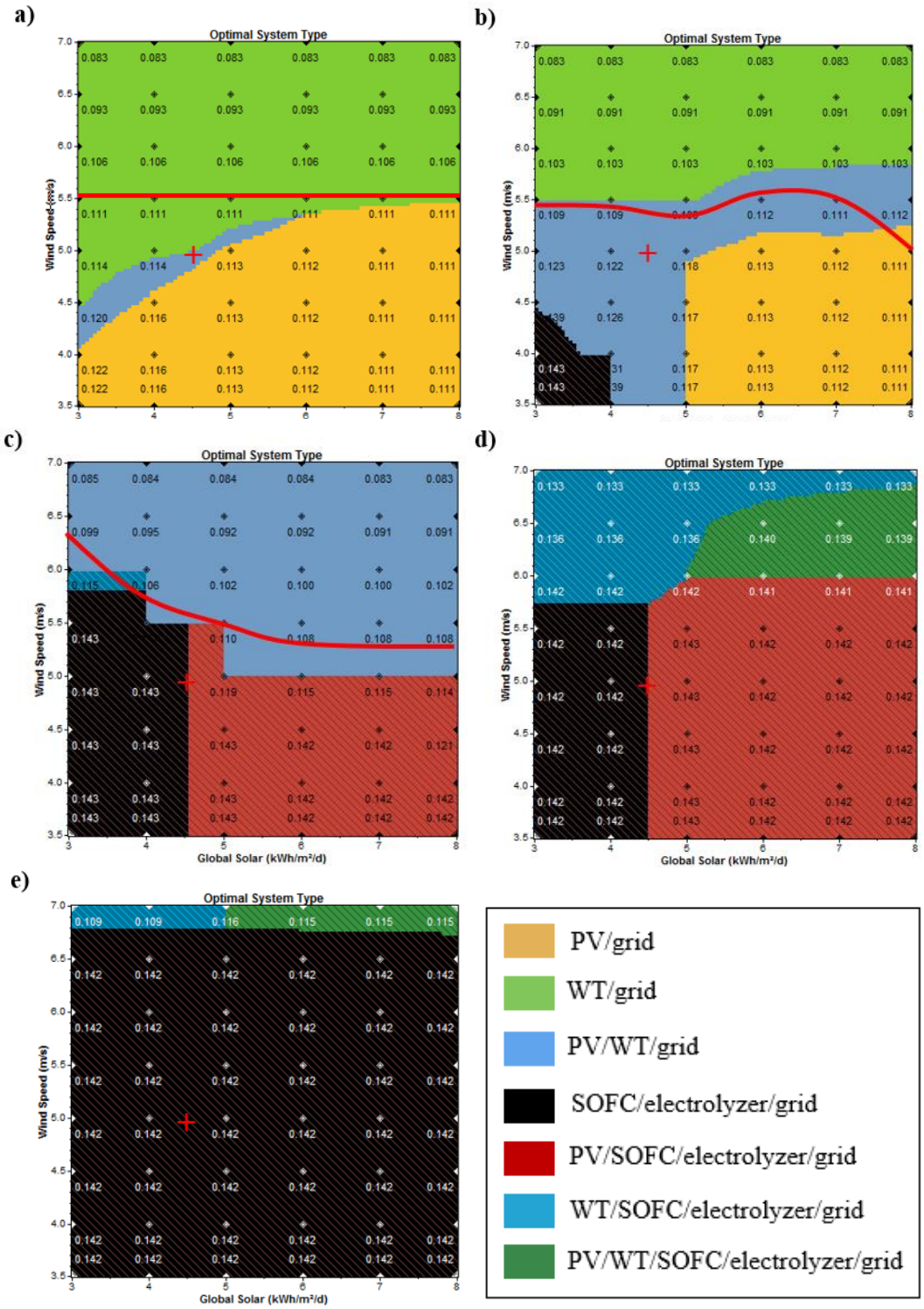
a)
b)
c)
d)
e)
Optimal System Type
Wind Speed (m/s)
Global Solar (kWh/m²/d)
PV/grid
WT/grid
PV/WT/grid
SOFC/electrolyzer/grid
PV/SOFC/electrolyzer/grid
WT/SOFC/electrolyzer/grid
PV/WT/SOFC/electrolyzer/grid

Figure 2.5 Economically optimal system types for the industrial application under varying wind speed and solar irradiance combinations with a MRF of **a)** 10%, **b)** 30%, **c)** 50%, **d)** 70%, and **e)** 90%. The lifetime cost of each system, in $/kWh, is superimposed on each graph. The red line represents the cost of grid energy ($0.11/kWh) and the red "+" indicates the average environmental conditions for Newark, DE.

2.4 Chapter Summary and Conclusions

In this Chapter, we established a principle by which HRES components should be rationally selected. The principle states that "*HRES components and their sizes should be rationally selected using knowledge of component costs, availability of renewable energy resources, and expected power demands of the application.*" This principle was demonstrated by using HOMER®—an economic and feasibility analysis software for energy systems—to determine the cheapest feasible energy system type given a set of user-defined inputs (e.g., power demand, wind speed, solar irradiance, MRF, component costs, etc.). The economic and feasibility analysis was completed for a residential application (30 kWh/day energy demand) and an industrial application (30 MWh/day energy demand). For each application, the economically optimal renewable energy system was determined for a range of average annual wind speed (3.5 m/s to 7m/s), average annual solar irradiance (3 kWh/m^2/day to 8 kWh/m^2/day), and MRF (10% to 90%). Our results show that under some combinations of average annual wind speed, average annual solar irradiance, and MRF, HRESs are economically preferred over stand-alone renewable energy systems. Moreover, some of the economically preferred HRESs are cost-competitive to grid energy. The HRESs that are cost-competitive to grid energy generally require an average annual wind speed of greater than 6 m/s, an average annual solar irradiance greater than 5.5 kWh/m^2/day, and a MRF between 30% and 70% for both applications. Although these

requirements eliminate many geographic locations and applications, this may not be the case within the near future as the cost of renewables continues to fall and the cost of grid energy continues to rise (see Section 1.1).

Chapter 3

DESIGN, OPERATION, AND CONTROL OF HRESS

3.1 Introduction

Once the HRES components and sizes are selected from the economic and feasibility analysis, their arrangement must be decided. The HRES components can be arranged in parallel or series (Fig. 3.1). In a parallel arrangement, power from each HRES component assists directly in meeting the power demand. In a series design, power from one component can only be stored in another, and then released to meet the power demand.

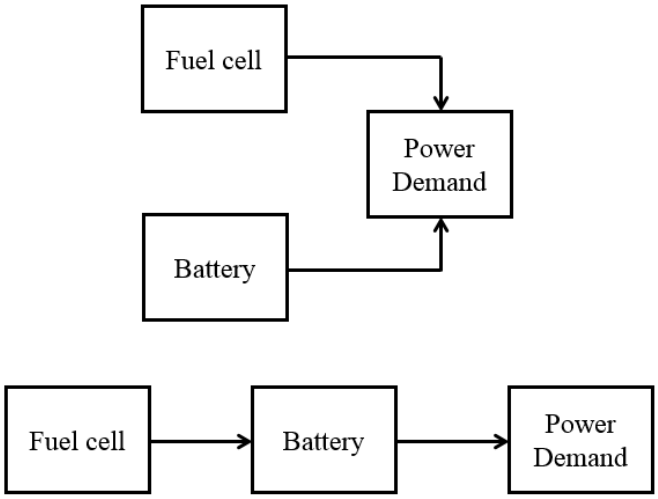

Figure 3.1 Schematic of a fuel cell/battery HRES arranged in parallel (top) and series (bottom). Black arrows represent flow of power.

But how do we decide which type of HRES design should be used such that operating objectives (see Section 2.1) are met consistently? A parallel design offers

higher energy efficient and reliable because multiple components can be used directly to meet the power demand, but a series design may be beneficial for some applications. For example, consider a shuttle bus that operates using either the parallel or series FC/battery design shown schematically in Fig. 3.1. Assuming each arrangement has an identical FC and battery, the parallel design is more efficient and reliable. However, the parallel design may lack longevity because rapid fluctuations in power demand, and thus FC power output, can degrade FC lifetime. In addition, the lifetime of some batteries (e.g., a NiCd battery) can be extended if a desired state of charge (SOC) is sustained throughout operation. Battery SOC is better maintained in a series design where a renewable energy system can be dedicated to charging the battery. Therefore, for this specific example, a series FC/battery design offers a practical advantage over the parallel FC/battery design when accounting for the operational considerations of the HRES components. Thus, the second HRES principle can be stated as follows:

Principle 2: *By default, the components of a HRES should be arranged in parallel for increased efficiency and reliability. However, a series HRES design may be preferred depending on the operational considerations of the HRES components.*

After the design is established, an appropriate control system must be developed that enables a HRES to meet the two operating objectives listed in Section 2.1. However, there are major challenges involved in the control of HRES, specifically those consisting of PVs, WTs, FCs, electrolyzers, and batteries. For example, PV and WT power vary drastically and often unpredictably, and will never be available,

individually or jointly, in a form that synchronizes perfectly with the independently varying power demand. Without proper control system design and intelligent coordination, therefore, the HRES cannot function effectively. Additionally, the inherent complexity, non-linear dynamics, and the various physical operational constraints associated with PVs, WTs, FCs, electrolyzers, and batteries combine to make deliberate control of the HRES's power output to a specific target extremely difficult.

The three major classes of control strategies that can be used to overcome these challenges in meeting the operating objectives, in order of increasing complexity and required computing power, are state control, proportional-integral-derivative (PID) control, and model predictive control (MPC). State control uses a set of conditional, if/then statements to decide how the flow of power is managed in a HRES. For example, if the system experiences a certain state, then a pre-specified action is performed. PID control meets operating objectives by reducing the present feedback error in control loops using separate proportional, integral, and derivative operators. MPC minimizes feedback error in control loops over an entire prediction horizon using a constrained optimization algorithm in conjunction with a state estimator.

But how do we choose among these types of control strategies for a given HRES and application? To answer this question, it is necessary to have a firm understanding of the HRES components as well as the desired end-use. A state controller, for instance, may be preferred when the system components used for control do not exhibit difficult dynamics[3] (e.g., time delays and large time constants)

---

[3] Of the components considered in this dissertation, the battery, the FC, and the electrolyzer are components available for control (WTs and PVs generate power that

and when substantial computing power is impractical (i.e. for small-scale remote power applications where the power needed to run a high-performance controller continuously is detrimental to the system). On the contrary, the benefits of MPC—primarily its constraint-handling abilities and incorporation of state estimation into predictive feedback control—may outweigh its implementation cost when HRES components have difficult dynamics and when heavy computing power is practical (i.e., for large-scale stationary applications that can afford the parasitic power required to run a high-performance controller continuously).

Principle 3: *Choice of control strategy for a HRES (e.g., state control, PID control, or MPC) depends on the dynamics of HRES components, their operational considerations, and the practical limitations of the HRES end-use.*

This Chapter presents a demonstration of principles 1, 2, and 3 via a case study involving the addition of a PV array to an existing FC/battery HRES for automotive applications. Because the FC/battery HRES arrangement has previously been established (relevant to principle 2), the case study highlights the design of an appropriate control strategy for such a system (relevant to principle 3) and the economic incentive of adding a PV array to the bus (relevant to principle 1).

---

cannot be controlled). Most types of batteries are not known to have difficult dynamics, whereas FCs (especially SOFCs) and electrolyzers usually do.

3.2 Case Study: A PV/FC/Battery HRES for Automotive Applications

3.2.1 Overview

Because using internal combustion engines (ICEs) to power vehicles is an unsustainable, environmentally hazardous practice, it is important to develop cost-effective and reliable renewable energy systems for automotive applications. For such applications, PEMFCs have some inherent advantages over ICEs. For example, many PEMFC-powered vehicles are more than twice as thermodynamically efficient as ICE-powered vehicles, while emitting zero greenhouse gases [51]. Furthermore, PEMFCs have fewer moving parts than ICEs, making them more reliable and less noisy [52]. Despite such advantages, the automotive industry has not been receptive to PEMFCs compared with ICEs, for two reasons: a higher cost of manufacture (~$3000/kW vs ~$50/kW [53]) and a lower vehicle accelerating potential (i.e., specific power) (~100 W/kg vs ~1000 W/kg [54]), which jointly make stand-alone PEMFCs impractical in automotive applications. Such shortcomings can be mitigated, however, by judiciously combining a PEMFC with one or more complementary renewable energy systems to form a HRES.

At the University of Delaware, a HRES shuttle bus consisting of a PEMFC and a NiCd battery (Fig. 3.2) was recently incorporated into the university's shuttle bus system [55]. In the HRES design, the NiCd battery is used to meet the power demand of the bus while the hydrogen-fueled PEMFC is used to maintain a desired state of charge (SOC) of the NiCd battery. (The rationale behind the series design is explained in Section 3.1. and in [55]) Because a NiCd battery is less expensive than a PEMFC (~$300/kW vs ~$3000/kW [56]) and has a higher accelerating potential (~250 W/kg

vs ~100 W/kg [54]), the HRES design provides a cheaper and more practical alternative to a stand-alone PEMFC-powered bus.

Figure 3.2 The University of Delaware's 22-foot, 22-seat transit bus manufactured by EBus, Inc. of Downey, CA, and equipped with a fuel cell/battery series-hybrid powertrain.

Although a FC/battery bus offers a viable "no emissions" alternative for automotive applications, it remains more expensive than traditional buses powered by ICEs. Further cost reduction can be achieved, without increasing greenhouse gas emissions, by incorporating a roof-installed PV array into the current design. The power produced by the PV array can be used in two ways: (1) to supplement the battery in meeting the bus's power demand; and (2) to supplement the FC in charging the battery. Because the power required by the fuel cell to maintain battery SOC is thereby reduced, so too is the use of hydrogen, which is an operating cost of the bus. The lifetime cost of the FC/battery bus can therefore be reduced with the addition of a PV array.

The operating objectives of a PV/FC/battery-powered bus are two-fold: (1) satisfy bus power demands; and (2) maintain the NiCd battery state of charge (SOC) at 65%. The operating objectives are challenging to meet due to rapid fluctuations in required bus speed (i.e., bus power demand) and available PV power throughout a shuttle run. The consequences of not overcoming these challenges are overuse or underuse of the battery in meeting the power demand, and deep battery discharge (< 20% SOC) or battery overcharging (> 80% SOC) [57] (the latter initiating oxygen-producing side reactions in the battery that can degrade the battery operating lifetime [58]). One goal of this case study, therefore, is to design a control strategy that enables the PV/FC/battery HRES to satisfy the power demand of the bus while maintaining the battery SOC at 65% in spite of rapid fluctuations in bus power demand and PV power.

Two separate control strategies are considered here: an algebraic control strategy (currently being used on the bus [55] and which will be described shortly) and a standard PID control strategy. The algebraic control strategy consists of controllers that use algebraic equations to determine the controller output (battery power request and FC power request) needed to meet the operating objectives of the bus. The original algebraic control strategy was specifically designed to enable the fuel cell/battery HRES to meet bus operating objectives only under normal conditions (i.e., typical shuttle runs). Although the original algebraic control strategy can be modified to include PV power, such a control strategy may not satisfy bus operating objectives when the bus is subject to abnormal operating conditions (i.e., sustained increases in bus speed). Should the bus experience abnormal operating conditions, a standard PID control strategy, may outperform the algebraic control strategy.

Because the addition of a PV array to the FC/battery bus affects operating costs, it is also necessary to determine the economic incentive for adding a PV array in terms of the return on investment (ROI) obtained from:

$$ROI = 100\left(\frac{\left[365L_{bus}A_{bus}C_{H_2}\left(M_{H_2,no\ PV} - M_{H_2,PV}\right)\right] - C_{PV}}{C_{PV}}\right), \tag{3.1}$$

where L_{bus} is the lifetime of the bus, A_{bus} is the bus availability, C_{H_2} is the cost of hydrogen, C_{PV} is the cost of the PV array (all fixed constants), $M_{H_2,no\ PV}$ is the mass of hydrogen consumed per day by the bus without a PV array, and $M_{H_2,PV}$ is the mass of hydrogen consumed per day by the bus with an incorporated PV array (these are functions of average solar irradiance during bus operation ($G_{T,avg}$), PV array size (S_{PV}), and PV array efficiency (η_{PV})). Thus, ROI will vary as a function of $G_{T,avg}$, S_{PV}, and η_{PV}. A second goal of this case study is therefore to determine the values of $G_{T,avg}$, S_{PV}, and η_{PV} required for positive ROI.

3.2.2 Process Description

The process under investigation is a PV/FC/battery HRES employed in a bus (shown schematically Fig. 3.3), which consists of four primary components: a NiCd battery, a PEMFC system, a PV array, and a traction motor. The majority of the bus' power demand is to be satisfied using the 120 kW-rated SAFT NiCd battery. The battery is charged primarily using the 32 kW-rated PEMFC system, which is comprised of two Ballard Mark9 SSL PEMFCs. The 2.4 kW-rated[4] PV array, consisting of eight LG300N1C-G3 monocrystalline silicon modules that will cover

[4] The PV array rated power output is the power output of the array under standard test conditions (G_T = 1000 W/m^2, a PV module temperature of 25°C, and a solar spectrum irradiance of AM 1.5).

most of the roof of the bus (~15 m^2), is to be used to supplement the battery output in meeting the power demand of the bus, and to assist the FC in charging the battery. A three-phase alternating current (AC) induction traction motor is responsible for converting electrical energy from the battery or PV array to mechanical energy that moves the bus. The traction motor has regenerative braking capability, producing electricity to charge the battery as the bus decelerates.

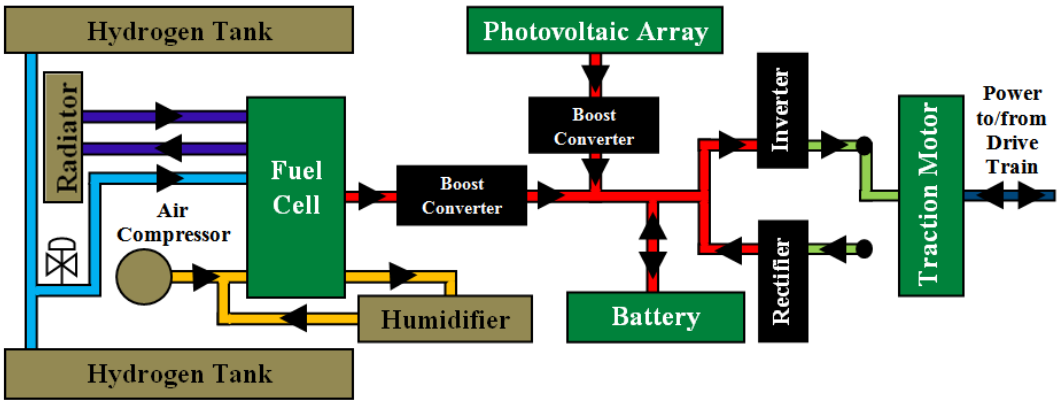

Figure 3.3 Schematic diagram of the UD fuel cell bus's PV/PEMFC/NiCd battery hybrid power train. Color legends: (1) Blocks: green, primary components; beige, auxiliary fuel cell components; black, power conditioning units. (2) Streams: purple, glycol/water mixture; light blue, hydrogen; yellow, air; red, DC power; light green, AC power; dark blue, mechanical power to/from the drive train. Black arrows indicate stream flow direction.

The PEMFC is maintained by four auxiliary components: twin high-pressure hydrogen storage tanks, a scroll-type air compressor, a fan-cooled radiator, and a membrane humidifier. The high-pressure hydrogen storage tanks, each rated at 350 bar, can store up to 6.4 kg of hydrogen. The stored hydrogen is released to the anode

of the PEMFC system using a pressure regulator valve, while oxygen is delivered to the cathode of the PEMFC system using a scroll-type air compressor. The temperature of the fuel-cell system is maintained at 70°C using a low-conductivity ethylene glycol/water mixture and a fan-cooled radiator. A membrane humidifier maintains relative humidity of the compressed air at 100% using moisture from the cathode exhaust air.

The power conditioning units on the bus (which are used to match the voltage and current type of an electrical power source with an electrical power sink) consist of two boost converters, an inverter, and a rectifier. Each boost converter increases the low voltage direct current (DC) power (~75 V for the fuel cell and ~30 V for the PV array) to match the high voltage DC power of the main DC bus (~300V). The inverter is used to convert DC power from the main DC bus to three-phase AC power usable by the traction motor, while the rectifier converts three-phase AC power from regenerating braking to DC power usable by the battery.

3.2.3 Process Modeling and Simulation

A modular approach was used to model and simulate the previously described PV/FC/battery HRES in Simulink. The PV, FC, battery, and traction models were constructed separately using models provided in the literature. The remainder of this subsection describes the PV/FC/battery HRES mathematical models.

3.2.3.1 PV Array Model

The PV array model (Fig. 3.4) is used to determine the power delivered from the PV array given the intensity of the incident solar irradiance on the surface of the photovoltaic material (G_T) and the ambient temperature (T_a). To calculate the power

delivered from a PV array, the temperature of the PV array (T_{array}) must first be determined using G_T and T_a as follows [59]:

$$T_{array} = \frac{T_a + (NOCT - T_{a,NOCT})\left(\frac{G_T}{G_{T,NOCT}}\right)\left[1 - \frac{\eta_{mp,STC}\left(1 - \alpha_{PT_{c,STC}}\right)}{\tau\alpha_{PV}}\right]}{1 + (NOCT - T_{a,NOCT})\left(\frac{G_T}{G_{T,NOCT}}\right)\left(\frac{\alpha_P \eta_{mp,STC}}{\tau\alpha_{PV}}\right)} + 273, \qquad (3.2)$$

where $NOCT$ is the nominal operating cell temperature[5], $T_{a,NOCT}$ is the ambient temperature at which NOCT is defined, $G_{T,NOCT}$ is the solar irradiance at which NOCT is defined, $\eta_{mp,STC}$ is the maximum power point efficiency under STC[6], α_P is the temperature coefficient of power, $T_{c,STC}$ is the PV cell temperature under STC, τ is the PV array cover film solar transmittance, and α_{PV} is the PV array solar absorptance.

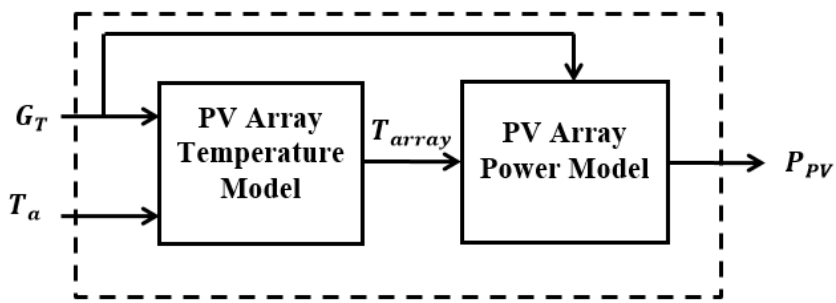

Figure 3.4 Schematic of the PV array model.

---

[5] Nominal operating conditions are T_{array} = 20°C, G_T = 800 W/m^2, and a wind speed of 1 m/s, with the back side of the PV panel exposed to the wind

[6] Standard test conditions are T_{array} = 25°C, G_T = 1000 W/m^2, and a solar spectrum irradiance of AM 1.5.

After determining the temperature of the PV array, the PV array power (P_{PV}) can be obtained. First, the light-generated current (I_{ph}) and the saturation current (I_o) can be calculated from [60]

$$I_{ph} = \left[I_{scr} + K_i\left(T_{array} - 298\right)\right]\left({}^{G_T}/_{1000}\right) \tag{3.3}$$

and

$$I_o = I_{or}\left(\frac{T_{array}}{T_r}\right)^3 \exp\left[\frac{qE_{G0}}{Ak}\left(\frac{1}{T_r} - \frac{1}{T_{array}}\right)\right]. \tag{3.4}$$

Here, I_{scr} is the short-circuit current of the PV cell under STC, K_i is the short-circuit current temperature coefficient at I_{scr}, T_r is the reference PV array temperature, I_{or} is the PV cell saturation current at T_r, q is the charge of an electron, E_{G0} is the band gap of silicon, A is the ideality factor of the PV array, and k is Boltzmann's constant. The short-circuit current (I_{sc}) can then be calculated using I_{ph} as shown below:

$$I_{sc} = n_p I_{ph}, \tag{3.5}$$

where n_p is the number of cells connected in parallel in each PV module. The short-circuit current is required for the short-current pulse maximum power point tracking (MPPT) technique, which determines the optimal operating current (I_{op}) of each module resulting in maximum PV array power output as follows [30]:

$$I_{op} = k_{MPPT} I_{sc}. \tag{3.6}$$

Here, k_{MPPT} is a proportional constant for the short-current pulse MPPT method. The value of k_{MPPT} for the PV array under consideration was determined by taking the slope of the line of best fit between I_{op} and I_{sc} as shown in Fig. 3.5.

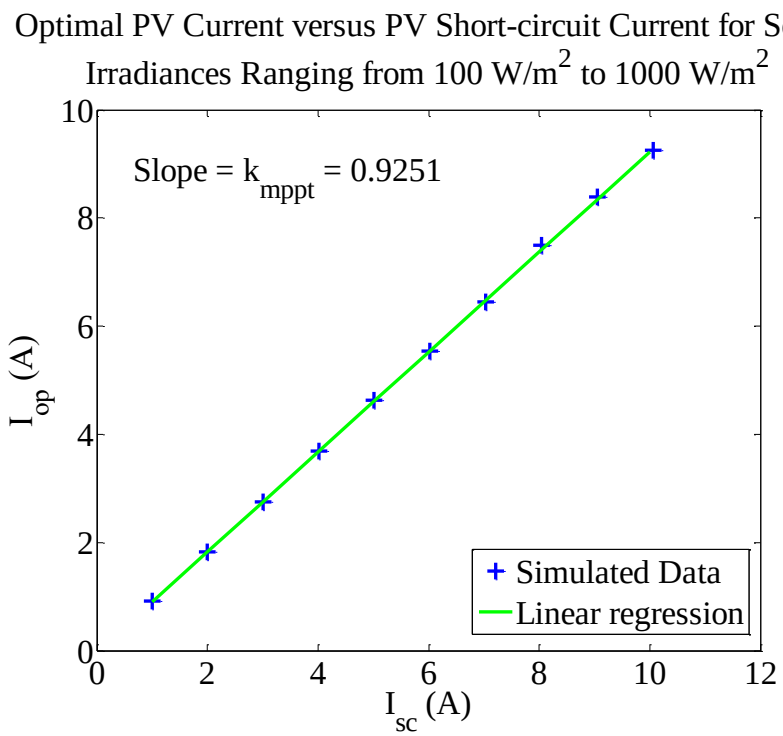

Figure 3.5 Optimal PV current versus PV short-circuit current for solar irradiances ranging from 100 W/m^2 (data point corresponding to the lowest value of I_{sc}) to 1000 W/m^2 (data point corresponding to the highest value of I_{sc}). Blue plus signs indicate simulated data and the green line represents the line of best fit calculated via linear regression of the simulated data. The slope of the linear regression line (0.9251) is equal to k_{MPPT}.

The optimal operating current is the same for each PV module because we assume each PV module in the array is exposed to the same amount of solar irradiance and ambient temperature. Therefore, the usable power generated by the entire PV array can be expressed as [30]:

$$P_{PV} = I_{op}\eta_{boost,PV}n_m\frac{AT_{array}kn_s}{q}\ln\left(\frac{-I_{op}+n_pI_{ph}+n_pI_o}{n_pI_o}\right), \tag{3.7}$$

where $\eta_{boost,PV}$ is the efficiency of the boost DC/DC converter that is used to match the DC voltage generated by the PV array to the higher voltage DC mains on the bus (~300 V), n_m is the number of PV modules in the PV array, and n_s is the number of cells connected in series in each PV module. The parameters of the PV array model are listed in Table 3.1.

Table 3.1 PV array model parameters.

Description	Symbol	Value	Units
Nominal operating cell temperature	$NOCT$	46.5	°C
Ambient temperature at which $NOCT$ is defined	$T_{a,NOCT}$	20	°C
Solar irradiance at which $NOCT$ is defined	$G_{T,NOCT}$	800	W/m^2
Maximum power point efficiency under STC	$\eta_{mp,STC}$	18.3	%
Temperature coefficient of power	α_P	-0.42	%/°C
PV array temperature under STC	$T_{c,STC}$	25	°C
Solar transmittance of any cover over the PV array	τ	90	%
Solar absorptance of the PV array	α_{PV}	90	%
Reference Short-circuit current of the PV cell under STC	I_{scr}	10	A
Short-circuit temperature coefficient at I_{scr}	K_i	0.003	A/°C
Reference PV cell temperature	T_r	301.18	K
PV cell saturation current at T_r	I_{or}	2.0793x10^{-6}	A
Charge of an electron	q	1.6x10-19	C
Band gap of silicon	E_{G0}	1.10	eV
Ideality factor of the PV array	A	1.3	N/A
Boltzmann's constant	k	1.3805x10^{-23}	J/K
Proportionality constant for the short-current pulse MPPT method	k_{MPPT}	0.9251	N/A
Number of modules in the PV array	n_m	8	N/A
Number of cells connected in series per module	n_s	60	N/A
Number of cells connected in parallel per module	n_p	1	N/A
Efficiency of the Boost Converter	$\eta_{boost,PV}$	0.90	N/A

3.2.3.2 Fuel Cell Model

As shown in Fig. 3.6, the fuel cell model calculates the fuel cell net power output (P_{FC}^{net}) using the fuel cell power requested by a controller (P_{FC}^{req}) and T_a. To determine P_{FC}^{net}, the fuel cell gross power output (P_{FC}^{gross}) and the fuel cell balance of plant power requirements (P_{BOP}) must be known.

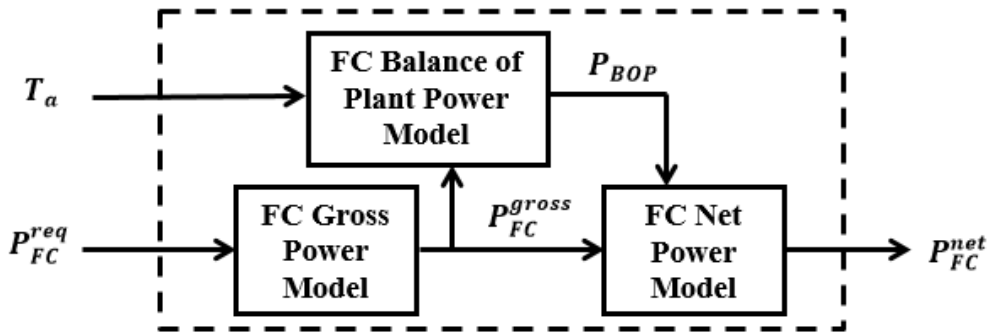

Figure 3.6 Schematic of the fuel cell model

The gross fuel cell power output is controlled using a programmable logic controller on the bus that accepts P_{FC}^{req} as a setpoint and adjusts the mass flowrate of hydrogen into the fuel cell ($\dot{m}_{H_2}$) such that P_{FC}^{gross} matches P_{FC}^{req}. The closed-loop response between P_{FC}^{req} and P_{FC}^{gross} is approximated using a first order model in the Laplace domain expressed as:

$$P_{FC}^{gross} = \frac{K_{FC}}{\tau_{FC}s + 1} P_{FC}^{req}, \tag{3.8}$$

where K_{FC} and τ_{FC} are the steady-state gain and time constant of the closed-loop response between P_{FC}^{req} and P_{FC}^{gross}, respectively. These two parameters were approximated using data collected from the fuel cell stack in response to a step decrease in P_{FC}^{req} (Fig. 3.7).

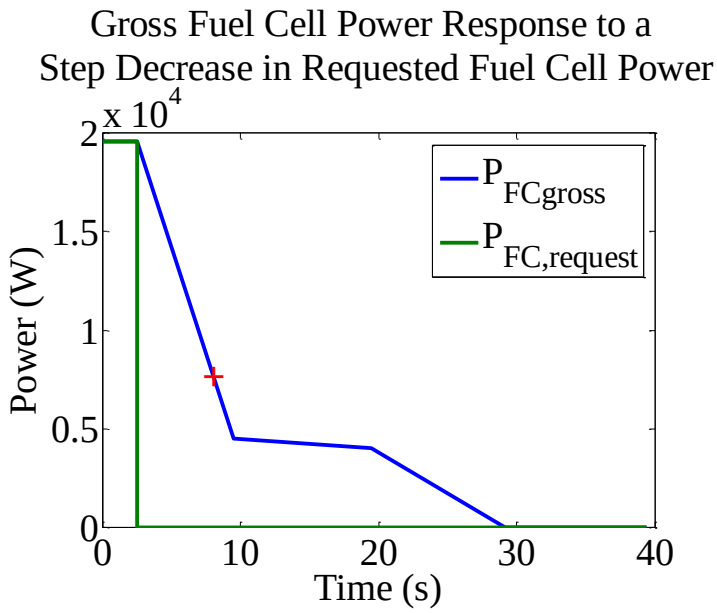

Figure 3.7 Gross fuel cell power response to a step decrease in requested fuel cell power from 19,600 W to 0 W. The blue line indicates the gross power response and the green line the step decrease in requested power. The red plus sign marks the point at which the gross fuel cell power output has reached 63.2% of its steady-state value. The time corresponding to this value (8 sec.) minus the time at which the step change was made (2.5 sec) is equal to the closed-loop time constant (τ_{FC}). The closed-loop steady-state gain (K_{FC}) is equal to 1.

Because the steady-state values of P_{FC}^{req} and P_{FC}^{gross} are both equal to zero, Eq. 3.8 is represented in real variables as opposed to deviation variables. The calculation of P_{FC}^{gross} assumes that temperature and relative humidity within the stack are controlled properly to their desired values of 70°C and 100%, respectively. This model assumption was found to not significantly affect the fidelity of a simulation of the existing fuel cell/battery bus [61].

The balance of plant power requirements can be expressed as the sum of the power required by the air compressor P_c, the hydrogen pump P_{hp}, and the radiator P_{rad} expressed as

$$P_{BOP} = P_c + P_{hp} + P_{rad}. \tag{3.9}$$

The combined power required by the hydrogen pump and radiator is assumed to be 1 kW while the power required by the air compressor is calculated as follows [61]:

$$P_c = \frac{C_p T_a}{\eta_m \eta_c}\left[\left(\frac{p_{sm}}{p_a}\right)^{(\gamma-1)/\gamma} - 1\right]\dot{m}_c, \tag{3.10}$$

where C_p is the nominal specific heat capacity of air at constant pressure, η_m is the compressor motor efficiency, η_c is the compressor efficiency, p_{sm} is the pressure in the supply manifold, p_a is the ambient pressure, γ is the nominal adiabatic index of air, and $\dot{m}_c$ is the mass flowrate of air through the compressor. The following expression is used to calculate $\dot{m}_c$:

$$\dot{m}_c = \frac{\lambda_{O_2} M_{O_2}}{4 y_{O_2} M_{H_2}}\left[1 + \frac{M_v \phi_a p_{sat,v}}{M_a p_a}\right]\left(2\dot{m}_{H_2} - \dot{m}_{purge}\right), \tag{3.11}$$

where λ_{O_2} is the oxygen excess ratio, y_{O_2} is the mole fraction of oxygen in air, M_{O_2} is the molar mass of oxygen, M_{H_2} is the molar mass of hydrogen, M_{H_2} is the molar mass of water vapor, M_a is the molar mass of dry air, ϕ_a is the relative humidity of the ambient air, $p_{sat,v}$ is the vapor saturation pressure at ambient temperature, and $\dot{m}_{purge}$ is the purge rate of hydrogen. Finally, $\dot{m}_{H_2}$ is obtained from:

$$\dot{m}_{H_2} = \frac{n_{FC} M_{H_2} I_{st}}{2F} + \dot{m}_{purge}, \tag{3.12}$$

where n_{FC} is the number of cells in the fuel cell stack and I_{st} is the fuel cell stack current. The stack current is determined using the net fuel cell power curve, which was constructed using real data from the fuel cell stack (Fig. 3.8).

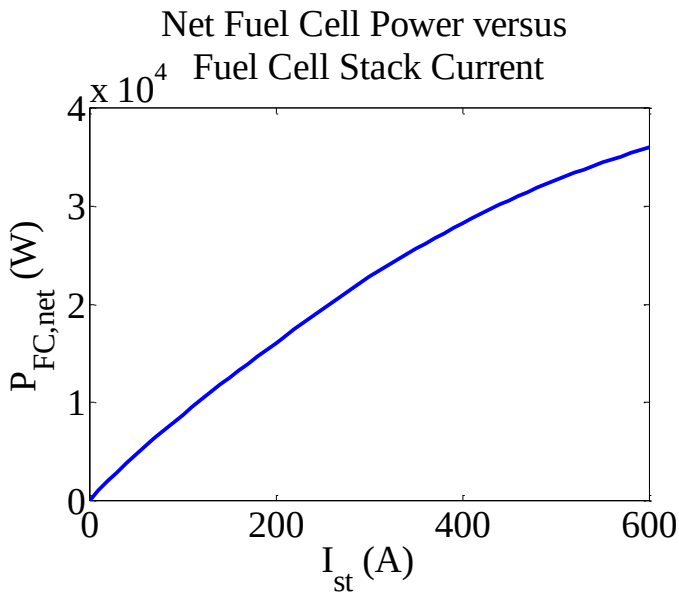

Figure 3.8 Net fuel cell power (P_{FC}^{net}) as a function of fuel cell stack current (I_{st}). After calculating P_{FC}^{net}, this curve can be used to determine I_{st}.

The net fuel cell power output is simply the difference between the gross fuel cell power output and the balance of plant power requirement multiplied by a converter efficiency:

$$P_{FC}^{net} = \eta_{boost,FC}\left(P_{FC}^{gross} - P_{BOP}\right), \tag{3.13}$$

where $\eta_{boost,FC}$ is the efficiency of the boost DC/DC converter used is used to match the DC voltage generated by the PV array to the higher voltage DC mains on the bus (~300 V). The parameters used for the fuel cell model are listed in Table 3.2.

Table 3.2 Fuel cell model parameters.

Description	Symbol	Value	Units
Steady-State Gain Between P_{FC}^{req} and P_{FC}^{gross}	K_{FC}	1	W/kg/s
Time Constant Between P_{FC}^{req} and P_{FC}^{gross}	τ_{FC}	5.5	s
Nominal Specific Heat Capacity of Air	C_p	1000	J/kg/K

Compressor Motor Efficiency	η_m	0.8	N/A
Compressor Efficiency	η_c	0.7	N/A
Supply Manifold Pressure	p_{sm}	103500	Pa
Ambient Pressure	p_a	101325	Pa
Nominal Adiabatic Index of Air	γ	1.4	N/A
Oxygen Excess Ratio	λ_{O_2}	1.6	N/A
Molar mass of Oxygen	M_{O_2}	32	g/mol
Molar Mass of Hydrogen	M_{H_2}	2	g/mol
Molar Mass of Water Vapor	M_v	18	g/mol
Molar Mass of Dry Air	M_a	28.84	g/mol
Relative Humidity of Ambient Air	ϕ_a	0.8	N/A
Purge Rate of Hydrogen	$\dot{m}_{purge}$	5.56×10^{-6}	kg/s
Number of cells in the fuel cell stack	n_{FC}	110	N/A
Efficiency of the Boost Converter	$\eta_{boost,FC}$	0.90	N/A

3.2.3.3 Battery Model

As shown in Fig. 3.9, the battery model is responsible for determining the battery discharge power (P_{batt}^{dis}) and the measured battery SOC (SOC_m) given the battery power requested by a controller (P_{batt}^{req}) and the battery charging power (P_{batt}^{ch}).

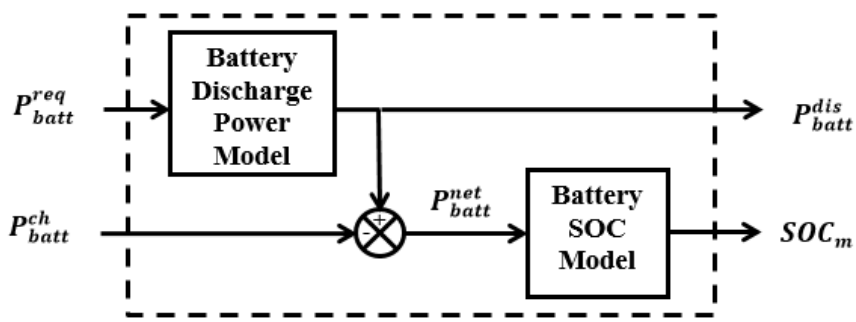

Figure 3.9 Schematic of the battery model.

The battery discharge power is calculated using a first order model in the Laplace domain represented by:

$$P_{batt}^{dis} = \frac{K_{batt}}{\tau_{batt}s + 1} P_{batt}^{req}, \tag{3.14}$$

where K_{batt} and τ_{batt} are the steady-state gain and time constant of the process, respectively. Because the steady-state values of P_{batt}^{dis} and P_{batt}^{req} are zero, they can be represented as real variables instead of deviation variables in Eq. 3.14. The value of K_{batt} is 1 since the steady-state discharge power is equal to the power signal that the battery receives from a controller, and the value of τ_{batt} is 0.1 seconds since battery actuation exhibits rapid dynamics.

After computing P_{batt}^{dis}, SOC_m can be determined using

$$P_{batt}^{net} = P_{batt}^{dis} - P_{batt}^{ch}, \tag{3.15}$$

$$I_{batt}^{net} = \frac{P_{batt}^{net}}{V_{batt}}, \tag{3.16}$$

$$V_{batt} = \begin{cases} V_{OC} - R_{int,ch} I_{batt}^{net} & I_{batt}^{net} < 0; \\ V_{OC} - R_{int,dis} I_{batt}^{net} & I_{batt}^{net} > 0; \end{cases}, \tag{3.17}$$

and

$$SOC_m = \begin{cases} SOC_0 - \eta_{batt,ch} \dfrac{\int_0^t I_{batt}^{net}\, dt}{C}, & I_{batt}^{net} < 0; \\ SOC_0 - \eta_{batt,dis} \dfrac{\int_0^t I_{batt}^{net}\, dt}{C}, & I_{batt}^{net} > 0; \\ SOC_0, & I_{batt}^{net} = 0 \end{cases}. \tag{3.18}$$

Here, P_{batt}^{ch} is the total power charging the battery (sum of P_{FC}^{net}, power from regenerative braking, and PV power remaining after power demands are met), V_{batt} is the battery voltage ranging from 240 V to 370 V, I_{batt}^{net} is the net battery current

ranging from -400 A to 400 A, V_{OC} is the battery open-circuit voltage, $R_{int,ch}$ and $R_{int,dis}$ are the battery internal charge and discharge resistance, respectively, SOC_0 is the battery SOC at the previous time step, $\eta_{batt,ch}$ is the battery charge efficiency, $\eta_{batt,dis}$ is the battery discharge efficiency, t is the time step, and C is the battery charge capacity. Fig. 3.10 shows the empirical data used to determine V_{OC}, $R_{int,ch}$, and $R_{int,dis}$ as a function of SOC_m. The parameters of the battery model are given in Table 3.3.

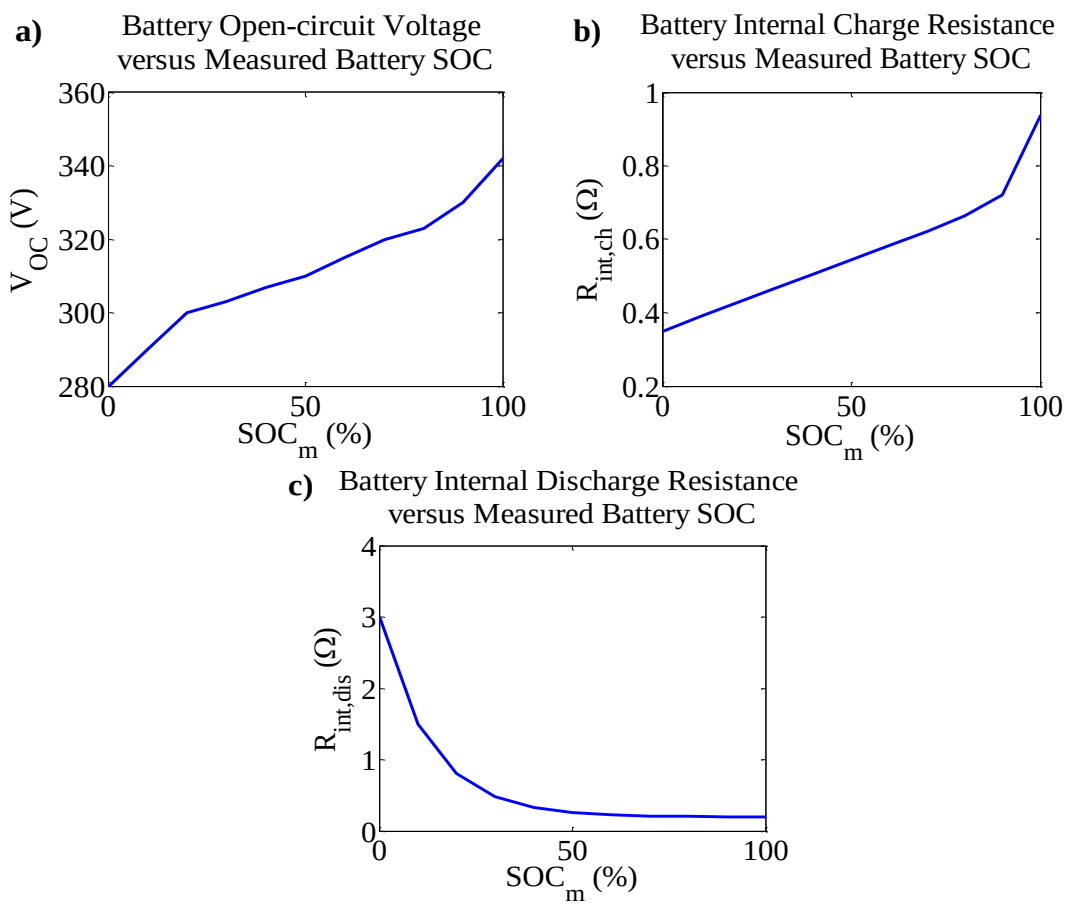

Figure 3.10 Empirical data collected from the NiCd battery for: **a)** $V_{OC} = f(SOC_m)$; **b)** $R_{int,ch} = f(SOC_m)$; and **c)** $R_{int,dis} = f(SOC_m)$.

Table 3.3 Battery model parameters.

Description	Symbol	Value	Units
Steady-state gain between $P_{batt,request}$ and $P_{batt,dis}$	K_{batt}	1	N/A
Time constant between $P_{batt,request}$ and $P_{batt,dis}$	τ_{batt}	0.1	s
Battery charge efficiency	$\eta_{batt,ch}$	0.85	N/A
Battery discharge efficiency	$\eta_{batt,dis}$	1	N/A
Total charge capacity of the battery system	C	200	Ah

3.2.3.4 Traction Model

The traction model, shown schematically in Fig. 3.11, governs the traction power required by the bus ($P_{traction}$) or the power produced from regenerative braking (P_{RB}) using bus velocity (V), acceleration (a) and inclination (θ) [61]:

$$P_{traction} = \frac{V}{\eta_{inv}}\left[ma + \frac{1}{2}C_d\rho AV^2 + mgC_{rr}V + (mg\sin(\tan^{-1}\theta))\right],\ a \geq 0 \quad (3.19)$$

$$P_{RB} = \eta_{rec}V\left[ma + \frac{1}{2}C_d\rho AV^2 + mgC_{rr}V + (mg\sin(\tan^{-1}\theta))\right],\ a < 0. \quad (3.20)$$

Here, η_{inv} is the efficiency of the inverter responsible for conditioning power in the main DC bus to AC power, η_{rec} is the efficiency of the rectifier responsible for conditioning AC regenerative braking power to DC power for charging the battery, m is the vehicle mass, a is the vehicle acceleration, C_d is the bus drag coefficient, ρ is the density of air, A is the vehicle frontal area, g is the gravitational constant, and C_{rr} is the vehicle rolling resistance.

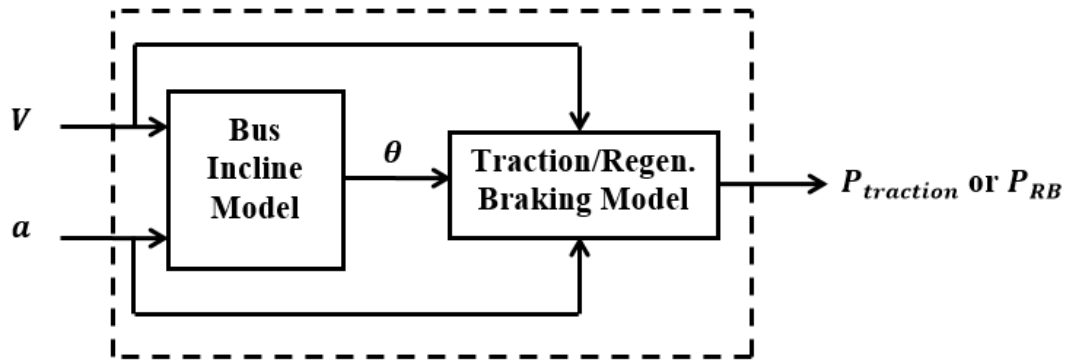

Figure 3.11 Traction model schematic.

If the acceleration of the bus is greater than or equal to zero, then only Eq. 3.19 is used, otherwise only Eq. 3.20 is used. The terms constituting equations Eq. 3.19 and Eq. 3.20 are acceleration, air drag, rolling resistance and inclination, respectively. The bus incline angle is calculated using the difference between the bus acceleration and calculated time derivative of the bus velocity as follows [61]:

$$\theta = \sin^{-1}\left[\frac{1}{g}\left(\frac{dV}{dt} - a\right)\right], \tag{3.21}$$

where $dV/\,dt$ is the calculated time derivative of the bus velocity over one simulation time step. The parameters of the traction model are provided in Table 3.4.

Table 3.4 Traction model parameters.

Description	Symbol	Value	Units
Mass of the bus	m	7830	kg
Coefficient of drag	C_d	0.8	N/A
Density of air at STP and sea level	ρ	1.2041	kg/m^3
Frontal area of the bus	A	4.81	m^2
Gravitational constant	g	9.81	m/s^2
Rolling resistance of the bus	C_{rr}	0.0065	N/A
Efficiency of the Inverter	η_{inv}	0.90	N/A

Efficiency of the Rectifier	η_{rec}	0.90	N/A

3.2.4 Control Strategies

The control objectives of the PV/FC/battery bus are to satisfy the required power demand and maintain the battery SOC at 65%. Thus, the control variables (CVs) for this system are the combined PV array and battery power output ($P_{PV/batt}$) and the measured battery SOC (SOC_m), while the available manipulated variables (MVs) are a signal requesting battery power (P_{batt}^{req}) and a signal requesting FC power (P_{FC}^{req}). The disturbance variables (DVs) in this system, which affect the CVs but cannot be manipulated, are power produced by the PV array (P_{PV}), excess PV power remaining after meeting bus power demands (P_{PV}^{excess}), and power produced from regenerative braking (P_{RB}).

The objective of the control strategy design is to use the MVs to drive the CVs to their desired setpoints despite any uncontrollable fluctuations in the DVs. Because the algebraic and PID control strategies are decentralized control strategies, each use two control loops to meet separately the two control objectives of the bus. The control loops and their CVs, CV setpoints, MVs, and DVs are listed in Table 3.5.

Table 3.5 PV/FC/battery HRES Process Variables

Control Loop	Manipulated Variable (MV)	Controlled Variable (CV)	CV Setpoints	Disturbance Variables (DVs)
1	P_{batt}^{req}	$P_{PV/batt}$	P_{total}	P_{PV}
2	P_{FC}^{req}	SOC_m	SOC_d	P_{PV}^{excess} and P_{RB}

Although each control strategy uses the same control loop structure, they each employ unique algorithms to meet the control objectives of the PV/fuel cell/battery bus. These algorithms are described in detail in the remainder of this Section.

3.2.4.1 Algebraic Control Strategy

The algebraic control strategy, (Bubna *et al*. [55]), consists of two separate controllers as shown in Fig. 3.12, with each controller based on algebraic equations. Algebraic controller 1, which is responsible for meeting the bus power demand, ignores the transient dynamics between P_{batt}^{req} and the battery discharge power (P_{batt}^{dis}). As a result, P_{batt}^{req} is simply

$$P_{batt}^{req} = P_{traction} + P_{accessory} - P_{PV}, \tag{3.22}$$

where $P_{traction}$ is the bus traction power demand and $P_{accessory}$ is the bus accessory power demand (i.e., power required by air conditioning, heating, lighting, etc.). Algebraic controller 2 uses the following equation to calculate the value of P_{FC}^{req} needed to maintain the battery SOC at 65%:

$$P_{FC}^{req} = \{\beta(SOC_d - SOC_m) + P_{avg} - P_{PV}^{excess}, \qquad P_{PV} > P_{total} \tag{3.23a}$$

$$P_{FC}^{req} = \{\beta(SOC_d - SOC_m) + P_{avg}, \qquad P_{PV} \leq P_{total} \tag{3.23b}$$

where β is a proportionality constant (3000 W/%) and P_{avg} is the one-hour time average net power of the battery. Eq. 3.23a is used when P_{PV} exceeds P_{total} since P_{PV}^{excess} helps charge the battery—during deceleration on a sunny day, for example. Eq. 3.23b is otherwise used to calculate P_{FC}^{req}.

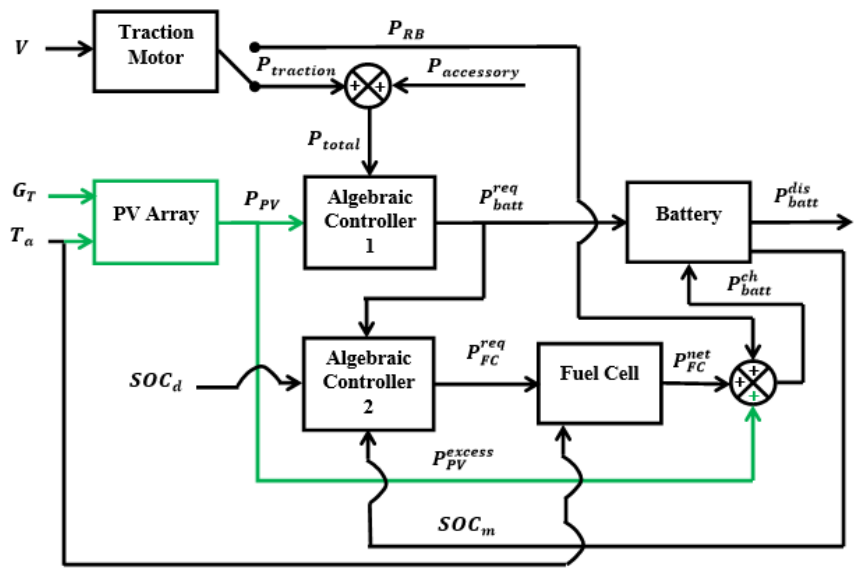

Figure 3.12 Control block diagram of the algebraic control strategy used for the PV/FC/battery HRES. Black blocks and lines indicate components of the original control scheme [55]; green blocks and lines indicate modifications to the original control scheme needed to accommodate a PV array.

3.2.4.2 PID Control Strategy

A control block diagram of the PID control strategy for the PV/FC/battery HRES is shown in Fig. 3.13. In control loop 1, P_{batt}^{req} is calculated using a proportional-integral (PI) controller

$$P_{batt}^{req} = K_{p1}\varepsilon_1 + K_i \int_0^t \varepsilon_1(\tau)d\tau \,. \tag{3.24}$$

Here, K_{p1} is the proportional gain of the total power controller (2.67), K_i is the integral gain of the total power controller (16.83), and ε_1 is the feedback error in control loop 1. No derivative term is included in Eq. 3.24 because rapid changes in bus speed (i.e., bus power demand) are likely to cause the derivative of ε_1 to fluctuate rapidly,

resulting in excessive control action and poor controller performance [62]. In control loop 2, P_{FC}^{req} is calculated using a proportional-only (P-only) controller as follows:

$$P_{FC}^{req} = K_{p2}\varepsilon_2, \tag{3.25}$$

where K_{p2} is the proportional gain of the battery SOC controller (30000 W/%) and ε_2 is the feedback error in control loop 2. A P-only controller suffices for battery SOC control because a step increase in P_{FC}^{req} causes a ramp increase in SOC_m. This accumulation mechanism between P_{FC}^{req} and SOC_m serves as a natural integral action, and, therefore, an integral term is not needed to eliminate offset between SOC_m and SOC_d [62].

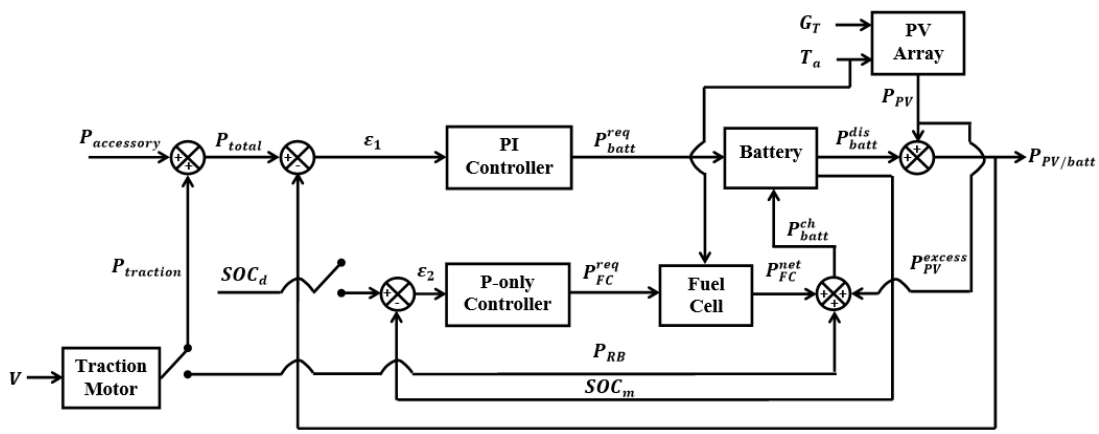

Figure 3.13 Control block diagram of the PID control strategy for the PV/FC/ battery HRES. Control loop 1 uses a PI controller to manipulate P_{batt}^{req}; Control loop 2 uses a P-only controller to manipulate P_{FC}^{req}.

3.2.5 Control Strategy Comparison

The effectiveness of the algebraic and PID control strategies are compared via simulations under three separate operating conditions:

1. typical operating conditions (solar irradiance, vehicle speed, and ambient temperature) during summer and winter;

2. sudden changes in cloud cover; and

3. sustained increase in bus speed.

And the following assumptions:

1. Each PV array module is exposed to the same solar irradiance and ambient temperature.

2. The DC/DC converters, the inverter, and the rectifier operate at steady-state and at 90% efficiency.

3. The battery system is fully charged at the beginning of each simulation.

4. The accessory power demand is constant at 3 kW.

3.2.5.1 Typical Operating Conditions

To compare the performance of the algebraic and PID control strategies for typical operating conditions during summer and winter, the bus operation was simulated using real solar irradiance (Fig. 3.14a), bus speed (Fig. 3.14b), and ambient temperature data over the indicated period. Solar irradiance measurements were obtained at half second intervals while the bus was driven on its typical shuttle route (the UD express route) between 12pm and 3:40pm, using a SP-215 Apogee pyranometer installed on the roof of the bus. The summer data were acquired on July 15th, 2011, the winter data on January 15th, 2012. The bus speed was measured using an onboard GPS device. The summer and winter ambient temperature data (301.24 K and 270.23 K, respectively) are the averages of hourly temperature data collected in Wilmington, DE, by meteorologists at New Castle County Airport between 12pm and 4pm on July 15th, 2011 and January 15th, 2012, respectively.

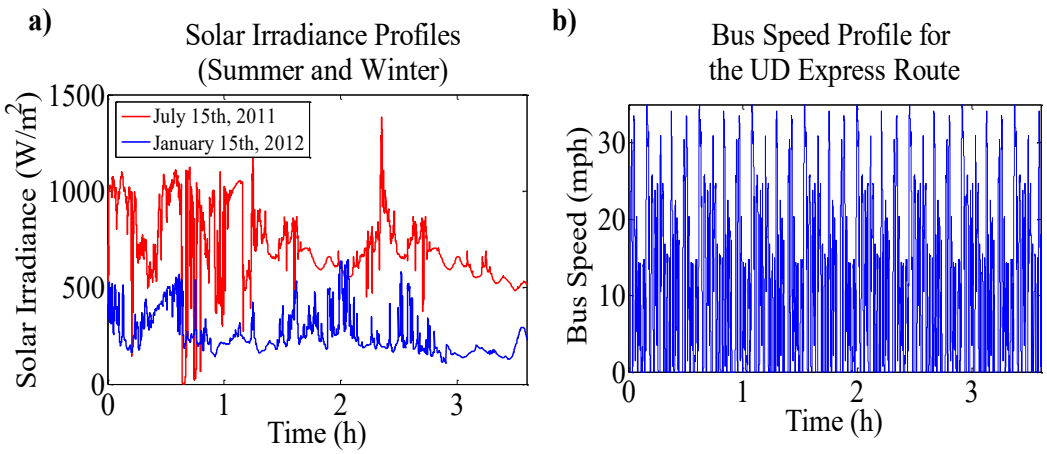

Figure 3.14 **a)** Actual solar irradiance data used to simulate bus operation with a roof-installed PV array, during the summer (red) and winter (blue). **b)** Actual bus speed data used to simulate typical bus traction power demands.

The results of simulating the bus operation under typically observed conditions (Fig. 3.15 and Fig. 3.16) show that under both the algebraic and PID control strategies the bus was able to meet its power demands and maintain battery SOC at 65% reasonably well during typical summer and winter operation. These results indicate that under typically observed conditions, the bus operating objectives are satisfied despite the rapid fluctuations in required bus speed and P_{PV}.

As expected, observe that regardless of the control strategy, the addition of a PV array to the fuel cell/battery bus decreased the amount of hydrogen required by the fuel cell (Fig. 3.17). More specifically, for this particular simulated system, we observe that supplemental PV power reduced hydrogen consumption by about 5% in the winter and by approximately 25% in the summer, for either control strategy.

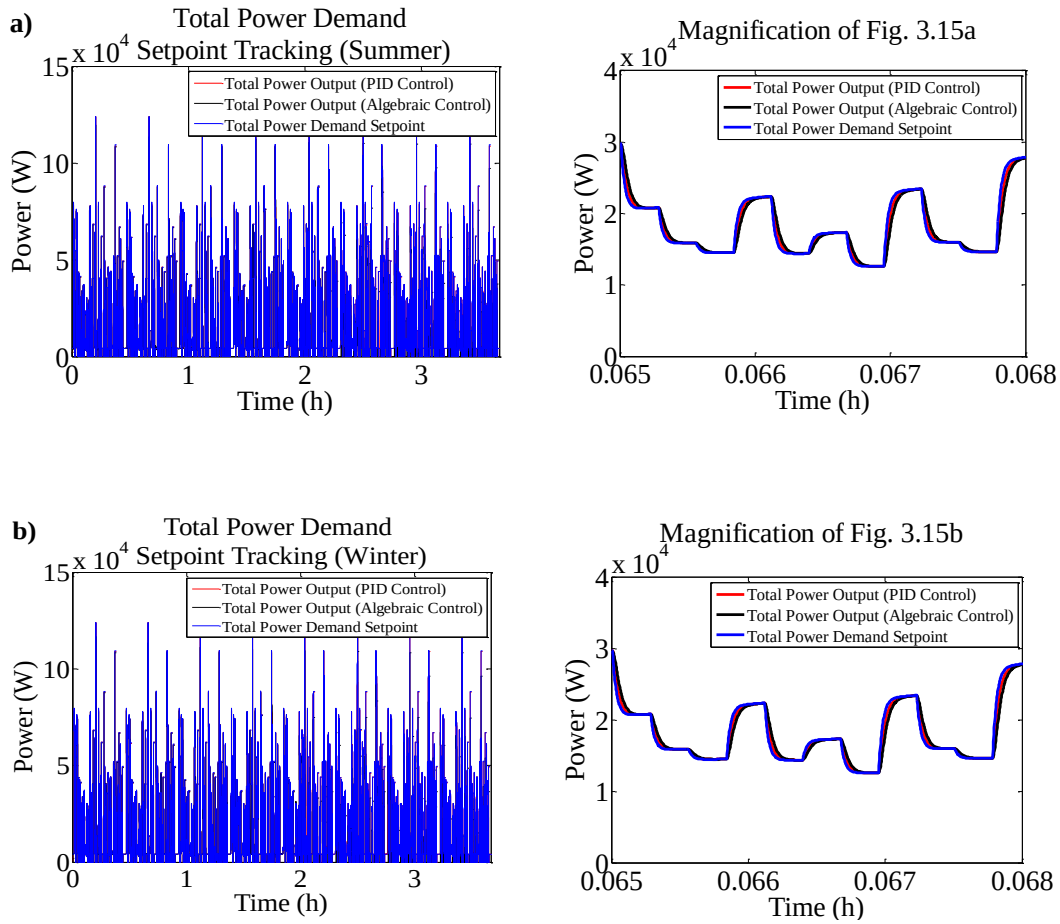

Figure 3.15 Total power demand set-point tracking for the bus using the algebraic and PID control strategies: **a)** summer operation and **b)** winter operation. The magnified plot shows details of controller performance, how rapid changes in bus speed (hence power demands) were tracked reasonably well.

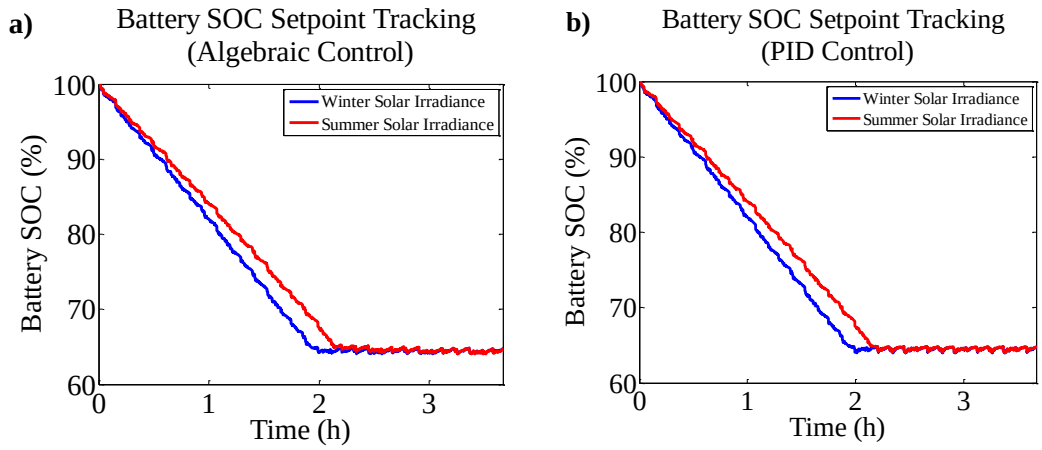

Figure 3.16 Battery state of charge during the 3 hour-40 minute simulation of the PV/fuel cell/battery bus operations under standard conditions: using **a)** algebraic control and **b)** PID control. Each control strategy maintains the battery SOC close to 65% for both summer and winter solar irradiance profiles.

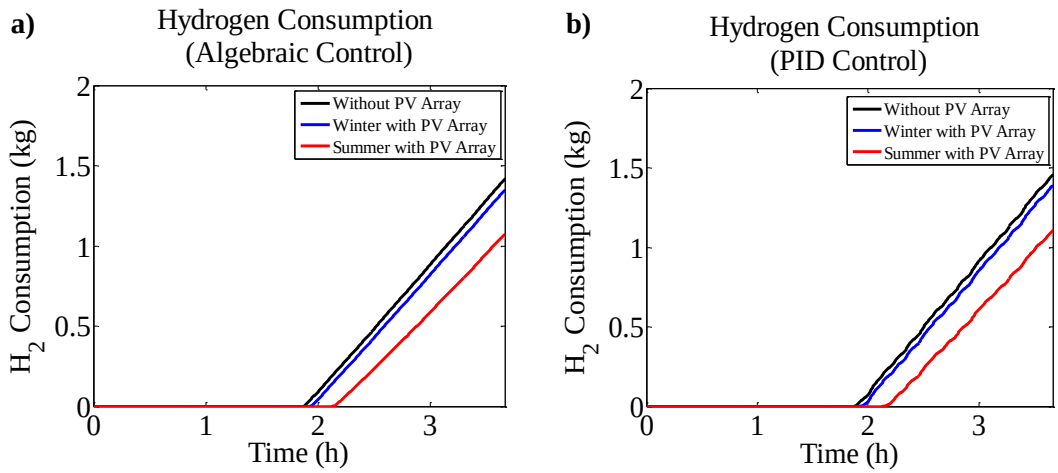

Figure 3.17 Hydrogen consumption profile during the 3 hour-40 minute simulation of the PV/FC/battery bus operation under standard conditions: using **a)** algebraic control and **b)** PID control. The bus consumed approximately the same amount of hydrogen under each control strategy, but hydrogen consumption was reduced by 5% to 25% (winter and summer, respectively) with the addition of a PV array.

3.2.5.2 Sudden Changes in Cloud Cover

To compare the performance of the algebraic and PID control strategies for sudden changes in cloud cover, the bus operation was simulated using constant bus speed (20 mph), constant ambient temperature (301.24 K), and artificial solar irradiance profile (Fig. 3.18) over the indicated period. The artificial solar irradiance data consists of three 30-minute intervals when solar irradiance is decreased from 1000 W/m^2 to 200 W/m^2 and then increased back to 1000 W/m^2. The decrease from 1000 W/m^2 to 200 W/m^2 and subsequent increase from 200 W/m^2 to 1000 W/m^2 simulate an instantaneous increase and decrease in cloud cover, respectively.

Fig. 3.19 shows the results of simulating bus operation under sudden changes in cloud cover. As shown in Fig. 3.19a, the algebraic and PID control strategies each enable the bus to meet its power demands well enough for practical purposes (settling time of less than 1 second) despite instantaneous changes in simulated cloud cover (hence P_{PV}). However, magnifying Fig. 3.19a at the moment of sudden change in cloud cover reveals that the bus can meet its power demands marginally better under PID control than under algebraic control. Additionally, under the algebraic and PID control strategies, the bus maintained battery SOC at 65% (Fig. 3.19b) and, in doing so, consumed approximately the same amount of hydrogen (Fig. 3.19c). Our results suggests that when sudden changes in cloud cover are expected, bus operation under algebraic or PID control is nearly identical.

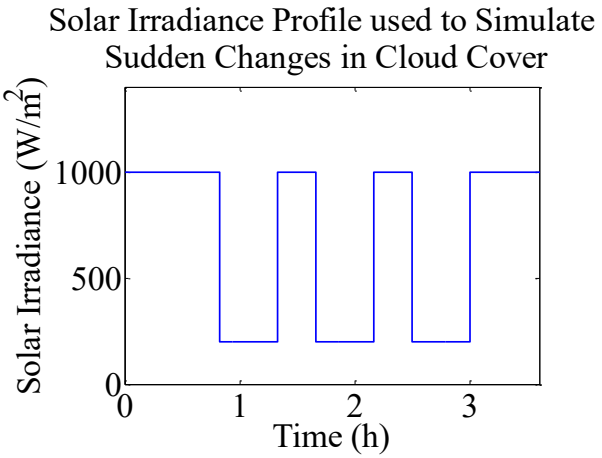

Figure 3.18 Artificial solar irradiance profile used to simulate bus operation with a roof-installed PV array. Solar irradiance is instantaneously decreased from 1000 W/m^2 to 200 W/m^2 three times for 30-minute intervals during the 3 hour-40 minute simulation of the bus.

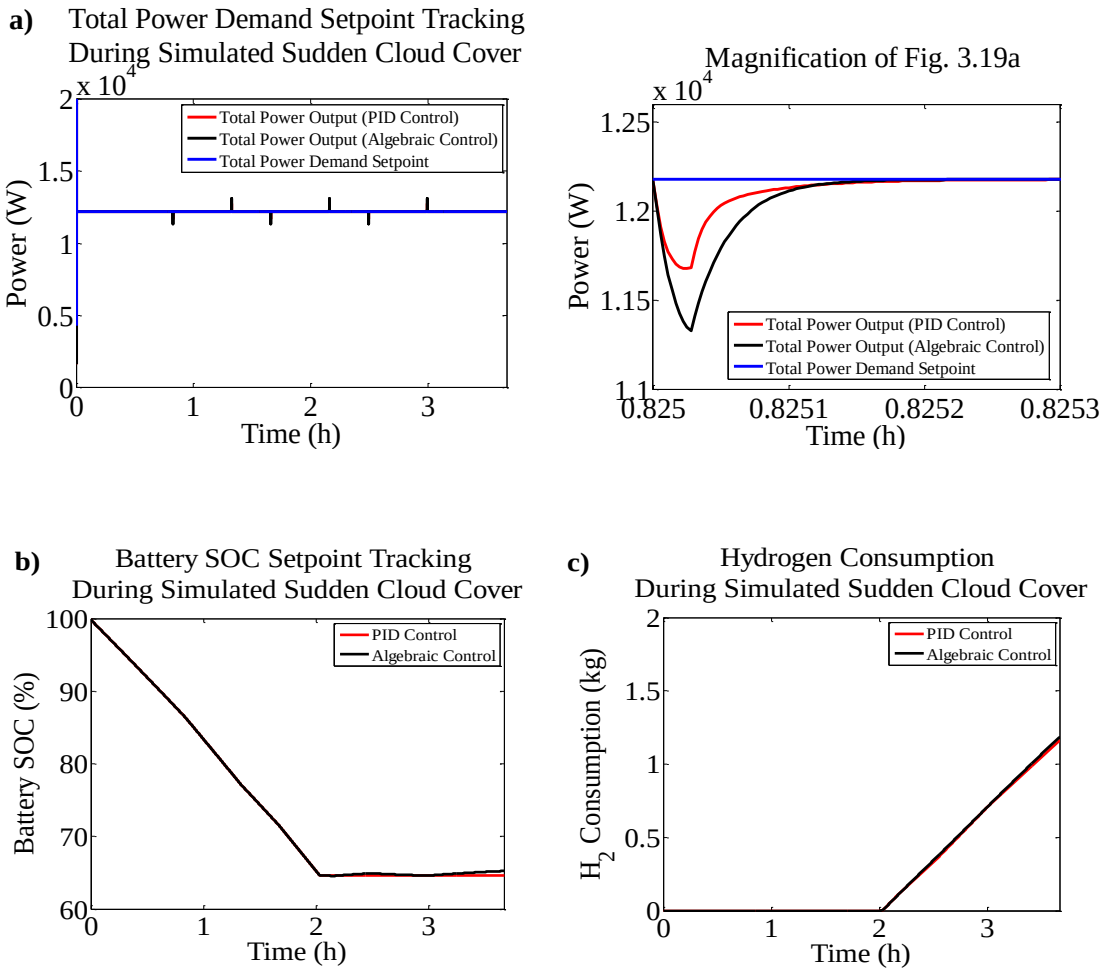

Figure 3.19 Results of simulating bus operation under sudden changes in cloud cover: **a)** Total power demand set-point tracking with a magnified plot illustrating details; **b)** battery SOC set-point tracking; and **c)** hydrogen consumption profile. The bus was able to meet its power demands under algebraic and PID control reasonably well despite large and abrupt changes in solar irradiance, but power demands were met slightly better under PID control than under algebraic control. The bus was able to maintain battery SOC at 65% while consuming approximately the same amount of hydrogen under each control strategy.

3.2.5.3 Sustained Increases in Bus Speed

To compare the performance of the algebraic and PID control strategies under sustained increases in bus speed, the bus operation was simulated using constant solar

irradiance (700 W/m^2), constant ambient temperature (301.24 K), and an artificial bus speed profile (Fig. 3.20). The artificial bus speed profile comprises two separate periods where bus speed is increased from 20 mph to 45 mph (the maximum bus speed) for 30 minutes and then decreased from 45 mph to 20 mph. Although such a speed profile is not characteristic of a typical bus shuttle run, a similar situation may arise when the bus needs to remain at maximum speed for an extended period of time to reach a desired destination.

Fig. 3.21 shows the results of simulating the bus operation under sustained increases in bus speed. As expected, observe that under sustained increases in bus speed, algebraic and PID control each enabled the bus to meet power demands well enough for practical purposes (Fig. 3.21a). However, upon closer investigation of a magnification of Fig. 3.20a during the first transition from 20 mph to 45 mph, PID control yielded slightly improved total power demand set-point tracking. As shown in Fig. 3.21b, under both algebraic and PID control the bus was not able to maintain battery SOC at 65% when the bus velocity was increased to 45 mph because the battery discharge power required to maintain a 45 mph speed exceeds the sum of P_{PV} and maximum fuel cell power. Each time the bus speed was reduced to 20 mph after remaining at 45 mph for 30 minutes, battery SOC recovered to its desired value of 65% under PID control while battery SOC overshoots first to ~67% and then to nearly 70% under algebraic control. The overshoot is a result of the drastic increase in P_{avg} that occurred when the bus reached its maximum speed for 30 minutes, causing algebraic controller 2 to produce a value of P_{FC}^{req} much larger than needed to maintain battery SOC at 65% (see Eq. 3.23a and 3.23b). Additionally, the overestimation of $P_{FC,request}$ by algebraic controller 2 in this case causes 5% more hydrogen to be

consumed than is needed to maintain the battery SOC at 65% (Fig. 3.21c). Therefore, when the bus is subjected to sustained increases in bus speed, the PID control strategy has two advantages over the algebraic control strategy: better battery SOC setpoint tracking and reduced hydrogen consumption.

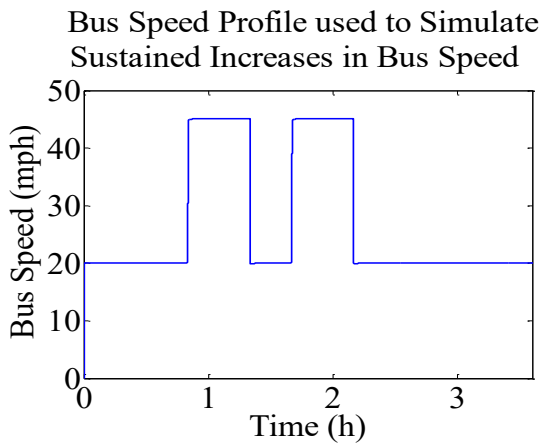

Figure 3.20 Artificial bus speed profile used to simulate bus operation with a roof-installed PV array. The profile contains two, 30-minute periods where bus speed is increased from 20 mph to 45 mph (the maximum bus speed) and subsequently decreased to 20 mph.

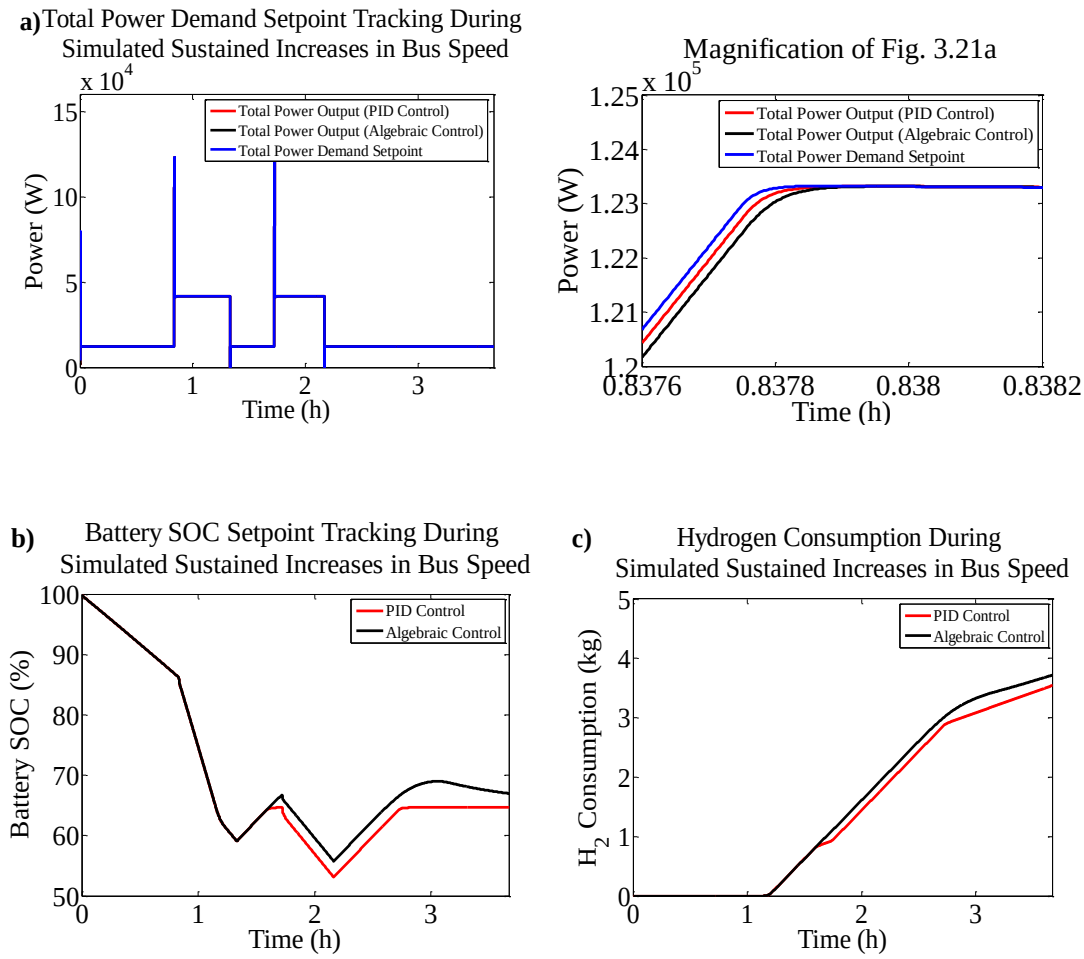

Figure 3.21 Results of simulating bus operation under sustained increases in bus speed: **a)** total power demand set-point tracking with a magnified plot illustrating details; **b)** battery SOC set-point tracking; and **c)** hydrogen consumption profile. The bus was able to meet its power demands under algebraic and PID control reasonably well despite large and abrupt changes in bus speed, but power demands were met slightly better using PID control. The bus was able to maintain battery SOC at 65% only under PID control, while algebraic control caused an overshoot of battery SOC to almost 70%. As a result, observe that the simulated bus under PID control consumed 5% less hydrogen than if the bus operated under algebraic control.

3.2.6 Economic Analysis

To ensure that the PV array modification described in this work is profitable under varying conditions and to provide expected profits from future PV array designs, we used Eq. 3.1 to obtain the ROI for a range of feasible values for $G_{T,avg}$ (300 W/m^2, 500 W/m^2, and 700 W/m^2), S_{PV} (5 m^2 – 50 m^2), and η_{PV} (5% – 50%). Each calculation was completed under the following assumptions:

1. The total cost (the sum of capital, shipping, and installation costs) of the PV array is \$4810[7].
2. The PV array costs \$1775 after deducting federal[8] and Delaware[9] state tax incentives [47,48].
3. Cost of hydrogen remains constant at \$3.43/kg [63].
4. The bus is only available to operate 60% of days throughout the year (average bus availability from reported fuel cell hybrid shuttle buses in 2014) [64].
5. On days when the bus does operate, it does so from 12pm to 3:40pm along the UD express route.
6. Operational lifetime of the bus is 12 years (DOE 2016 target) [64].
7. The battery is fully charged at the start of each shuttle run.
8. The bus uses the PID control strategy described in Section 3.2.4.2

Fig. 3.22 shows the PV array ROI as a function of PV array efficiency (η_{PV}) and size (S_{PV}) for varying levels of average solar irradiance during bus operation

---

[7] Capital cost = \$475 per PV module, shipping cost = \$60, and installation cost = 25% of module cost

[8] 30% of total installed costs

[9] \$0.45/W-rated - \$0.90/W-rated, but average of \$0.675/W-rated was used in this work

($G_{T,avg}$). As shown in Fig. 3.22a, when $G_{T,avg}$ = 300 W/m^2—a condition expected for geographic locations consistently deprived of solar irradiance—the ROI for the PV array used in this work is approximately -20% (~$370 loss). Because a profit is not expected from our design when $G_{T,avg}$ = 300 W/m^2, we do not recommend retrofitting the fuel cell/battery bus with the PV array described in this work in geographic locations where such conditions are expected. Instead, the PV array should only be added to the existing bus under such conditions if C_{PV} remains $1775, while η_{PV} and/or S_{PV} are high enough to yield a positive ROI according to Fig. 13a. However, Fig. 3.22b indicates that when $G_{T,avg}$ = 500 W/m^2—a condition expected for geographic locations having a similar climate to Newark, DE—the PV array described in this work yields a 30% ROI ($550 profit). As expected, Fig. 3.22c shows that even larger profits can result from the PV array addition when $G_{T,avg}$ = 700 W/m^2—a condition expected for geographic locations having high exposure to sunlight year-round. More specifically, under such conditions, the PV array described in this work provides 80% ROI (~$1,470 profit). We therefore recommend implementing the PV/FC/battery bus described in this study in Newark, DE, and other geographic locations having greater than 500 W/m^2 of average solar irradiance during bus operation.

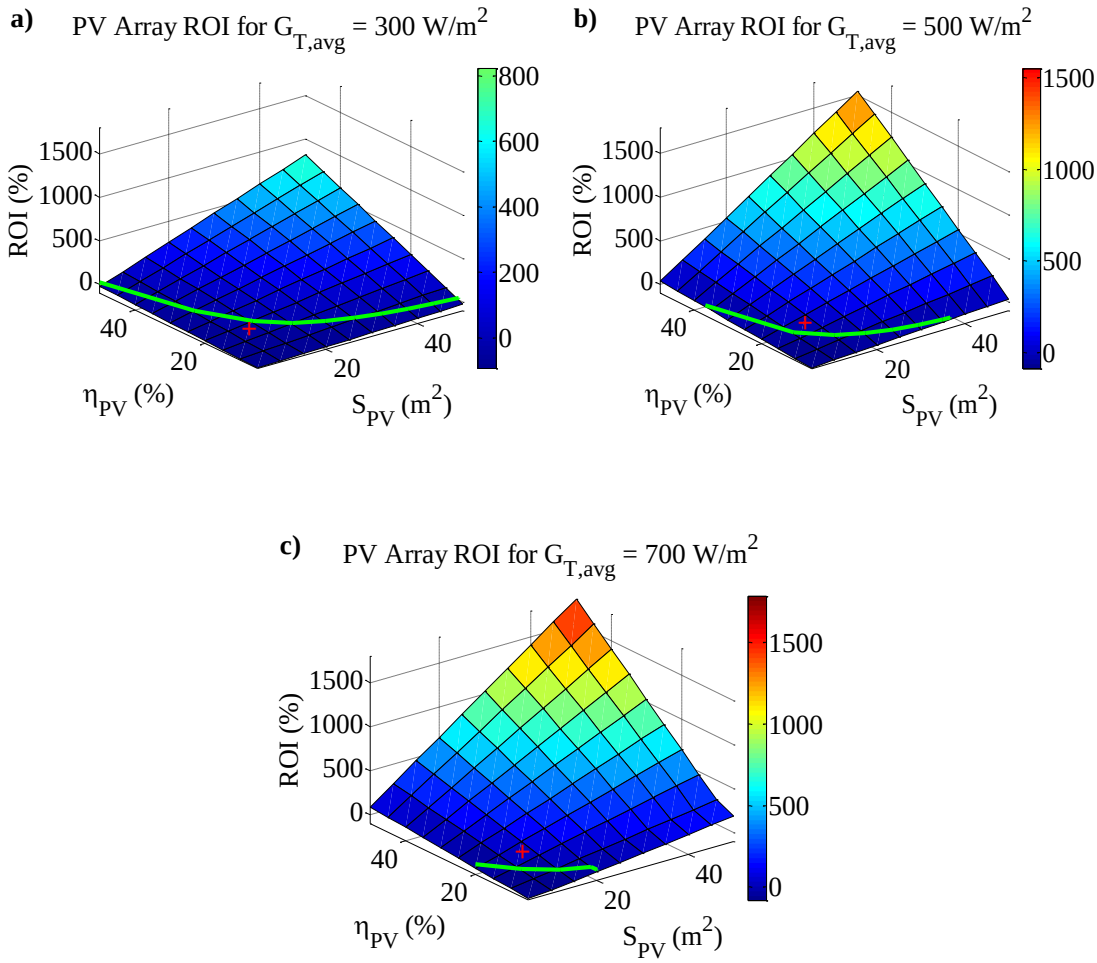

Figure 3.22 Plots of ROI versus PV efficiency (η_{PV}) and PV surface area (S_{PV}) for average solar irradiance during bus operation ($G_{T,avg}$) of: **a)** 300 W/m^2; **b)** 500 W/m^2; and **c)** 700 W/m^2. The green line in each figure represents the intersection between the ROI = 0% plane and the surface plot of ROI. The red plus sign in each figure corresponds to the PV array used in this work (η_{PV} = 18.3% and S_{PV} = 13.12 m^2). For the PV array used in this work, if $G_{T,avg}$ = 300 W/m^2 the ROI is -20%, while for $G_{T,avg}$ = 500 W/m^2 and 700 W/m^2 the ROI is 30% and 80%, respectively.

3.3 Chapter Summary and Conclusions

In this chapter, we established two principles regarding the design, operation and control of HRESs. The two principles are states as follows: "*By default, the*

components of a HRES should be arranged in parallel for increased efficiency and reliability. However, a series HRES design may be preferred depending on the operational considerations of the HRES components." and "*Choice of control strategy for a HRES (e.g., state control, PID control, or MPC) depends on the dynamics of HRES components, their operational considerations, and the practical limitations of the HRES end-use."* In addition to principle 1, these two principles were demonstrated by evaluating the design, operation, control, and economic implications of adding a PV array to an existing FC/battery HRES for automotive applications.

First, we compared the operation of a PV/FC/battery bus under algebraic and PID control by simulating the bus under typically observed conditions during summer and winter, sudden changes in cloud cover, and sustained increases in bus speed. For typical operating conditions during summer and winter, we showed that each control strategy enabled the PV/FC/battery HRES to meet bus power demands and maintain the battery SOC at 65%. Furthermore, simulations of bus operation under typically operating conditions indicate that the addition of a PV array to the existing fuel cell/battery bus reduced hydrogen consumption by 10% to 35%. During sudden changes in cloud cover, the algebraic and PID control strategies enabled the bus to meet its power demands and maintain battery SOC at 65% while consuming approximately the same amount of hydrogen. However, when the bus undergoes sustained increases in speed, the PID control strategy allowed the bus to better maintain battery SOC at 65% and consume about 5% less hydrogen than the bus under algebraic control. Therefore, the PID control strategy is the preferred candidate control strategy for the PV/FC/battery bus because of its ability to meet bus operating objectives under a variety of operating conditions.

In addition, an economic analysis was completed to determine the values of $G_{T,avg}$, S_{PV}, and η_{PV} required for positive ROI. When $G_{T,avg}$ was 300 W/m^2, the ROI for the PV array design described in this study (S_{PV} = 13.12 m^2 and η_{PV} = 18.3%) was approximately -20%, implying that the PV/fuel cell/battery bus should not be implemented in locations having such low exposure to sunlight when the bus is expected to operate (between 12pm and 3:40pm). However, when $G_{T,avg}$ was greater than 500 W/m^2, the ROI was positive and profits are expected (500 W/m^2: 30% ROI, 700 W/m^2: 80% ROI). Because the bus is likely to be exposed to an average of at least 500 W/m^2 of solar irradiance during operation in Newark, DE, we recommend the PV/fuel cell/battery bus design described in this paper be implemented at the University of Delaware. Overall, it is recommended that if $G_{T,avg} \geq 500$ W/m^2, one can expect the PV array modification to the FC/battery bus to more than pay for itself while producing zero harmful emissions.

Chapter 4

DATA-DRIVEN ADVANCED CONTROL OF HRESS

4.1 Introduction

Although the previous Chapter presents and demonstrates the general design, operation, and control guidelines for HRESs, some HRESs—typically those having little or no computational constraints—can take advantage of certain advanced control practices. In particular, the concept of data-driven control is appealing for HRESs because large quantities of data from these systems are available virtually continuously and, in some cases, nearly instantaneously. For our purposes, the most important implication of this fact is that the fundamental dynamic relationships between system inputs and system outputs are contained in these often information-rich data sets, so that any changes in system characteristics will also be reflected in the information contained in the data. Our premise is that this fact should be exploited, when computational effort can be afforded, for effective design of control systems that will adapt seamlessly to changing conditions in order to deploy the most effective operation regardless of prevailing conditions. Therefore, we can state the following principle regarding data-driven advanced control of HRESs:

Principle 4: *Information-rich data should be used to assist in the intelligent coordination of HRES components in meeting its operating objectives when additional computation can be afforded and significant benefits can be realized.*

It is worth noting that this control principle can be applied to two classes of control schemes: decentralized control and centralized control. In decentralized

control (e.g., PID control), the control of multivariable processes is accomplished using multiple controllers, with each controller maintaining the setpoint of a single controlled variable using a single manipulated variable. This control system paradigm is preferred for systems requiring high computational speed, low costs, and robust control when a processing unit fails. On the contrary, centralized control (e.g., MPC) contains a single global controller that is responsible for controlling all process outputs using all available manipulated variables. Because centralized control operates using a more complex algorithm than decentralized control, it is usually preferred in systems that do not necessarily require high computational speed and low cost [65].

In this Chapter, we aim to demonstrate the use of Principle 4 by using data to help dictate adaptive control action in both a decentralized and centralized control strategy. We will do so by presenting two separate case studies that demonstrate Principle 4. The first case study describes a data-driven decentralized control strategy (Section 4.2) while the second case study describes a data-driven centralized control strategy (Section 4.3).

4.2 Data-driven Decentralized Control: On-line Determination of Appropriate Control Loop Configuration using Directed Spectral Decomposition

4.2.1 Overview

An important part of designing effective decentralized multivariable control schemes is determining control loop configurations (CLCs) that minimize control loop interactions. Traditionally, the most appropriate CLC is often determined using either the relative gain array [66] or the dynamic relative gain array [67] of a process obtained at a single operating condition, with the configuration remaining unchanged for the duration of any subsequent process operation. For systems having significant

non-linear characteristics, however, a designated CLC may no longer be appropriate at new operating conditions, leading to poor control system performance and potential closed-loop instability—a situation that can be avoided if control loops can be appropriately reconfigured.

As an example of a process that undergoes a change in the most appropriate CLC, consider the non-linear 3-input, 3-output stirred mixing tank process shown schematically in Fig. 4.1. Based on a 2-input, 2-output stirred mixing tank example [62], the process consists of three input variables: a hot stream flowrate (F_H), a cold stream flowrate (F_C), and a brackish stream flowrate (F_B). These three input variables can be used to control independently the tank's three output variables: the liquid level (h), the liquid temperature (T), and the salt concentration (C). The hot stream, cold stream, and brackish stream are each maintained at a constant temperature (T_H, T_C, and T_B, respectively) and a constant salt concentration (C_H, C_C, and C_B, respectively). At the bottom of the tank an orifice allows liquid to leave at a flowrate expressed as $F(h)$.

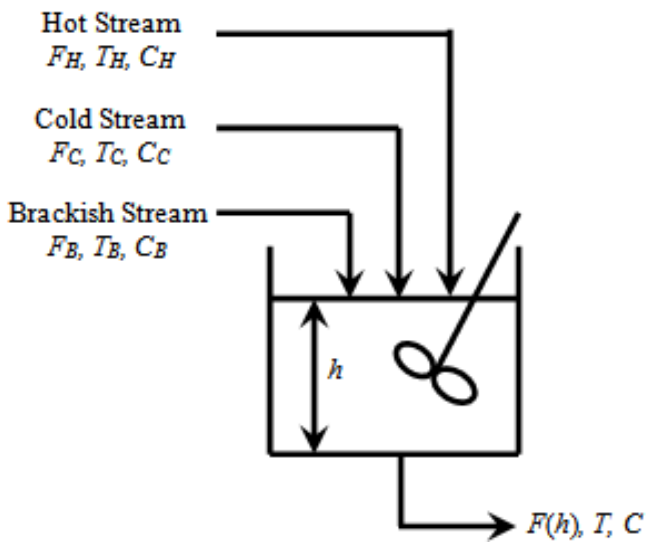

Figure 4.1 Schematic of the 3-input, 3-output stirred mixing tank process. A hot stream, cold stream, and brackish stream each affect liquid level height in the tank (h), liquid temperature (T), and salt concentration (C).

The assumption that all three input streams have equal and constant density and heat capacity yields the following intuitive determination: if ($T_H - T$) is greater than ($T_C - T$) and ($T_B - T$), and ($C_B - C$) is greater than ($C_H - C$) and ($C_C - C$), then F_H should be used to control T and F_B should be used to control C. The remaining input variable, F_C, can be used to control h because each flowrate has an identical influence on the tank's liquid level. Under such conditions, controller configuration 3 (Fig. 4.2) minimizes control loop interactions of the stirred mixing tank.

If the operating temperature of the tank changes, however, such that ($T_C - T$) is greater than ($T_B - T$) and ($T_H - T$), F_C should then be used to control T, F_B should continue to be used to control C, and F_H should be used to control h. Hence, under this new operating condition, the most apposite CLC of the stirred mixing tank changes from configuration 3 to configuration 1 (Fig. 4.2).

Configuration 1	Configuration 2	Configuration 3
F_H—h	F_H—h	F_C—h
F_C—T	F_B—T	F_H—T
F_B—C	F_C—C	F_B—C

Configuration 4	Configuration 5	Configuration 6
F_B—h	F_C—h	F_B—h
F_H—T	F_B—T	F_C—T
F_C—C	F_H—C	F_H—C

Figure 4.2 Possible control loop configurations of the 3-input, 3-output stirred mixing tank process.

Although the most suitable CLC of the stirred mixing tank can be determined intuitively, we hypothesize that information-rich data can be used to seamlessly reconfigure control loops online in any process having significant non-linear characteristics. Our goal therefore is to develop and evaluate an online data-driven procedure for determining the most suitable CLC of a process. For this purpose, we used directed spectral decomposition (DSD)—a spectral analysis technique that uses informative process data to determine the total energy transferred between process variables [68]—to ascertain connection strength between process variables in a simulation of the stirred mixing tank. Following statistical validation of connection-strength estimates, these estimates were then used to determine a CLC that would minimize control loop interactions at the current operating conditions.

4.2.2 Procedure Development

4.2.2.1 Directed Spectral Decomposition

Directed spectral decomposition, a linear spectral analysis technique using dynamic process data to quantify causal relationships (i.e., total energy transferred)

between process variables, has previously been used to determine connectivity in processes having unknown connections between variables [68]. Before employing DSD, white Gaussian noise (WGN) must be added to each variable. When added to process inputs WGN generates informative data; when added to process outputs it simulates output measurement noise (only required in simulations). The WGN has a mean of zero and a variance that must be carefully selected such that collected process data is informative without detrimentally perturbing the system.

Next, data collected from the process is used to estimate the coefficients of a unique A-form structural vector autoregressive (SVAR) model represented as:

$$x[k] = A_0^{-1} \sum_{r=1}^{p} A_r x[k-r] + A_0^{-1} e[k]\,, \tag{4.1}$$

where x$[k]$ is a vector of data measurements taken from a process at time k, p is the model order selected using the Akaike Information Criterion (AIC) [69], A_r is the matrix of auto-regressive coefficients at lag r (estimated using least squares), e$[k]$ is a vector of white noise sequences, and A_0 is a matrix containing the instantaneous relationships between variables [70]. Because A_0 only contains information regarding instantaneous relationships between variables (i.e., the direct effect of process outputs on process inputs via closed-loop feedback control), it is estimated only when a process is under closed-loop feedback control. In practice, A_0 can be estimated uniquely using maximum-likelihood estimation [70].

After estimating A_r and A_0, the transfer function matrix is calculated from:

$$A(\omega) = \sum_{r=1}^{p} A_r z^{-r}|_{z=e^{j\omega}}\,, \tag{4.2}$$

$$\bar{A}(\omega) = I - A(\omega), \tag{4.3}$$

$$H(\omega) = \bar{A}^{-1}(\omega), \tag{4.4}$$

and

$$\widetilde{H}(\omega) = H(\omega)A_0^{-1}, \tag{4.5}$$

where Eq. 4.2 is the Fourier transform of A_r [71]. The transfer function matrix can be re-written in expanded form as:

$$\widetilde{H}(\omega) = \begin{bmatrix} \tilde{h}_{11}(\omega) & \tilde{h}_{12}(\omega) & \cdots & \tilde{h}_{1j}(\omega) \\ \tilde{h}_{21}(\omega) & \tilde{h}_{22}(\omega) & \cdots & \tilde{h}_{2j}(\omega) \\ \vdots & \vdots & \ddots & \vdots \\ \tilde{h}_{i1}(\omega) & \tilde{h}_{i2}(\omega) & \cdots & \tilde{h}_{ij}(\omega) \end{bmatrix}, \tag{4.6}$$

where the jth column corresponds to the jth source variable (i.e., the variable influencing a connection sink) and the ith row corresponds to the ith sink variable (i.e., the variable influenced by a connection source) [72]. Because all process inputs and outputs are considered potential connection sources and sinks, $\widetilde{H}(\omega)$ is a 6 x 6 matrix for the 3-input, 3-output stirred mixing tank.

The transfer function matrix is then used to calculate total energy transferred from one variable to another. In this context, total energy transfer is a measure of a connection source's influence on a connection sink at a given frequency (total energy transfer does not refer to electrical energy). The total energy transferred from the jth source variable to the ith sink variable is the sum of direct energy transfer, indirect energy transfer, and an interference effect between direct and indirect energy transfer given by:

$$\left|\tilde{h}_{ij}(\omega)\right|^2 = \left|\tilde{h}_{D,ij}(\omega)\right|^2 + \left|\tilde{h}_{I,ij}(\omega)\right|^2 + \tilde{h}_{IF,ij}(\omega), \tag{4.7}$$

where $\tilde{h}_{D,ij}(\omega)$ is the direct transfer function, $\tilde{h}_{I,ij}(\omega)$ is the indirect transfer function, and $\tilde{h}_{IF,ij}(\omega)$ is the interference effect [4].

4.2.2.2 Quantification, Validation, and Statistical Significance of Connection Strength Estimates

After obtaining the total energy transfer estimates between process variables, these estimates are used to quantify the connection strength between process variables, determined as follows:

$$\psi_{ij} = \int_0^{\pi} \left|\tilde{h}_{ij}(\omega)\right|^2 d\omega, \tag{4.8}$$

where ψ_{ij} is a scalar value of the directional connection strength between the jth source variable and the ith sink variable. Thus, the matrix of connection strengths between variables is

$$\Psi = \begin{bmatrix} \psi_{11} & \psi_{12} & \cdots & \psi_{1j} \\ \psi_{21} & \psi_{22} & \cdots & \psi_{2j} \\ \vdots & \vdots & \ddots & \vdots \\ \psi_{i1} & \psi_{i2} & \cdots & \psi_{ij} \end{bmatrix}. \tag{4.9}$$

The connection strength estimates in Eq. 4.9 can be used to determine the most appropriate CLC of a process only if the white noise sequences in Eq. 4.1 are uncorrelated—a requirement for SVAR model accuracy [73]. A common mathematical representation of correlation between two data sets is the Pearson correlation coefficient:

$$\rho_{ij} = \frac{cov(i,j)}{\sigma_i \sigma_j}. \tag{4.10}$$

Here, ρ_{ij} is the Pearson correlation coefficient between the ith and j^{th} white noise sequence ($-1 \leq \rho_{ij} \leq 1$), $cov(i,j)$ is the covariance between the ith and j^{th} white noise sequence, σ_i is the standard deviation of the ith white noise sequence, and σ_j is the standard deviation of the jth white noise sequence [74]. Therefore, connection strength estimates calculated in Eq. 4.9 are only valid when the Pearson correlation coefficient matrix (P) of white noise sequences is an identity matrix given by:

$$P = \begin{bmatrix} \rho_{11} & \rho_{12} & \cdots & \rho_{1j} \\ \rho_{21} & \rho_{22} & \cdots & \rho_{2j} \\ \vdots & \vdots & \ddots & \vdots \\ \rho_{i1} & \rho_{i2} & \cdots & \rho_{ij} \end{bmatrix} = \begin{bmatrix} 1 & 0 & \cdots & 0 \\ 0 & 1 & \cdots & 0 \\ \vdots & \vdots & \ddots & \vdots \\ 0 & 0 & \cdots & 1 \end{bmatrix}. \tag{4.11}$$

Because each white noise sequence is perfectly correlated with itself, the diagonal elements of P are 1. The off-diagonal elements of P are deemed statistically insignificant using a statistical hypothesis test (Appendix A). If there is no evidence to suggest that the off-diagonal elements of P are not significantly different from zero, then connection strength estimates are valid. Otherwise, the variance of WGN added to process input variables must be adjusted, connection strengths estimated, and another hypothesis test performed. This procedure continues until P has no statistically significant off-diagonal elements.

Following the validation of connection strength estimates, it is necessary to determine which of those estimates are statistically significant. For this purpose, the 99% statistical significance thresholds of the connection strength estimates are calculated by developing a distribution for each estimate assuming no true connections exist between process variables (i.e., only WGN is present in the collected process data) [75]. Distributions for each connection strength estimate can be developed from surrogate data sets generated using phase randomization—a surrogate data generation technique retaining the power spectrum and autocorrelation of the original data set [76]. If a connection strength estimate is less than the 99% significance threshold, it is deemed insignificant and is set equal to zero in subsequent calculations for determining the most appropriate CLC.

4.2.2.3 Identification of the Most Appropriate CLC

After connection strengths are calculated, validated, and evaluated for statistical significance, they can be used to ascertain the most appropriate CLC for a process by following three steps. First, the elements of Ψ are normalized to the highest value of connection strength within an element's row, a normalization represented mathematically as:

$$\varphi_{ij} = \left.\frac{\psi_{ij}}{max(\psi_{i1}, \psi_{i2}, \dots, \psi_{in})}\right|_{\substack{i=1,2,\dots,m \\ j=1,2,\dots,n}}, \tag{4.12}$$

where φ_{ij} is the row-normalized connection strength between the jth process input and the ith process output ($0 \leq \varphi_{ij} \leq 1$), m is the number of process outputs, and n is the number of process inputs. Second, the row-normalized connection strengths are used to quantify the relative effect of process inputs on each process output:

$$\Gamma_i = \left.\sum_{j=1}^{n} \frac{(1-\varphi_{ij})}{(n-1)}\right|_{i=1,2,\dots,m}, \tag{4.13}$$

where Γ_i is referred to as the interaction factor of the ith process output. Thus, if all process inputs have equal influence on the ith process output (i.e., $\{\varphi_{i1}, \varphi_{i2}, \dots, \varphi_{in}\} = 1$), then $\Gamma_i = 0$, and prominent closed-loop interactions are expected when controlling the ith process output. If, however, only one process input has an effect on the ith process output then $\Gamma_i = 1$, and no significant closed-loop interactions are expected when controlling the ith process output. It is worth noting that $0 \leq \Gamma_i \leq 1$, except when $\{\varphi_{i1}, \varphi_{i2}, \dots, \varphi_{in}\} = 0$. Under such conditions, $\Gamma_i = n/n - 1$ and the ith process output cannot be controlled. The final step for identifying the most appropriate CLC is to pair, in descending order of interaction factor, each process *output* with an unpaired process *input* corresponding to the highest value of connection strength to the process output under consideration. If two interaction factors are equal (e.g., $\Gamma_1 = \Gamma_2$), priority

is given to the output variable having the highest connection strength corresponding to an unpaired input variable. The input-output control loop pairing procedure continues until no further pairings can be made.

4.2.3 Procedure Execution

The data-driven control loop reconfiguration procedure described previously in Section 4.2.2 should be executed only when control system performance has significantly degraded such that a) process input variation (i.e., control action) around an expected value is deemed excessive; or b) process output variation around a prescribed setpoint is deemed excessive. Accordingly we have developed separate control system performance metrics for process inputs and outputs that can be used to detect, in real time, when reconfiguration is needed. The control system performance metric for process inputs is defined as:

$$\Theta_j = \frac{\int_0^{\delta} \left(u_j^{SS} - u_j\right)^2 dt}{\int_0^{\delta} \left(u_{j,0}^{SS} - u_{j,0}\right)^2 dt}, \tag{4.14}$$

where Θ_j is the control system performance metric for the jth process input, u_j^{SS} is a vector containing the most recent steady-state values of the jth process input anticipated for current operating conditions, u_j is a vector containing the most recent values of the jth process input over time under current operating conditions, $u_{j,0}^{SS}$ is u_j^{SS} under initial process operating conditions, $u_{j,0}$ is a vector containing values of the jth process input over time under initial process operating conditions, and δ is the time over which the data was collected. Similarly, we define the control system performance metric for process outputs as:

$$\Theta_i = \frac{\int_0^{\delta} \left(y_i^{SP} - y_i\right)^2 dt}{\int_0^{\delta} \left(y_{i,0}^{SP} - y_{i,0}\right)^2 dt}, \tag{4.15}$$

where Θ_i is the control system performance metric for the ith process input, y_i^{SP} is a vector of the most recent setpoint values of the ith process input, y_i is a vector containing the most recent values of ith process input over time under current operating conditions, $y_{i,0}^{SP}$ is y_i^{SP} under initial process operating conditions, and $y_{i,0}$ is a vector containing values of a process output over time under initial process operating conditions.

There are two properties of Θ_j and Θ_i worth noting. First, the size of u_j^{SS}, u_j, y_i^{SP}, and y_i all remain constant. As new data is collected, the newest data point for each of these vectors is added while the oldest is deleted. This "moving window," which is equal in size to the number of data points collected over δ, ensures that only the most recent control system performance is accounted for in each calculation. Second, denominators of Θ_j and Θ_i are constant, corresponding to the control system performance under initial operating conditions. Therefore, when Θ_j = 1 or Θ_i = 1, the corresponding input or output variable, respectively, has identical control system performance at current operating conditions as compared to initial operating conditions. If the Θ_j = 1 or Θ_i = 1 is less than 1, current control system performance is better than that under initial operating conditions. Conversely, when Θ_j = 1 or Θ_i = 1 is greater than 1, current control system performance is worse than that under initial operating conditions.

We propose that input and output variation is deemed excessive, and therefore control loops must be reconfigured, if Θ_j > 2 or Θ_i > 2 after the process has reached steady-state following a disturbance or change in desired operating conditions. When

such a condition is met in a real process, an alarm would be triggered and an operator would verify its cause. If the operator determines the alarm to be a result of poor control system performance, 1000 samples of input and output data would be collected at current operating conditions and the procedure described in Section 4.3.2 executed. The recommended CLC would then verified by the operator and the control loops reconfigured accordingly. Controllers for the new configuration would be automatically retuned using a multi-loop controller tuning algorithm and on-line process operation resumed.

4.2.4 Procedure Evaluation

4.2.4.1 Model System

In order to demonstrate how the procedure described in Section 4.2.2 can be used in a real process of identifying the most suitable CLC, a 3-output stirred mixing tank simulation was constructed in Simulink using a model consisting of three ordinary differential equations:

$$A_C \frac{dh}{dt} = F_H + F_C + F_B - K\sqrt{h}, \tag{4.16}$$

$$A_C \frac{d(hT)}{dt} = F_H T_H + F_C T_C + F_B T_B - K\sqrt{h}T, \tag{4.17}$$

and

$$A_C \frac{d(hC)}{dt} = F_H C_H + F_C C_C + F_B C_B - K\sqrt{h}C. \tag{4.18}$$

Here, A_C is the cross-sectional area of the tank and K is a constant related to the rate at which fluid leaves the orifice at the bottom of the tank. Each liquid flow is assumed to have equal and constant heat capacities and densities. In addition, expressions for the

steady-state brackish stream flowrate (F_{BS}), cold stream flowrate (F_{CS}), and hot stream flowrate (F_{HS}), which are required to initialize the simulation, are defined as:

$$F_{BS} = K\sqrt{h_S} \cdot \left[\frac{(C_H - C_S)(T_C - T_H) - (C_C - C_H)(T_H - T_S)}{(C_C - C_H)(T_B - T_H) - (C_B - C_H)(T_C - T_H)}\right], \tag{4.19}$$

$$F_{CS} = \frac{-F_{BS}(T_B - T_H) - K\sqrt{h_S}(T_H - T_S)}{(T_C - T_H)}, \tag{4.20}$$

and

$$F_{HS} = K\sqrt{h_S} - F_{BS} - F_{CS}. \tag{4.21}$$

Here, h_S is the tank's steady-state liquid level, T_S the steady-state liquid temperature, and C_S the steady-state salt concentration. Each model parameters units and values are listed in Table 4.1.

Table 4.1 Model parameters used in the stirred mixing tank simulation.

Description	Symbol	Value	Units
Cross-sectional area of the tank	A_C	2	m^2
Constant related to the rate at which fluid leaves the orifice at the bottom of the tank	K	0.25	$m^{5/2}/s$
Hot stream temperature	T_H	65	°C
Cold stream temperature	T_C	15	°C
Brackish stream temperature	T_B	15	°C
Hot stream salt concentration	C_H	0	kg/m^3
Cold stream salt concentration	C_C	0	kg/m^3
Brackish stream salt concentration	C_B	2	kg/m^3
Steady-state liquid level in the tank	h_S	2.5	m
Steady-state temperature in the tank	T_S	30	°C
Steady-state salt concentration in the tank	C_S	0.5	kg/m^3

4.2.4.2 Evaluation Design

The stirred mixing tank simulation was used to evaluate our procedure's ability to determine the most appropriate CLC of a non-linear process under changing operating conditions. We began our evaluation by simulating the stirred mixing tank using the parameter values provided in Table 4.1. At these operating conditions, the most appropriate CLC for the process (determined *a priori* as configuration 3 in Fig. 4.2) was implemented in conjunction with a set of PI controller tuning parameters (Table 4.2). Throughout our evaluation, the value of δ in Eq. 4.14 and 4.15 was set to 15 minutes, and the values of Θ_j and Θ_i recalculated each time new data became available. Following a simulation run of ~3.5 hours under initial operating conditions, we increased the stirred mixing tank desired liquid temperature from 30°C to 51°C, while the CLC and controller tuning remaining fixed. At this new operating condition, the stirred mixing tank model is nearly closed-loop unstable, but control system performance is not poor enough to warrant shutdown. Instead, the procedure execution criterion described in Section 4.2.3 is eventually fulfilled and on-line process data is collected for processing, while the desired liquid temperature is held at 51°C. Once 1000 data samples of each input and output were collected, our procedure was used to determine the most suitable CLC at the new desired liquid temperature. Subsequently, the newly recommended CLC was implemented and the PI controllers automatically retuned using the *looptune* function in Matlab. For an additional ~3.5 hours the simulation was continued using the new CLC and controller tuning in order to confirm expected control system performance improvement at the new desired liquid temperature.

Table 4.2 PI controller tuning parameters used for the initial CLC of the stirred mixing tank simulation.

Input—Output Pair	K_p	K_i
F_H—T	2.22×10^{-16}	5.76×10^{11}
F_C—h	5.39×10^{-3}	8.09×10^{-2}
F_B—C	2.22×10^{-16}	1.52×10^{13}

Because our procedure relies on using DSD, WGN having a mean of zero and variance of *b* was added to each input and output variable to gain informative process data and simulate measurement noise, respectively (Table 4.3). For input variables the values of *b* were selected to ensure sufficient but not significant process perturbation, thereby producing informative data with which to identify the most appropriate CLC. Values of *b* for output variables were chosen to imitate expected measurement noise of each output. Individual WGN signals had sampling intervals equal to the smallest process time constant (12.65 seconds).

Table 4.3 Noise variances for each WGN addition to the stirred mixing tank model's input and output variables.

Variable	Noise Variance (*b*)
F_H	2×10^{-5}
F_C	1.75×10^{-5}
F_B	9×10^{-6}
h	3.75×10^{-2}
T	0.4
C	1×10^{-3}

4.2.4.3 Evaluation Results

Fig. 4.3 – Fig. 4.6 show the results of simulating the stirred mixing tank. Based upon the evaluation design described in Section 4.2.4.2, our results demonstrate that before the desired liquid temperature is changed from 30°C to 51°C (specified by the

black dashed line in Fig. 4.3 – Fig. 4.6), variations in each input are due only to the additive WGN (Fig. 4.3), while each output tracked its respective setpoint reasonably well (Fig. 4.4). Consequently, the values of Θ_j and Θ_i remain close to their initial values of 1, indicating satisfactory control system performance under initial operating conditions (Fig. 4.5 and 4.6).

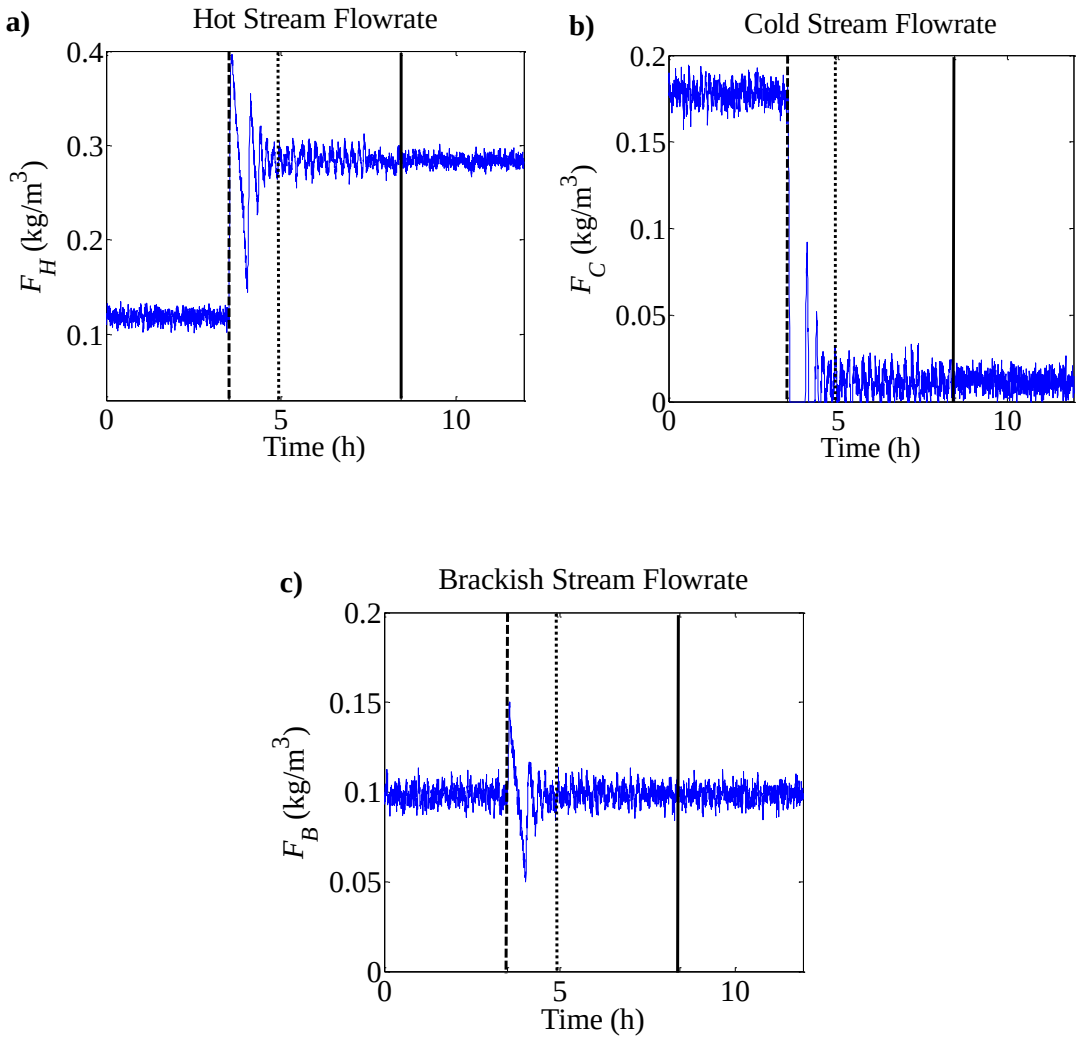

Figure 4.3 Time profiles of the stirred mixing tank inputs: **a)** hot stream flowrate; **b)** cold stream flowrate; and **c)** brackish stream flowrate. The blue lines represent collected data from the stirred mixing tank simulation. The black dashed line indicates the time when the operating temperature of the tank is increased to 51°C, the black dotted line indicates the time when an alarm is triggered due to poor output control system performance, and the black solid line is the time when control loops are reconfigured and controllers retuned.

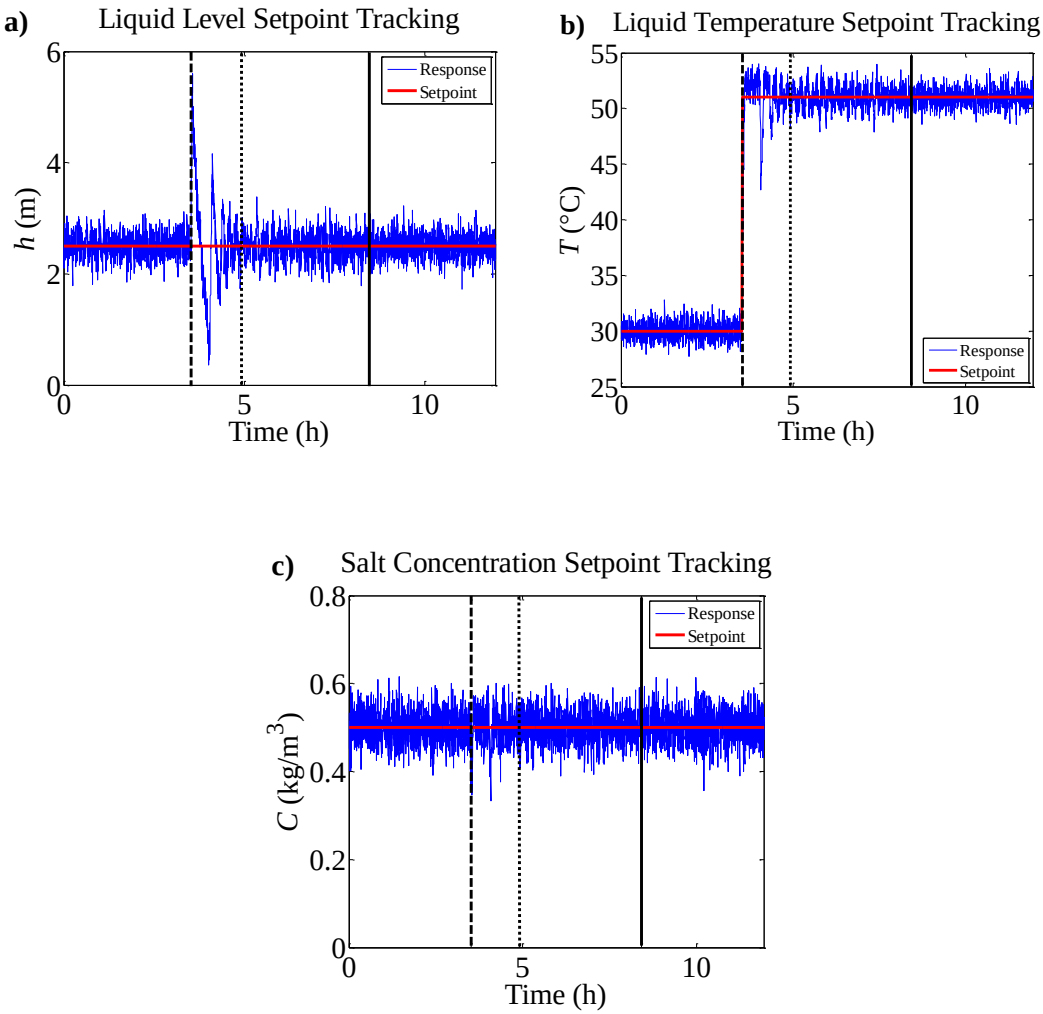

Figure 4.4 Stirred mixing tank output setpoint tracking: **a)** liquid level; **b)** liquid temperature; **c)** salt concentration. The blue lines represents data collected from the stirred mixing tank simulation while the red lines represent output setpoints. The black dashed line indicates the time when the operating temperature of the tank is increased to 51°C, the black dotted line indicates the time when an alarm is triggered due to poor output control system performance, and the black solid line is the time when control loops are reconfigured and controllers retuned.

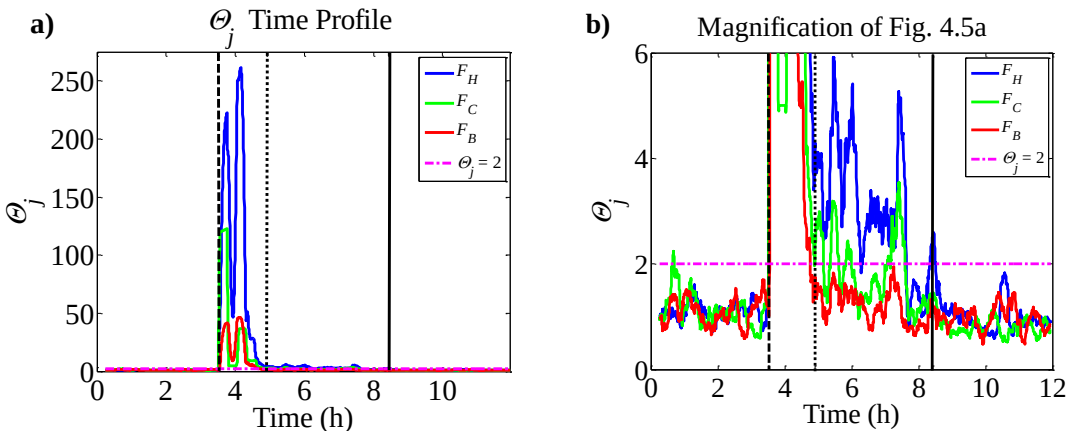

Figure 4.5 **a)** Time profiles of individual input control system performance metrics (Θ_j) during simulation of a stirred mixing tank; and **b)** a magnification of **a)**. The blue, green, and red lines represent Θ_{F_H}, Θ_{F_C}, and Θ_{F_B}, respectively while the dashed-dotted magenta line represents the threshold value of Θ_j = 2. The black dashed line indicates the time when the operating temperature of the tank is increased to 51°C, the black dotted line indicates the time when an alarm is triggered due to poor output control system performance, and the black solid line is the time when control loops are reconfigured and controllers retuned.

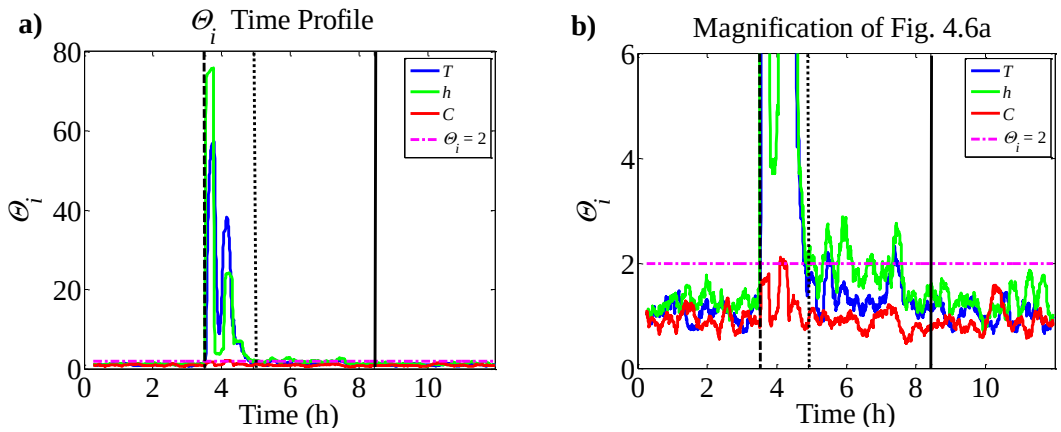

Figure 4.6 **a)** Time profiles of each output control system performance metric (Θ_i) during a simulation of the stirred mixing tank; and **b)** a magnification of **a)**. The blue, green, and red lines represent Θ_T, Θ_h, and Θ_C, respectively while the dashed-dotted magenta line represents the threshold value of Θ_i = 2. The black dashed line indicates the time when the operating temperature of the tank is increased to 51°C, the black dotted line indicates the time when an alarm is triggered due to poor output control system performance, and the black solid line is the time when control loops are reconfigured and controllers retuned.

Observe that after the desired liquid temperate is increased to 51°C at ~3.5 hours, input and output variables exhibit varying degrees of oscillatory behavior around/near their expected steady-state values (Fig. 4.3 and Fig. 4.4). As a result, the values of Θ_j and Θ_i all remain greater than 2 (with the exception of Θ_C) until ~4.8 hours (Fig. 4.5 and Fig. 4.6). At ~4.9 hours, the procedure execution criterion described in Section 4.3.3 is fulfilled when Θ_h increases above 2 after decreasing below the chosen threshold value of 2 following a change in desired operating temperature.

Upon fulfillment of the procedure execution criterion at ~4.9 hours, an alarm is triggered (specified by the dotted black line in Fig. 4.3 – Fig. 4.6) and the simulation continues unchanged until 1000 data samples for each input and output are collected.

During this time (between ~4.9 hours and ~8.4 hours) one can observe steady oscillations in F_H, F_C, h, and T near their expected steady-state values, while F_B and C settle into their expected steady-state values (Fig. 4.3 and Fig. 4.4). As a result, between ~4.9 hours and ~8.4 hours, Θ_{F_H}, Θ_{F_C}, Θ_h, and Θ_T are sometimes greater than 2 while Θ_{F_B} and Θ_C are never greater than 2 (Fig. 4.5 and Fig. 4.6), a result suggesting that at current operating conditions, input—output control loop pairings F_H—T and F_C—h do not minimize control loop interactions (and hence must be switched) while F_B—C remains a correct input—output pairing. As shown in Section 4.2.1, we can intuitively support this inference by determining that the most appropriate CLC of the stirred mixing tank changes from F_H—T, F_C—h, and F_B—C under initial operating conditions to F_C—T, F_H—h, and F_B—C after increasing the desired liquid temperature to 51°C.

Although the most suitable CLC at new operating conditions can be thus determined, our goal nonetheless is to evaluate our procedure for determining the most appropriate CLC of a process online using collected process data. Therefore, the 1000 input and output data samples collected between ~4.9 hours and ~8.4 hours were subsequently used in our procedure to identify the most apposite CLC of the stirred mixing tank simulation after the desired liquid temperature was increased to 51°C.

Fig. 4.7 shows the connection strength matrix obtained from Eq. 4.8 for the stirred mixing tank simulation at the new desired liquid temperature of 51°C. Two characteristics of the connection strength matrix are worth noting. First, all diagonal elements of the connection strength matrix are statistically significant and much greater than any off-diagonal value, suggesting that each process variable is highly correlated with itself (which must be true). Second, all of the statistically significant

off-diagonal elements of the connection strength matrix can be explained using knowledge of the known direct and indirect connections between process variables of the simulated closed-loop stirred mixing tank under the initial CLC (Fig. 4.8). More specifically, each input as a connection source has a direct connection to each output as a connection sink, and each output as a connection source has direct connectivity with each input as a connection sink that was used to control the respective output given the initial CLC. Also, as a consequence of closed-loop feedback control, each input as a connection source can have an indirect connection to other inputs being connection sinks. Likewise, each output as a connection source can have an indirect connection to other outputs being connection sinks.

	F_H	F_C	F_B	h	T	C
F_H	550	7	29	5*	33	12
F_C	3*	542	3*	35	5*	2*
F_B	4*	7	615	5*	3*	171*
h	20	17	20	505	5*	11
T	18	87	81	10	510	36
C	10	7	71	6	8	534

Figure 4.7 Connection strengths estimated using data collected from the stirred mixing tank simulation between ~4.9 hours and ~8.4 hours. Each column variable corresponds to a connection source; each row variable corresponds to a connection sink. An asterisk (*) denotes a statistically insignificant connection-strength estimate (i.e., below the 99% statistical significance threshold).

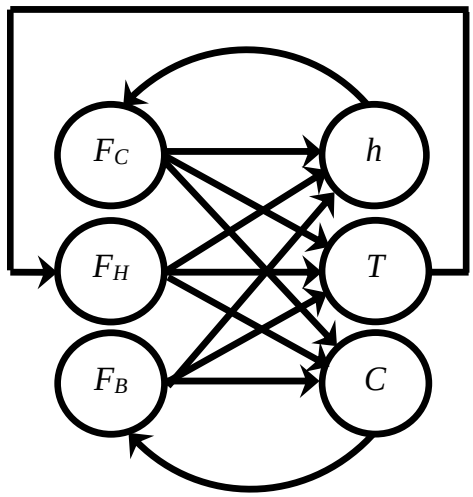

Figure 4.8 Schematic of the known connections between process variables in the closed-loop stirred mixing tank using controller configuration 3 from Fig. 4.2.

The connection strength estimates were validated using the procedure described in Appendix A. The resulting Pearson correlation coefficient matrix of the white noise sequences and the corresponding matrix of t scores are shown in Fig. 4.9 and Fig. 4.10, respectively. All off-diagonal elements of Fig. 4.10 are infinite because each white noise sequence is perfectly correlated with itself (i.e., the diagonal elements of Fig. 4.9 are all 1). Because all off-diagonal elements are less than 1.9623, there is no evidence to reject H_0 at the 95% confidence level, and white-noise sequences are insignificantly correlated. Thus, our connection strength estimates (Fig. 4.7) are deemed valid.

	F_H	F_C	F_B	h	T	C
F_H	1.000	0.031	0.032	-0.006	0.000	0.011
F_C	0.031	1.000	0.036	0.000	-0.011	-0.032
F_B	0.032	0.036	1.000	-0.008	0.002	-0.001
h	-0.006	0.000	-0.008	1.000	0.019	-0.024
T	0.000	-0.011	0.002	0.019	1.000	0.014
C	0.011	-0.032	-0.001	-0.024	0.014	1.000

Figure 4.9 Estimated Pearson correlation coefficient matrix of white noise sequences from the SVAR model using data collected from the stirred mixing tank simulation between ~4.9 hours and ~8.4 hours.

	F_H	F_C	F_B	h	T	C
F_H	∞	0.978	1.006	0.180	0.002	0.354
F_C	0.978	∞	1.145	0.002	0.341	0.999
F_B	1.006	1.145	∞	0.244	0.054	0.040
h	0.180	0.002	0.244	∞	0.590	0.771
T	0.002	0.341	0.054	0.590	∞	0.432
C	0.354	0.999	0.040	0.771	0.432	∞

Figure 4.10 Estimated Pearson correlation coefficient t scores of white noise sequences from the SVAR model using data collected from the stirred mixing tank simulation between ~4.9 hours and ~8.4 hours.

Upon validating the connection strength estimates, Eq. 4.12 and Eq. 4.13 were used to determine the interaction factor, Γ_i, for each output (Table 4.4). As expected, $\Gamma_C > \Gamma_T > \Gamma_h$ because only F_B has a high connection strength with C, F_C and F_B have similarly high connection strengths with T, and all three inputs have nearly equal connection strengths with h. After ranking the values of Γ_i from highest to lowest, the input-output pairing procedure described in Section 4.2.2.3 was used to determine the most suitable CLC of the stirred mixing tank at current operating conditions. Our

input-output pairing procedure dictates that F_B is first paired with C, then F_B with T, and lastly F_H with h. Therefore, our entire procedure as described in Section 4.2.2 correctly determined that controller configuration 1 (Fig. 4.2) minimizes control loop interactions for the simulated stirred mixing tank when the desired liquid temperature is increased to 51°C.

Table 4.4 Output interaction factors determined using data collected between ~4.9 and ~8.4 hours of a stirred mixing tank simulation.

Output Variable	Interaction Factor (Γ_i)
h	0.0805
T	0.4245
C	0.8801

After determining the most apposite CLC for the simulated stirred mixing tank at the new desired liquid temperature of 51°C, the control loops were reconfigured accordingly, the controllers were retuned using the *looptune* function in Matlab (Table 4.5), and the simulation was continued. Following control loop reconfiguration and controller retuning (the time of this action is indicated by the solid black line in Fig. 4.3 – Fig. 4.6), the variation in F_H, F_C, h, and T around near their expected steady-state values was reduced to an amount similar to that observed under initial operating conditions and CLC (Fig. 4.3 and Fig. 4.4). As a result, the values of Θ_{F_H}, Θ_{F_C}, Θ_h, and Θ_T remain below 2, indicating satisfactory control system performance under these new operating conditions (Fig. 4.5 and Fig. 4.6).

Table 4.5 PI controller tuning parameters for the new CLC of the stirred mixing tank simulation.

Input—Output Pair	K_p	K_i
F_C—T	2.22×10^{-16}	-2.95×10^{11}
F_H—h	2.22×10^{-16}	1.17×10^{12}
F_B—C	1.70×10^{-2}	2.04×10^{-1}

4.3 Data-driven Centralized Control: Adaptive Model Predictive Control of a PV/WT/FC/battery/electrolyzer HRES for Residential Applications

4.3.1 Overview

For some HRESs, the challenges associated with their control (stochastic nature of natural resources and inherent non-linearity and physical constraints of HRES components) have been overcome, in part, by using model predictive control (MPC) to coordinate the flow of power to and from HRES components such that power demands are satisfied and storage capacity setpoints are maintained. MPC is advantageous for HRESs having many components because of its straight-forward constraint handling capabilities (of which there can be many in a HRES) and its optimal reduction of predicted feedback error using predicted future process states.

Previously, MPC has been used to meet the operating objectives of a WT/diesel generator hybrid energy system [26] and a PV/WT/FC/electrolyzer/battery HRES [27]. Although the operating objectives of these hybrid energy systems were met reasonably well using MPC, we hypothesize that control performance can be improved using information-rich data available nearly continuously from a HRES (e.g., wind speed, solar irradiance, component power outputs, etc.). We propose that the data collected from a HRES can be used to improve MPC performance via measured disturbance prediction and model adaptation.

Measured disturbances are process variables that affect controlled variables but are dependent on inputs that cannot be manipulated. In a HRES, PV and WT power are examples of measured disturbances because they affect the control of total HRES power output and energy storage levels, but solar irradiance and wind speed cannot be manipulated. By obtaining accurate predictions of PV and WT power, a model predictive controller can compute control action that accounts for future values of measured disturbances and, as a result, control performance of the HRES can be improved.

Model adaptation, in this context, is the practice of approximating linear models (required in the MPC strategy) of a non-linear, time-variant process as the process undergoes changes in operating conditions. Some components of HRESs are non-linear, time-variant systems. For example, it is well known that FC power is a non-linear function of fuel flowrate [77], and this process relationship can be significantly altered by catalyst degradation over time [78]. Therefore, updating the linear model approximation of each HRES component to match current operating conditions and system characteristics can result in more accurate representation of the HRES in the MPC framework, which can ameliorate control performance.

In this Section of the dissertation, we are concerned with the development and evaluation of a data-driven MPC strategy for an off-grid PV/WT/FC/battery/electrolyzer HRES. The data-driven MPC strategy contains a traditional MPC algorithm supported by measured disturbance prediction and model adaptation. Measured disturbance prediction was executed using adaptive ARIMA time-series modeling while model adaptation was accomplished using subspace identification. The benefits of using the data-driven MPC strategy are demonstrated by

way of a 24-hour simulation study of a HRES responsible for meeting the power demand of a typical single-family home during the summer in Newark, DE.

4.3.2 Process Description

The HRES design (shown schematically in Fig. 4.11) consists of five primary components: a PV array, a WT array, a FC, a string of batteries, and an electrolyzer. The 9 kW-rated PV array, consisting of thirty LG300N1C-G3 monocrystalline silicon modules, along with three, 2.5 kW-rated WES5 Tulipo variable-speed WTs[10] produce a combined uncontrollable power (P_{uncon}) that is first used to meet the home's power demand (P_{demand}). If $P_{uncon} < P_{demand}$, the sum of controllable power from a 3 kW proton exchange membrane (PEM) FC and a string of three Hoppecke 24 OPsZ 3000 deep-cycle lead-acid batteries (P_{con}) is used to meet the home's remaining power demand. However, if $P_{uncon} > P_{demand}$, the excess power (P_{excess}) is either used to charge the battery string (P_{batt}^{ch}) or sent to a 3 kW PEM electrolyzer (P_{elec}) to produce hydrogen.

[10] The WT rated power output is the power output of the WT at a wind speed of 9 m/s.

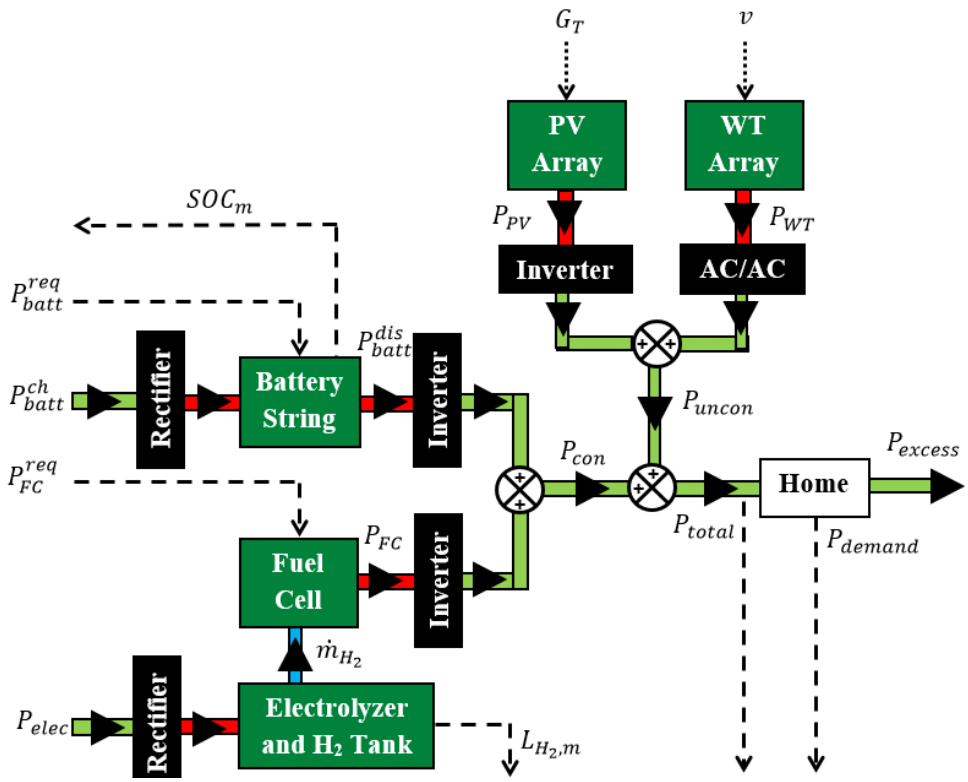

Figure 4.11 A schematic of the PV/WT/FC/battery/electrolyzer HRES for a residential application. Block color representation: green, primary components; black, power conditioning units; white, electrical power end use. Solid stream color representation: light green, AC power; red, DC power; hydrogen; blue. Black solid arrows indicate the directional flow of streams. Black dotted lines represent disturbance inputs to the HRES while black dashed lines represent flow of information to or from a controller.

The PV array and the WT efficiencies are maximized using maximum power point tracking (MPPT)—a technique used to extract the maximum usable power from a system at current operating conditions. The PV array uses a Short-Current Pulse MPPT method, which determines the operating current of the PV array needed to achieve maximum power output [30]. The operating current is realized by using a current-controlled DC/DC power converter. The WT MPPT is accomplished by

controlling the rotor speed to a value corresponding to maximum power output at a given wind speed and blade pitch angle. The rotor speed is regulated using a set of PI controllers that manipulate the WT generator current and voltage in the dq-synchronous rotating reference frame as described in [79]. The blade pitch angle is determined using a power controller that reduces power output of the WT at wind speeds higher than its rated wind speed (9 m/s), thereby maintaining safe operation of the WT.

The PEMFC is maintained by four auxiliary components: twin high-pressure hydrogen storage tanks, an air compressor, a water-cooled heat exchanger, and a membrane humidifier. The high-pressure hydrogen storage tanks, each rated at 350 bar, can store up to 5.6 kg of hydrogen [80]. The stored hydrogen is released to the anode of the PEMFC system using a pressure regulator valve, while oxygen is delivered to the cathode of the PEMFC system using an air compressor. The air compressor delivers enough oxygen to the cathode to maintain the molar ratio of oxygen to hydrogen added to the fuel cell (commonly referred to as the excess oxygen ratio) at 2. The PEMFC temperature is maintained at 75°C using a water-cooled heat exchanger while a membrane humidifier maintains relative humidity of the compressed air at 100% using moisture from the cathode exhaust air.

Although the PEM electrolyzer is essentially a reverse PEMFC, the electrolyzer only requires temperature regulation. The electrolyzer temperature is maintained at 40°C using a water-cooled heat exchanger similar to that used by the FC.

Safety and reliability of the HRES's electrical system is preserved using power conditioning units that match the voltage and current type of electrical power sources

and sinks. Power conditioning is achieved using three inverters, two rectifiers, and an AC/AC converter. Each inverter increases the low voltage direct current (DC) power (~30 V for the PV array, ~30V for the FC, ~2V for the battery) to match the high voltage alternating current (AC) power of the electricity mains of the home (~120V at 60 Hz is standard for homes in the United States). Each rectifier is used to condition AC power from the main AC bus to match the DC voltage of the power sink (~2V for the battery when it is being charged and ~20V for the electrolyzer). The AC/AC converter takes AC power produced from the WTs (~400V at 60 Hz) and matches the AC power of the electricity mains of the home.

4.3.3 Process Modeling and Simulation

A modular approach was used to model and simulate the PV/WT/FC/battery/electrolyzer HRES in Simulink. Each component model was constructed separately using models provided in the literature. The PV model is identical to the one described in Section 3.2.3.1 except the number of PV modules (n_m) is set equal to 30. The WT, FC, battery, electrolyzer, and hydrogen storage models are described in the remainder of this Section.

4.3.3.1 Wind Turbine Model

The WT model, shown schematically in Fig. 4.12, was used to determine the combined electrical power generated by the WTs (P_{WT}) given v, T_a, and atmospheric pressure (P_{atm}). The WT model consists of an aerodynamic model, a drive train model, and a generator model supported by different control schemes depending on v (Fig. 4.13). If v is less than the cut-in wind speed (v_{cut-in}), the generator is stalled and no power is produced (zone I in Fig. 4.13). If v_{cut-in} < v < the rated wind speed

(v_{rated}), a generator speed control scheme is used for MPPT (zone II in Fig. 4.13). If v_{rated} < v < the cut-out wind speed ($v_{cut-out}$), a pitch angle control scheme is used to reduce rotor speed and power output to safe levels (zone III in Fig. 4.13). If $v_{cut-out}$ < v, the blade pitch angle is set to 90°, the rotor stops rotating, and no power is generated (zone IV in Fig. 4.13).

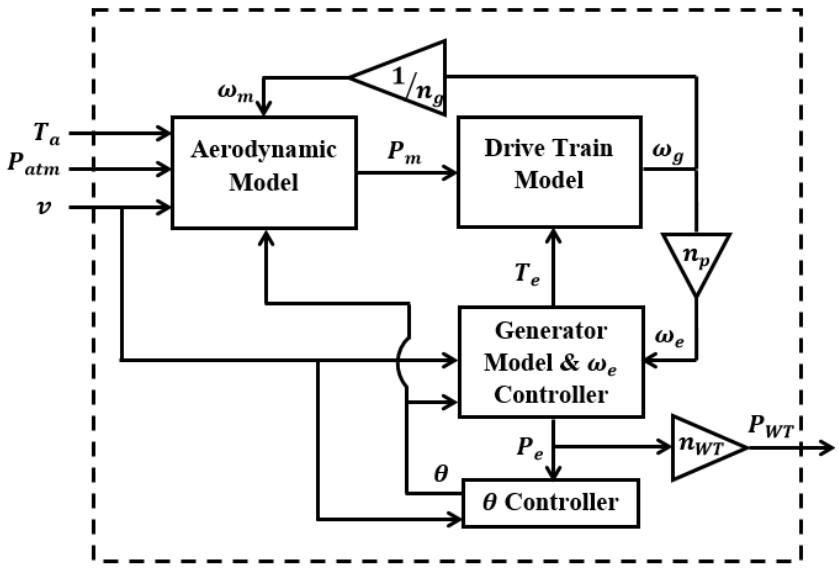

Figure 4.12 Schematic of the wind turbine model.

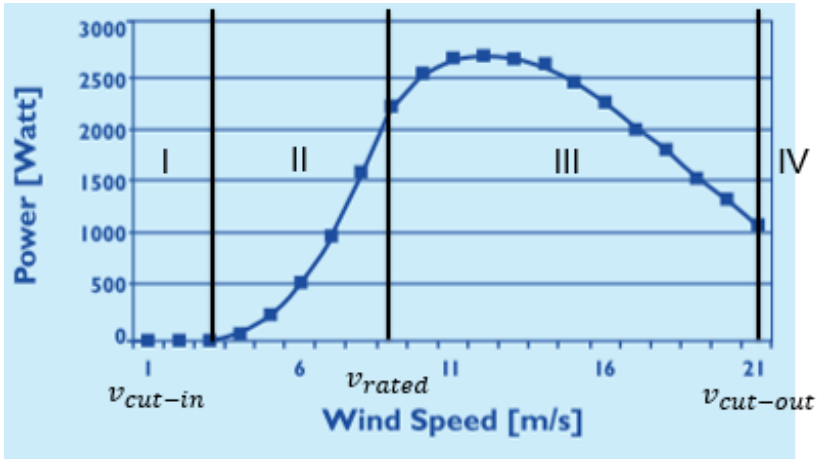

Figure 4.13 WES5 Tulipo steady-state power output as a function of wind speed. WT control varies depending on the current operation zone (I, II, III, or IV). Figure source: http://www.cellenergy.ie/pdf/WES5_Tulipo_brochure_ds1.pdf

The aerodynamic model determines the simulated mechanical power (P_m) of the WT given v and T_a as follows:

$$P_m = 0.5\rho_{air}\pi R^2 v^3 C_p, \tag{4.22}$$

$$\rho_{air} = \frac{P_{atm}}{R_{air}T_a}. \tag{4.23}$$

Here, ρ_{air} is the air density, R_{air} is the specific gas constant for dry air, R is the radius of the WT rotor, and C_p is the WT power coefficient expressed as [81]:

$$C_p = 0.22\left(\frac{116}{\beta} - 0.4\theta - 5\right)\exp\left(\frac{-12.5}{\beta}\right). \tag{4.24}$$

In Eq. 4.24, θ is the pitch angle of the rotor blades and β is [82]:

$$\beta = \left(\frac{1}{\lambda + 0.08\theta} - \frac{0.035}{\theta^3 + 1}\right)^{-1}, \tag{4.25}$$

where λ is the tip-speed ratio of the WT (i.e., the ratio of angular rotor speed to wind speed), which is represented mathematically as:

$$\lambda = \frac{\omega_m R}{v}, \tag{4.26}$$

where ω_m is the turbine rotor rotational speed.

The drive train model, shown schematically in Fig. 4.14, was used to simulate the generator rotational speed (ω_g) given the generator electromagnetic torque (T_e), the aerodynamic torque transferred to the generator (T_{m_g}), the rotational damping coefficient (B_m), and the rotor/generator equivalent inertia (J_{eq}) as follows:

$$\frac{d\omega_g}{dt} = \frac{T_e - T_{m\_g} - B_m \omega_g}{J_{eq}}. \tag{4.27}$$

The aerodynamic torque transferred to the generator is given by:

$$T_{m\_g} = \frac{P_m}{\omega_m n_g}, \tag{4.28}$$

where n_g is the gear ratio between the rotor and generator, and

$$J_{eq} = \frac{J_m + J_g}{n_g^2}. \tag{4.29}$$

In Eq. 4.29, J_m is the rotor inertia and J_g is the generator inertia.

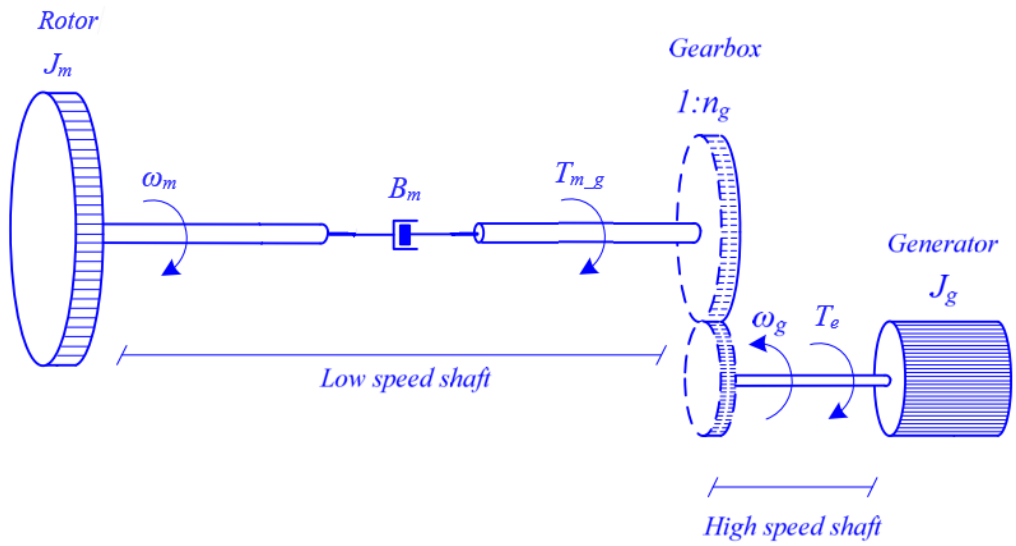

Figure 4.14 Schematic of the WT drive train. The rotor rotates the low speed shaft at an angular speed of ω_m, having an inertia (J_m), and a rotational damping coefficient of B_m. The torque transferred from the rotor side to the generator side (T_{m_g}), delivered from a gear box ratio (n_g), rotates the high speed shaft at an angular speed of ω_g. The generator has an inertia of J_g and generates electromagnetic torque (T_e) in the opposite rotational direction of ω_g [83].

The WT generator is a permanent magnet synchronous generator (PMSG) that generates three-phase (a, b, and c) power. The PMSG was modeled in the *dq*-synchronous reference frame (see Fig. 4.15), which yields a simplified PMSG model as follows [84]:

$$\frac{di_d}{dt} = \frac{-R_a}{L} i_d + \omega_e i_q + \frac{u_d}{L}, \tag{4.30}$$

$$\frac{di_q}{dt} = \frac{-R_a}{L} i_q - \omega_e \left(i_q + \frac{\psi_{pm}}{L} \right) + \frac{u_q}{L}, \tag{4.31}$$

where i_d and u_d are the *d*-axis current and voltage, respectively, i_q and u_q are the *q*-axis current and voltage, respectively, R_a is the armature resistance, L is the generator

inductance, ψ_{pm} is the permanent magnetic flux, and ω_e is the electrical rotating speed given by $\omega_e = n_p \omega_g$ where n_p is the number of magnetic pole pairs.

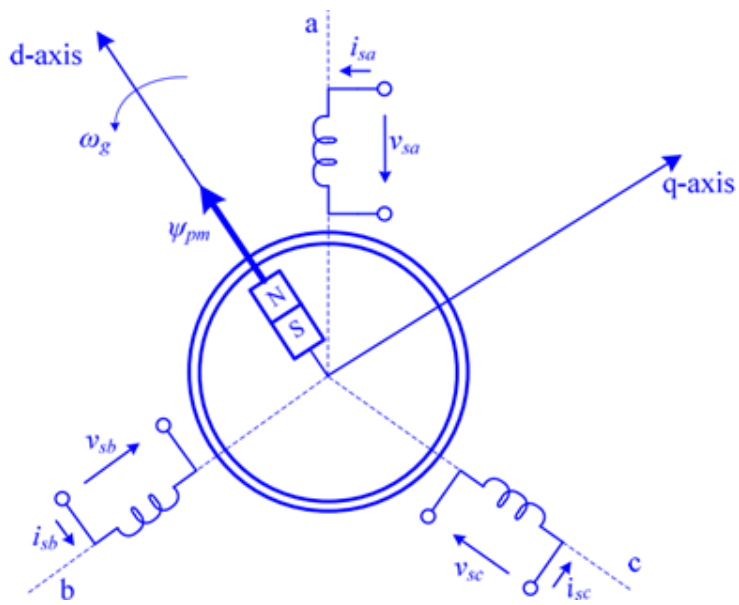

Figure 4.15 PMSG schematic showing the static three-phase *abc* reference frame and the rotating *dq*-synchronous reference frame as if looking straight down the center of the high speed shaft. The permanent magnet pole pair (N/S), having a permanent magnetic flux of ψ_{pm}, rotates counter-clockwise at an angular speed equal to the generator speed (ω_g). The magnet passes near one of three inductance coils every 120° of rotation, generating current and voltage in either the *a*, *b*, or *c* phase. The *d*-axis and *q*-axis remain perpendicular to each other while rotating in sync with the permanent magnet pole pair [83].

The electromagnetic torque is then obtained from

$$T_e = 1.5 n_p i_q \psi_{pm}, \tag{4.32}$$

While the electrical power from a single WT (P_e) is

$$P_e = T_e \omega_e. \tag{4.33}$$

The combined WT power output (P_{WT}) is then expressed as:

$$P_{WT} = P_e n_{WT}, \tag{4.34}$$

where n_{WT} is the number of wind turbines.

The generator speed control strategy (control strategy used when operating in zone II in Fig. 4.13) is needed to extract as much power from the wind as possible. As described in Section 1.3.2, WT MPPT matches ω_m to a reference value ($\omega_{m,ref}$) that maximizes C_p for a given v and θ (see Eq 4.24 – 4.26). To match ω_m to $\omega_{m,ref}$, the cascade control strategy shown in Fig. 4.16 was implemented [84]. First, $\omega_{m,ref}$ is obtained for a given v using a lookup table and then converted to $\omega_{e,ref}$ using n_g and n_p. Then, ω_e is matched to $\omega_{e,ref}$ using a PI controller (PI1) to manipulate $i_{q,ref}$, which is controlled using another PI controller (PI2) that manipulates u_q. Concurrently, i_d is controlled to $i_{d,ref}$ using a PI controller (PI3) that manipulating u_d. The controller parameters are provided in Table 4.6.

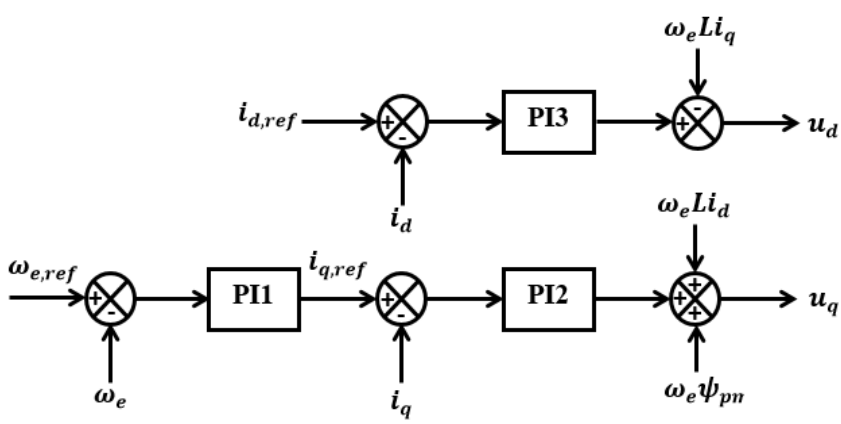

Figure 4.16 Schematic of the generator speed cascade control strategy [84].

The blade pitch control strategy (control strategy used when operating in zone III in Fig. 4.13). is needed to maintain safe operation of the WT when $v > v_{rated}$. As shown in Fig. 4.17, the blade pitch control strategy actuates θ such that P_e is controlled to a reference value of P_e ($P_{e,ref}$). The control of P_e to $P_{e,ref}$ is executed using a combination of a feedback PI controller (PI4) and a feedforward P-only controller (FF). The PI4 and FF controller parameters are provided in Table 4.6 while all remaining WT model parameters are given in Table 4.7.

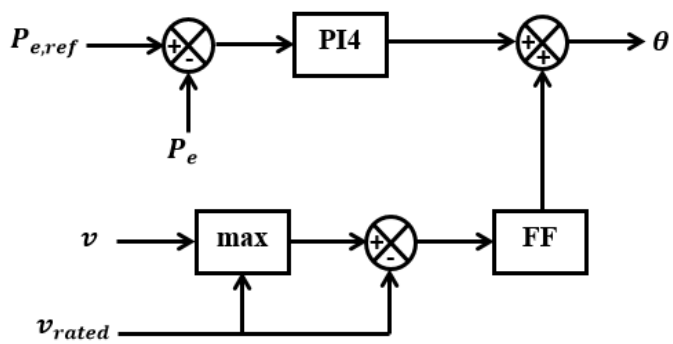

Figure 4.17 Schematic of the blade pitch control scheme [84].

Table 4.6 Controller parameters for the generator speed and blade pitch control strategies.

Controller	K_p	K_i
PI1	3.69×10^{-2}	2.24×10^{-2}
PI2	6.11	3.99×10^{3}
PI3	6.11	3.99×10^{3}
PI4	-1.27×10^{-2}	-2.15×10^{-2}
FF	10	N/A

Table 4.7 Wind turbine model parameters

Description	Parameter	Value	Units
Rotor radius[11]	R	2.5	m
Specific gas constant for dry air	R_{air}	287.05	$J \cdot kg^{-1} \cdot K^{-1}$
Rotational damping coefficient [84]	B_m	0	$kg \cdot m^2 \cdot rad^{-1} \cdot s^{-1}$
Rotor inertia[12]	J_m	23.4047	$kg \cdot m^2$
Generator inertia[12]	J_g	0.00067	$kg \cdot m^2$
Gear ratio[12]	n_g	6	N/A
Armature Resistance [85]	R_a	12.9	Ω
Generator inductance [85]	L	6.7×10^{-2}	H
Permanent magnetic flux [86]	ψ_{pm}	0.835	Wb
Number of pole pairs [85]	n_p	8	N/A
Number of wind turbines	n_{WT}	3	N/A
Cut-in wind speed[11]	v_{cut-in}	3	m/s
Rated wind speed[11]	v_{cut-in}	9	m/s
Cut-out wind speed[11]	$v_{cut-out}$	21	m/s

[11] Provided in the WES5 Tulipo technical brochure (http://www.cellenergy.ie/pdf/WES5_Tulipo_brochure_ds1.pdf).

[12] Estimated using the known rotor radius and the methods described in [103].

4.3.3.2 Fuel Cell Model

In this Section, a more detailed PEMFC model is used than that described in Section 3.2.3.2. The detailed FC model, provided in [24], consists of separate dynamic polarization, gas partial pressure, and thermal models supported by FC temperature (T_{FC}), power (P_{FC}), and excess oxygen ratio (λ_{O_2}) control (Fig. 4.18).

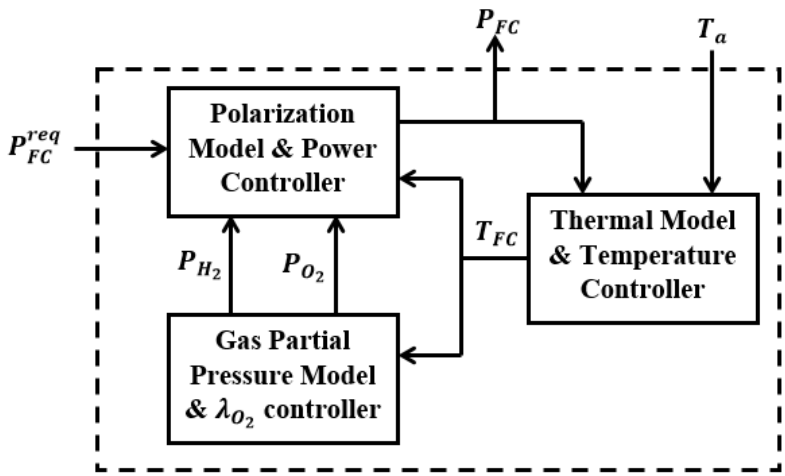

Figure 4.18 Schematic of the FC model

The dynamic polarization curve model determines V_{FC} as a function of thermodynamic potential (E), activation voltage losses (V_{act}), ohmic voltage losses (V_{ohm}), and mass transport voltage losses (V_{mass}) as follows:

$$V_{FC} = n_{cell,FC}(E - V_{act} - V_{ohm} - V_{mass}), \tag{4.35}$$

where n_{cell} is the number of cells connected in series in the FC stack. In Eq. 4.35, V_{mass} was considered negligible, while E, V_{act}, and V_{ohm} are given empirically by [87]:

$$\begin{cases} E = 1.229 - 8.5x10^{-4}(T_{FC} - 298.15) + \frac{R_{gas}T_{FC}}{2F}\ln\left[P_{H_2}P_{O_2}^{0.5}\right] \\ \frac{dV_{act}}{dt} = I_{FC}\left(\frac{1}{C_{dl}} + \frac{V_{act}}{E_{act}C_{dl}}\right) \\ V_{ohm} = \frac{181\left[1 + 0.03\left(\frac{I_{FC}}{A_{FC}}\right) + 0.062\left(\frac{T_{FC}}{303}\right)^2\left(\frac{I_{FC}}{A_{FC}}\right)^2\right]}{A_{FC}\left[11.866 - 3\left(\frac{I_{FC}}{A_{FC}}\right)\right]\exp\left[4.18\left(\frac{T_{FC} - 303}{T_{FC}}\right)\right]} \end{cases}, \tag{4.36}$$

where T_{FC} is the FC temperature, R_{gas} is the universal gas constant, F is Faraday's constant, P_{H_2} is the partial pressure of hydrogen in the anode, P_{O_2} is the partial pressure of hydrogen in the cathode, I_{FC} is the FC current, C_{dl} is the double layer capacitance, E_{act} is the activation energy of the cathode half-reaction, and A_{FC} is the FC catalyst active area. The empirical formula for E_{act} is

$$E_{act} = \xi_1 + \xi_2 T_{FC} + \xi_3 T_{FC}\ln\left(C_{O_2}\right) + \xi_4 T_{FC}\ln(I_{FC}) \tag{4.37}$$

with parameters:

$$\begin{cases} \xi_1 = -0.948 \\ \xi_2 = 2.86x10^{-3} + 2x10^{-4}\ln(A_{FC}) + 4.3x10^{-5}\ln\left(C_{H_2}\right) \\ \xi_3 = 7.6x10^{-5} \\ \xi_4 = -1.93x10^{-4} \end{cases}, \tag{4.38}$$

where the oxygen concentration at the cathode/membrane interface (C_{O_2}), and the hydrogen concentration at the anode/membrane interface (C_{H_2}) can be obtained using Henry's law. The Henry's law expressions for C_{O_2} and C_{H_2} are [88]:

$$C_{O_2} = 1.97x10^{-7}P_{O_2}\exp\left(\frac{498}{T_{FC}}\right), \tag{4.39}$$

and

$$C_{H_2} = 9.174x10^{-7}P_{H_2}\exp\left(\frac{-77}{T_{FC}}\right). \tag{4.40}$$

The dynamic gas partial pressure model is used to determine P_{H_2} and P_{O_2} for the polarization model as follows:

$$\begin{cases} \dfrac{V_{an}}{R_{gas}T_{FC}}\dfrac{dP_{H_2}}{dt} = \dot{m}_{H_2,in} - \dot{m}_{H_2,out} - \dfrac{n_{cell}I_{FC}}{n_{H_2}F} \\ \dfrac{V_{cat}}{R_{gas}T_{FC}}\dfrac{dP_{O_2}}{dt} = \dot{m}_{O_2,in} - \dot{m}_{O_2,out} - \dfrac{n_{cell}I_{FC}}{n_{O_2}F} \end{cases}, \tag{4.41}$$

where V_{an} and V_{cat} are the volume of the anode and cathode gas channels, respectively, n_{H_2} and n_{O_2} are the number of electrons produced per mole of hydrogen and oxygen reacted, respectively, and $\dot{m}_{H_2,out}$ and $\dot{m}_{O_2,out}$ are assumed to be

$$\begin{cases} \dot{m}_{H_2,out} = k_{an}\left(P_{H_2} - P_{H_2,in}\right) \\ \dot{m}_{O_2,out} = k_{cat}\left(P_{O_2} - P_{O_2,out}\right) \end{cases}. \tag{4.42}$$

In Eq. 4.42, k_{an} and k_{cat} are the anode and cathode flowrate constants, respectively, $P_{H_2,in}$ is the hydrogen partial pressure at the anode inlet, and $P_{O_2,out}$ is the oxygen partial pressure at the cathode outlet. Furthermore, λ_{O_2} is defined as

$$\lambda_{O_2} = \frac{\dot{m}_{O_2,in}n_{O_2}F}{n_{cell}I_{FC}}. \tag{4.43}$$

The dynamic FC thermal model, derived from a heat balance of the FC, is expressed as:

$$\begin{cases} C_{t,FC}\dfrac{dT_{FC}}{dt} = \dot{E}_{tot} - P_{FC} - \dot{Q}_{loss} - \dot{Q}_{cool} \\ \dot{E}_{tot} = \dfrac{\Delta H_{FC}n_{cell}I_{FC}}{n_{H_2}F} \\ P_{FC} = V_{FC}I_{FC} \\ \dot{Q}_{loss} = \dfrac{C_{t,FC}(T_{FC} - T_a)}{\tau_{t,FC}} \\ \dot{Q}_{cool} = \left(h_{cond,FC} + h_{conv,FC}I_{FC}\right)\dfrac{\left(T_{FC} - T_{c,in}\right) - \left(T_{FC} - T_{c,out}\right)}{\ln\left[\left(T_{FC} - T_{c,in}\right)/\left(T_{FC} - T_{c,out}\right)\right]} \end{cases}, \tag{4.44}$$

where $C_{t,FC}$ is the FC thermal capacitance, $\dot{E}_{tot}$ is the total chemical power delivered

to the FC, P_{FC} is the electrical power generated by the FC, $\dot{Q}_{loss}$ is the rate of heat loss to the environment, $\dot{Q}_{cool}$ is the rate of heat loss to the water-cooled heat exchanger, ΔH_{FC} is the enthalpy of hydrogen consumption in a PEM FC, $\tau_{t,FC}$ is a FC thermal time constant, h_{cond} and h_{conv} are the conductive and convective FC heat exchanger coefficients, respectively, $T_{c,in}$ is the cooling water temperature into the FC, and $T_{c,out}$ is the cooling water temperature leaving the FC. The cooling water temperature leaving the FC is obtained from a separate energy balance as follows:

$$\rho_w V_w C_{pw} \frac{dT_{c,out}}{dt} = \dot{m}_{cw} C_{pw} \left(T_{c,in} - T_{c,out}\right) + UA \left(T_{FC} - \frac{T_{c,in} - T_{c,out}}{2}\right), \quad (4.45)$$

where ρ_w is the water density, V_w is the water volume, C_{pw} is the heat capacity of water, $\dot{m}_{cw}$ is the cooling water flowrate, and UA is the overall heat transfer index.

In the FC control scheme, $\dot{m}_{cw}$, $\dot{m}_{H_2,in}$, and $\dot{m}_{O_2,in}$ are used to control T_{FC}, P_{FC}, and λ_{O_2}, respectively. As shown in Fig. 4.19, a set of PI controllers are used to regulate T_{FC}, P_{FC}, and λ_{O_2} to their desired values ($T_{FC,d}$, P_{FC}^{req}, and $\lambda_{O_2,d}$). The PI controller parameters are provided in Table 4.8 and all other FC model parameters are given in Table 4.9.

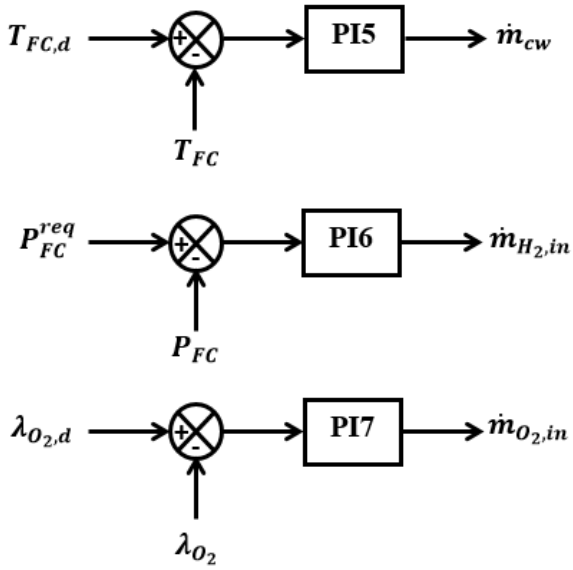

Figure 4.19 Schematic of the FC temperature, power, and excess oxygen ratio control scheme.

Table 4.8 FC PI controller parameters.

Controller	K_p	K_i
PI5	-1.70×10^{-3}	-3.87×10^{-5}
PI6	1.83×10^{-6}	1.04×10^{-6}
PI7	1.19×10^{-2}	2.02

Table 4.9 FC model parameters provided in [24] unless otherwise noted.

Description	Parameter	Value	Units
Number of FC cells connected in series[13]	$n_{cell,FC}$	21	N/A
Universal gas constant	R_{gas}	8.206×10^{-5}	$m^3 \cdot atm \cdot K^{-1} \cdot mol^{-1}$
Double layer capacitance	C_{dl}	8.12	F

[13] Since we are using a 3 kW FC system in this work, these parameter values were assumed to be 60% of the values for a 5 kW FC system provided in [24].

FC catalyst active area per cell	A_{FC}	2.32x10^{-2}	m^2
Anode volume	V_{an}	5x10^{-3}	m^3
Cathode volume	V_{cat}	1x10^{-2}	m^3
Number of electrons produced per mole of hydrogen reacted	n_{H_2}	2	N/A
Number of electrons produced per mole of oxygen reacted	n_{O_2}	4	N/A
Anode flowrate constant	k_{an}	6.5x10^{-2}	mol·s^{-1}·atm^{-1}
Cathode flowrate constant	k_{cat}	6.5x10^{-2}	mol·s^{-1}·atm^{-1}
Hydrogen partial pressure at the anode inlet	$P_{H_2,in}$	3	atm
Oxygen partial pressure at the cathode outlet	$P_{O_2,out}$	1	atm
FC thermal capacitance[13]	$C_{t,FC}$	1.074x10^4	J·K^{-1}
Enthalpy of hydrogen consumption in a PEM FC	ΔH_{FC}	2.855x10^5	J·mol^{-1}
FC thermal time constant[13]	$\tau_{t,FC}$	1.236	s
Conductive FC heat exchanger coefficient	$h_{cond,FC}$	35.55	W·K^{-1}
Convective FC heat exchanger coefficient	$h_{conv,FC}$	2.5x10^{-2}	W·K^{-1}·A^{-1}
Inlet cooling water temperature	$T_{c,in}$	298	K
Water density	ρ_w	1000	kg·m^3
Water volume	V_w	2.5x10^{-3}	m^3
Heat capacity of water	C_{pw}	75.327	J·mol^{-1}·K^{-1}
Overall heat transfer index	UA	241	W·K^{-1}
Desired FC temperature	$T_{FC,d}$	348	K
Desired excess oxygen ratio	$\lambda_{O_2,d}$	2	N/A

4.3.3.3 Battery Model

The battery model, shown schematically in Fig. 4.20, was used to simulate the battery discharge power (P_{batt}^{dis}) and measured battery SOC (SOC_m) given the requested battery power (P_{batt}^{req}), P_{batt}^{ch}, and T_a.

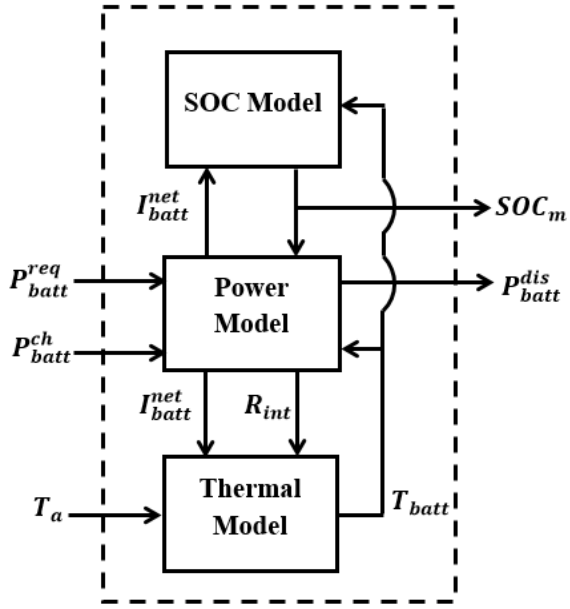

Figure 4.20 Schematic of the battery model.

The battery model is composed of a power model, a thermal model, and a SOC model. The power model determines P_{batt}^{dis} I_{batt}^{net}, and R_{int} given P_{batt}^{req}, P_{batt}^{ch}, the battery temperature (T_{batt}) and SOC_m as follows [89]:

$$\begin{cases} P_{batt}^{dis} = \dfrac{K_{batt}}{\tau_{batt}s + 1} P_{batt}^{req} \\ P_{batt}^{net} = P_{batt}^{dis} - P_{batt}^{ch} \\ I_{batt}^{net} = \dfrac{P_{batt}^{net}}{V_{batt}} \\ V_{batt} = V_{OC} - I_{batt}^{net} R_{int} \\ V_{OC} = V_{OC,nom} - \beta_1(273 + T_{batt})(100 - SOC_m) \\ R_{int} = R_{int,nom}[1 + \beta_1(100 - SOC_m)] \end{cases}, \tag{4.46}$$

where τ_{batt} and K_{batt} are the battery power time constant and gain, respectively (defined in Section 3.2.3.3), P_{batt}^{net} is the net battery power, V_{batt} is the battery voltage, $V_{OC,nom}$ is the nominal battery open-circuit voltage, $R_{int,nom}$ is the nominal battery

internal resistance, and β_1 and β_2 are empirical constants. In Eq. 4.46, T_{batt} is obtained from the battery thermal model developed from a heat balance of the battery:

$$\begin{cases} C_{t,batt}\dfrac{dT_{batt}}{dt} = \dot{Q}_{gen} - \dfrac{T_{batt} - T_a}{R_{t,batt}} \\ \dot{Q}_{gen} = I_{batt}^{net\,2} R_{int} \end{cases}, \tag{4.47}$$

where $C_{t,batt}$ is the battery thermal capacitance, $\dot{Q}_{gen}$ is the internal heat generated from Joule heating, and $R_{t,batt}$ is the battery thermal resistance. Temperature regulation is typically not required for a deep-cycle lead-acid battery. The SOC model is used to compute SOC_m as follows [89]:

$$\begin{cases} SOC_m = \begin{cases} SOC_0 - \dfrac{\eta_{batt,ch}100}{C_{max}}\left[\displaystyle\int_0^t I_{batt}^{net}dt + C_{unavail}\right], & I_{batt}^{net} < 0; \\ SOC_0 - \dfrac{\eta_{batt,dis}100}{C_{max}}\left[\displaystyle\int_0^t I_{batt}^{net}dt + C_{unavail}\right], & I_{batt}^{net} > 0; \\ SOC_0 & I_{batt}^{net} = 0 \end{cases} \\ C_{unavail} = C_{max} - C_{avail} \\ C_{avail} = \dfrac{\beta_3 C_0^* \left(1 + \dfrac{T_{batt}}{T_{batt,f}}\right)^{\beta_4}}{1 + (\beta_3 - 1)\left(\dfrac{I_{batt}^{net}}{I_{batt}^*}\right)^{\beta_5}} \end{cases}, \tag{4.48}$$

where C_{max}, $C_{unavail}$, and C_{avail} are the maximum, unavailable, and available battery charge capacity, respectively, $T_{batt,f}$ is the freezing temperature of the battery electrolyte, I_{batt}^* is the nominal discharge current, C_0^* is the charge capacity at I_{batt}^* and T_{batt} = 0°C, and β_3, β_4, and β_5 are empirical constants. All battery model parameter values are provided in Table 4.10.

Table 4.10 Battery model parameters provided from [89] unless otherwise noted.

Description	Parameter	Value	Units

Nominal battery open-circuit voltage[14]	$V_{OC,nom}$	2.03	V
Nominal battery internal resistance[14]	$R_{int,nom}$	1.12×10^{-4}	Ω
Battery thermal capacitance[15]	$C_{t,batt}$	5.07×10^{5}	$J \cdot °C^{-1}$
Battery thermal resistance[15]	$R_{t,batt}$	1.89	$°C \cdot W^{-1}$
Battery empirical constant 1	β_1	8.93×10^{-4}	$V \cdot °C^{-1}$
Battery empirical constant 2	β_2	-0.2	N/A
Battery empirical constant 3	β_3	1.11	N/A
Battery empirical constant 4	β_4	1.19	N/A
Battery empirical constant 5	β_5	1.75	N/A
Battery electrolyte freezing point	$T_{batt,f}$	-40	°C
Nominal battery discharge current[14]	I^*_{batt}	300	A
Nominal battery charge capacity at I^*_{batt} and T_{batt} = 0°C[14]	C^*_0	3000	Ah
Battery charge efficiency[14]	$\eta_{batt,ch}$	0.86	N/A
Battery discharge efficiency[14]	$\eta_{batt,dis}$	1	N/A

4.3.3.4 Electrolyzer Model

The PEM electrolyzer model (Fig. 4.21) consists of a polarization model, a thermal model, and a hydrogen production model supported by a temperature regulator that maintains the electrolyzer stack temperature (T_{elec}) at a desired value ($T_{elec,d}$).

---

[14] Provided from the Hoppecke 24 OPsZ 3000 manufacturer's brochure.

[15] Since we are using a 3000 Ah battery in this work, these parameter values were assumed to be 9.43 times greater than those for the 317.9 Ah battery system studied in [89].

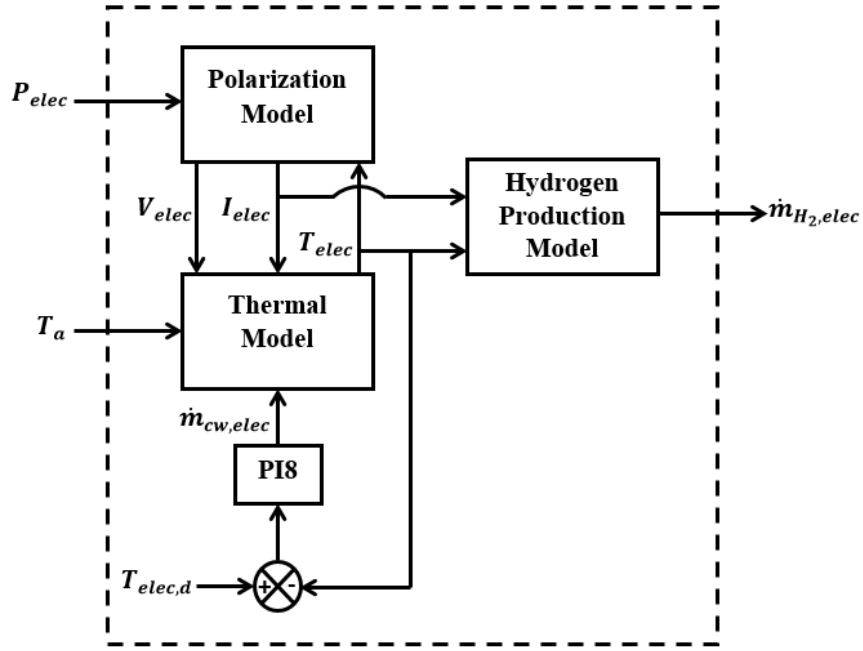

Figure 4.21 Schematic of the electrolyzer model. The heat exchanger cooling water flowrate ($\dot{m}_{cw,elec}$) is determined by a PI controller (PI8) that acts to match T_{elec} to $T_{elec,d}$. The controller gains of PI8 are as follows: K_p = -0.4 and K_i = -3.8x10^{-3}.

The polarization model determines the electrolyzer voltage (V_{elec}) and current (I_{elec}) given P_{elec} and T_{elec} as follows [44,90]:

$$\begin{cases} V_{elec} = n_{cell,elec}\left(E_{elec} + V_{act,elec} + V_{ohm,elec}\right) \\ I_{elec} = \dfrac{P_{elec}}{V_{elec}} \\ E_{elec} = 1.5 - 1.5x10^{-3}T_{elec} + 9.5x10^{-5}T_{elec}\ln(T_{elec}) + 9.84x10^{-8}T_{elec}^2 \\ V_{act,elec} = \dfrac{R_{gas}T_{elec}}{\alpha 2F}\ln\left(\dfrac{I_{elec}}{I_{elec,0}}\right) \\ V_{ohm,elec} = I_{elec}R_{eq} \end{cases}, \quad (4.49)$$

where $n_{cell,elec}$ is the number of cells connected in series in the electrolyzer stack, E_{elec} is the electrolyzer thermodynamic potential (for degrees Kelvin), $V_{act,elec}$ is the

electrolyzer activation overpotential, $V_{ohm,elec}$ is the ohmic overpotential, α is the charge transfer coefficient, $I_{elec,0}$ is the electrolyzer exchange current, and R_{eq} is the electrolyzer equivalent internal resistance. The thermal model is the result of a heat balance around the electrolyzer [44]:

$$\begin{cases} C_{t,elec}\dfrac{dT_{elec}}{dt} = \dot{Q}_{gen} - \dot{Q}_{loss} - \dot{Q}_{cool} \\ \dot{Q}_{gen} = I_{elec}\left(V_{elec} - n_{cell,elec}E_{tn}\right) \\ \dot{Q}_{loss} = \dfrac{T_{elec} - T_a}{R_{th,elec}} \end{cases}, \tag{4.50}$$

where $C_{t,elec}$ is the electrolyzer thermal capacitance, $\dot{Q}_{gen}$ is the electrolyzer heat generation, $\dot{Q}_{loss}$ is the electrolyzer heat lost to the environment, $\dot{Q}_{cool}$ is the electrolyzer heat lost to a water-cooled heat exchanger, E_{tn} is the thermoneutral potential for water splitting at $T_{elec,d}$, and $R_{th,elec}$ is the electrolyzer thermal resistance. The electrolyzer water-cooled heat exchanger is identical to that described in Section 4.3.3.2. The hydrogen production model, which accounts for losses due to the dryer, deoxidizer, and safety purging, determines the hydrogen flowrate from the electrolyzer given T_{elec} and I_{elec} [44]:

$$\begin{cases} \dot{m}_{H_2,th} = \dfrac{n_{cell,elec}I_{elec}/2F}{\tau_{elec}s + 1} \\ \dot{m}_{H_2,elec} = \dot{m}_{H_2,th}\eta_{H_2} \\ \eta_{H_2} = \dfrac{a_1}{100}\exp\left(\dfrac{a_2 + a_3T_{elec}}{I_{elec}}\right) \end{cases} \tag{4.51}$$

where $\dot{m}_{H_2,th}$ is the theoretical hydrogen flowrate, τ_{elec} is the electrolyzer time constant, η_{H_2} is the hydrogen production efficiency, and a_1, a_2, and a_3 are empirical constants. All electrolyzer model parameter values are listed in Table 4.11.

Table 4.11 Electrolyzer model parameters provided in [44] unless otherwise noted.

Description	Parameter	Value	Units
Number of cells connected in series[16]	$n_{cell,elec}$	36	N/A
Universal gas constant	R_{gas}	8.314	J·mol^{-1}·°C^{-1}
Charge transfer coefficient	α	0.5	N/A
Electrolyzer exchange current[16]	$I_{elec,0}$	1.125x10^{-9}	A
Electrolyzer equivalent internal resistance	R_{eq}	108.75	Ω
Electrolyzer thermal capacitance[16]	$C_{t,elec}$	1.26x10^{5}	J·°C^{-1}
Electrolyzer thermoneutral potential[17]	E_{tn}	1.42	V
Electrolyzer thermal resistance[16]	$R_{th,elec}$	0.245	°C·W^{-1}
Electrolyzer time constant	τ_{elec}	5	s
Electrolyzer empirical constant 1	a_1	57.1081	%
Electrolyzer empirical constant 2	a_2	-1.6996097x10^{3}	A
Electrolyzer empirical constant 3	a_3	1.0304	A·°C^{-1}
Desired Electrolyzer temperature	$T_{elec,d}$	40	°C

4.3.3.5 Hydrogen Storage Model

The hydrogen storage model was used to simulate the measured hydrogen tank level ($L_{H_2,m}$) given $\dot{m}_{H_2,elec}$. First, the number of moles of hydrogen entering the storage tanks (n_{mol,H_2}) was obtained from:

$$n_{mol,H_2} = n_{mol,H_2,0} \int_0^t \dot{m}_{H_2,elec} dt \,, \tag{4.52}$$

where $n_{mol,H_2,0}$ is the moles of hydrogen in the storage tank at the previous time step. Next, the storage tank pressure ($P_{H_2,tank}$) was determined using the Benedict-Webb-Rubin (BWR) equation of state (EOS) [91]:

---

[16] Since we are using a 3 kW electrolyzer in this work, these parameter values were assumed to be 3 times greater than those for the 1 kW electrolyzer system studied in [44].

[17] The electrolyzer thermoneutral potential is for water splitting at 40°C [104].

$$P_{H_2,tank} = R_{gas}T_a\rho_m + \left(B_0R_{gas}T_a - A_0 - \frac{C_0}{T_a^2}\right)\rho_m^2 + \left(bR_{gas}T_a - a\right)\rho_m^3 + a\alpha\rho_m^6 + \frac{c}{T_a^2}(1+\gamma\rho_m^2)\exp(-\gamma\rho_m^2)\rho_m^3, \tag{4.53}$$

where ρ_m is the hydrogen molar density given by

$$\rho_m = \frac{n_{mol,H_2}}{V_{tank}}, \tag{4.54}$$

V_{tank} is the storage tank volume, and B_0, A_0, C_0, b, a, α, c, and γ are empirical constants. The BWR EOS is an accurate assessment of hydrogen pressure while T_a is between 273 K and 423 K, and while ρ_m/ρ_c < 2.5, where ρ_c is the critical molar density of hydrogen. Lastly, $L_{H_2,m}$ is expressed as:

$$L_{H_2,m} = 100\left(\frac{P_{H_2,tank}}{P_{H_2,rated}}\right), \tag{4.55}$$

where $P_{H_2,rated}$ is the storage tank rated pressure. All hydrogen storage tank model parameters are provided in Table 4.12.

Table 4.12 Hydrogen storage tank parameters provided in [91] unless otherwise noted.

Description	Parameter	Value	Units
Universal gas constant	R_{gas}	$8.2057\text{x}10^{-2}$	$L\cdot atm\cdot K^{-1}\cdot mol^{-1}$
Storage tank volume[18]	V_{tank}	258	L
BWR EOS empirical constant 1	B_0	$1.8041\text{x}10^{-2}$	$L\cdot mol^{-1}$
BWR EOS empirical constant 2	A_0	$9.7319\text{x}10^{-2}$	$L^2\cdot atm\cdot mol^{-2}$
BWR EOS empirical constant 3	C_0	$3.8914\text{x}10^{2}$	$L^2\cdot atm\cdot K\cdot mol^{-2}$
BWR EOS empirical constant 4	b	$1.7976\text{x}10^{-4}$	$L^2\cdot mol^{-2}$
BWR EOS empirical constant 5	a	$-9.2211\text{x}10^{-3}$	$L^3\cdot atm\cdot mol^{-3}$
BWR EOS empirical constant 6	α	$-3.4215\text{x}10^{-6}$	$L^3\cdot mol^{-3}$
BWR EOS empirical constant 7	c	$-2.4613\text{x}10^{2}$	$L^3\cdot atm\cdot K^2\cdot mol^{-3}$

[18] Parameter provided in [80].

BWR EOS empirical constant 8	γ	1.89x10^{-3}	L^2·mol^{-2}
Storage tank rated pressure[18]	$P_{H_2,rated}$	345.42	atm

4.3.4 Controller Development

The PV/FC/battery HRES control objectives are: 1) to satisfy the home's required power demand; and 2) to maintain the battery SOC and hydrogen tank level at 65% and 100%, respectively. Thus, the control variables (CVs) for this system are the combined PV, WT, FC, and battery power output (P_{total}), the measured battery SOC (SOC_m), and the measured hydrogen tank level ($L_{H_2,m}$), while their desired setpoints (SPs) are P_{demand}, the desired battery SOC (SOC_d), and the desired hydrogen tank level ($L_{H_2,d}$). The available manipulated variables (MVs) are a signal requesting FC power (P_{FC}^{req}), a signal requesting battery power (P_{batt}^{req}), excess power sent to the electrolyzer (P_{elec}), and excess power sent to charge the battery (P_{batt}^{ch}). The disturbance variables (DVs) in this system, which affect the CVs but cannot be manipulated, are power produced by the PV array (P_{PV}) and power produced by the WT array (P_{WT}).

The objective of the control strategy design is to use the MVs to drive the CVs to their SPs despite any uncontrollable fluctuations in the DVs. To achieve this objective, a data-driven model predictive controller was developed, which consists of a standard MPC algorithm supported by measured disturbance prediction and model adaptation (Fig. 4.22). The measured disturbance prediction algorithm uses solar irradiance (G_T) and wind speed (v) data to fit separate adaptive ARIMA time-series models, which are used to predict future values of P_{PV} and P_{WT}. The disturbance variable predictions (DV_{pred}) are used directly by the MPC strategy to calculate more suitable values of MVs required to accommodate the disturbances. The model

adaptation algorithm uses subspace identification of MV and CV data to approximate a linear state-space model of the non-linear, time-variant HRES at current operating conditions (SS_{new}), thereby improving controller performance. Each component of the data-driven model predictive controller is described in the remainder of this Section.

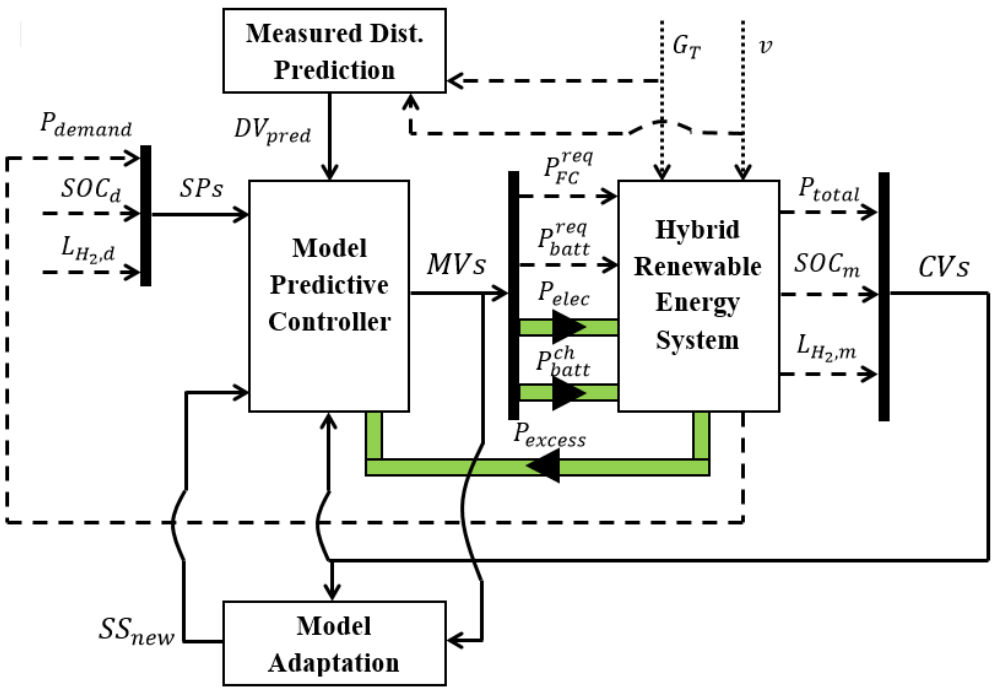

Figure 4.22 Control block diagram of the data-driven model predictive controller used for the PV/WT/FC/battery/electrolyzer HRES. Light green lines indicate AC power while their black solid arrows show the directional flow of AC power. Black dotted lines represent inputs to the HRES's disturbance variables. Black dashed lines represent flow of information. Black solid lines indicate a vector of signals.

4.3.4.1 Model Predictive Control

Model predictive control (MPC) is a model-based controller used to compute optimal process inputs ($u(k)$) that drive process outputs ($y(k)$) to their desired

setpoints ($y_{SP}(k)$) by minimizing an objective function. The model for a model predictive controller is typically given in discrete state-space form as follows:

$$\begin{cases} x(k+1) = Ax(k) + Bu(k) \\ y(k) = Cx(k) + Du(k) \end{cases} \tag{4.56}$$

where k is the sampling time, A is the state matrix, B is the input matrix, C is the output matrix, D is the feedthrough matrix. The initial state-space model of the HRES was determined using the System Identification Toolbox in Matlab, which provided a first-order linearized HRES model expressed as:

$$\begin{cases} y = \begin{bmatrix} P_{total} & SOC_m & L_{H_2,m} \end{bmatrix}^T \\ u = \begin{bmatrix} P_{FC}^{req} & P_{batt}^{req} & P_{elec} & P_{batt}^{ch} & P_{PV} & P_{WT} \end{bmatrix}^T \\ A = \begin{bmatrix} -0.5576 & 0 & 0 & 0 \\ 0 & -0.3869 & 0 & 0 \\ 0 & 0 & 0 & 0 \\ 0 & 0 & 0 & 0 \end{bmatrix} \\ B = \begin{bmatrix} 1 & 0 & 0 & 0 & 0 & 0 \\ 0 & 0.5 & 0 & 0 & 0 & 0 \\ 0 & -4.289x10^{-4} & 0 & 4.96x10^{-4} & 0 & 0 \\ -2.89x10^{-4} & 0 & 3.21x10^{-4} & 0 & 0 & 0 \end{bmatrix} \\ C = \begin{bmatrix} 0.5655 & 0.7777 & 0 & 0 \\ 0 & 0 & 0 & 9.766x10^{-4} \\ 0 & 0 & 9.766x10^{-4} & 0 \end{bmatrix} \\ D = \begin{bmatrix} 0 & 0 & 0 & 0 & 1 & 1 \\ 0 & 0 & 0 & 0 & 0 & 0 \\ 0 & 0 & 0 & 0 & 0 & 0 \end{bmatrix} \end{cases}. \tag{4.57}$$

The model predictive controller objective function is given by:

$$\min_{u(k)} J(x(t), u(t), t) = \begin{cases} \sum_{k=1}^{N_p} W_y [y(k) - y_{SP}(k)]^2 \\ + \sum_{k=1}^{N_c} W_u \left[u(k) - u_{target}(k)\right]^2 \\ + \sum_{k=1}^{N_c} W_{\Delta u} [\Delta u(k|k+1)]^2 \end{cases} \tag{4.58}$$

$$\text{subject to: } \begin{cases} y_{min} \le y(k) \le y_{max} \\ u_{min} \le u(k) \le u_{max} \\ \Delta u_{min} \le \Delta u(k) \le \Delta u_{max} \end{cases} \tag{4.59}$$

where $x(t)$ is a vector of states of the system at time t, $u(t)$ is a vector of inputs at time t, N_p is the prediction horizon (expressed in the number of control intervals) over which the objective function is minimized, N_c is the control horizon (also expressed in the number of control intervals) over which future control moves are computed ($N_c \leq N_p$), W_y, W_u, and $W_{\Delta u}$ are weight factors for outputs, inputs, and changes in inputs, respectively, $\Delta u(k|k+1)$ is a vector of changes in inputs at the kth step in the prediction horizon, and $u_{target}(k)$ is a vector of target input values at the kth step in the prediction horizon (typically used if there are inputs unused in the control of outputs in over-determined control systems). The objective function in Eq. 4.58 is typically subject to a set of constraints as shown in Eq. 4.59, where $y_{min}, u_{min},$ and Δu_{min} are vectors of the minimum allowable outputs, inputs, and change in inputs, respectively, and $y_{max}, u_{max},$ and Δu_{max} are vectors of the maximum allowable outputs, inputs, and change in inputs, respectively.

The MPC tuning parameters and constraints used here are provided in Table 4.13. Note that the weight factor for each CV is equal because each of their desired values are equally important to reach. The weight factor for the change in P_{FC}^{req} is orders of magnitude larger than P_{batt}^{req} because the lifetime of a FC can be extended by preventing large fluctuations in its power output [92], while the power output of a battery can vary greatly without significant degradation.

Table 4.13 MPC tuning parameters and constraints.

Description	Symbol	Value	Units
Control interval	N/A	1	s
Prediction horizon over which the objective function is minimized	N_p	60	s

Control horizon over which future control moves are computed	N_c	5	s
Weight factor for P_{total}	$W_{P_{total}}$	1	N/A
Weight factor for SOC_m	W_{SOC_m}	1	N/A
Weight factor for $L_{H_2,m}$	$W_{L_{H_2,m}}$	1	N/A
Weight factor for P_{FC}^{req}	$W_{P_{FC}^{req}}$	$5x10^{-4}$	N/A
Weight factor for P_{batt}^{req}	$W_{P_{batt}^{req}}$	$5x10^{-4}$	N/A
Weight factor for P_{elec}	$W_{P_{elec}}$	0	N/A
Weight factor for P_{batt}^{ch}	$W_{P_{batt}^{ch}}$	0	N/A
Weight factor for the change in P_{FC}^{req}	$W_{\Delta P_{FC}^{req}}$	$4x10^{-3}$	N/A
Weight factor for the change in P_{batt}^{req}	$W_{\Delta P_{batt}^{req}}$	$1x10^{-10}$	N/A
Weight factor for the change in P_{elec}	$W_{\Delta P_{elec}}$	$1x10^{-3}$	N/A
Weight factor for the change in P_{batt}^{ch}	$W_{\Delta P_{batt}^{ch}}$	$1x10^{-3}$	N/A
Minimum and maximum allowed value for P_{total}	$[P_{total,min}, P_{total,max}]$	[0,inf]	W
Minimum and maximum allowed value for SOC_m	$[SOC_{m,min}, SOC_{m,max}]$	[30,100]	%
Minimum and maximum allowed value for $L_{H_2,m}$	$[L_{H_2,m,min}, L_{H_2,m,max}]$	[0,100]	%
Minimum and maximum allowed value for P_{FC}^{req}	$[P_{FC,min}^{req}, P_{FC,max}^{req}]$	[0,3000]	W
Minimum and maximum allowed value for P_{batt}^{req}	$[P_{batt,min}^{req}, P_{batt,max}^{req}]$	[0,3660]	W
Minimum and maximum allowed value for P_{elec}	$[P_{elec,min}, P_{elec,max}]$	[0,3000]	W
Minimum and maximum allowed value for P_{batt}^{ch}	$[P_{batt,min}^{ch}, P_{batt,max}^{ch}]$	[0,3660]	W
Minimum and maximum allowed value for the change in P_{FC}^{req}	$[\Delta P_{FC,min}^{req}, \Delta P_{FC,max}^{req}]$	[-inf,inf]	W
Minimum and maximum allowed value for the change in P_{batt}^{req}	$[\Delta P_{batt,min}^{req}, \Delta P_{batt,max}^{req}]$	[-inf,inf]	W
Minimum and maximum allowed value for the change in P_{elec}	$[\Delta P_{elec,min}, \Delta P_{elec,max}]$	[-inf,inf]	W
Minimum and maximum allowed value for the change in P_{batt}^{ch}	$[\Delta P_{batt,min}^{ch}, \Delta P_{batt,max}^{ch}]$	[-inf,inf]	W

4.3.4.2 Measured Disturbance Prediction

Because the prediction horizon of the model predictive controller is 1 minute and new G_T and v measurements are only available once per minute, we are only interested in computing the next-step-ahead (1 minute ahead) prediction of P_{PV} ($P_{PV,t+1}$) and P_{WT} ($P_{WT,t+1}$). To obtain $P_{PV,t+1}$ and $P_{WT,t+1}$, we must first determine the next-step-ahead predictions of G_T and v ($G_{T,t+1}$ and v_{t+1}). At our desired temporal prediction resolution (1 minute ahead), ARIMA time series models have G_T and v prediction capabilities superior to numerical weather prediction and artificial neural networks [93–95]. Therefore, we predicted $G_{T,t+1}$ and v_{t+1} using two separate ARIMA time-series models of the following form:

$$X_t = \sum_{i=1}^{p} \varphi_i X_{t-i} - \sum_{i=1}^{d} -X_{t-i} + \sum_{i=1}^{q} \theta_i \varepsilon_{t-i} + \varepsilon_t \tag{4.60}$$

where X_t is a time series containing data of either G_T or v, p is the autoregressive (AR) order, φ_i are the AR parameters, d is the differencing or integrating (I) order, q is the moving average (MA) order, θ_i are the MA parameters, and ε_t are white noise error terms. The model orders (p, d, and q) and model coefficients (φ_i and θ_i) in Eq. 4.60 are typically determined for a given X_t and remain unchanged while predicting future values of X_t (X_{t+1}).

However, we wish to add an adaptive mechanism to the ARIMA time-series model that will provide more accurate P_{PV} and P_{WT} predictions to the model predictive controller. Therefore, X_t must be updated such that when new G_T and v data become available, the newest datum is added to each respective X_t and the oldest

datum is deleted (X_t remains a constant size containing N_{ts} number of data samples[19]). This "moving window" approach adapts each ARIMA model to changing conditions while removing data that is no longer representative of current operating conditions.

Once X_t is updated with new data, the first step in obtaining a new prediction model is to determine the value of d by using the Kwiatkowski, Phillips, Schmidt, and Shin (KPSS) statistical hypothesis test for stationarity of X_t [96], which must be stationary (i.e., exhibit no significant trends) to estimate an accurate ARIMA model. If there is no evidence to reject the null hypothesis of the KPSS test, then d = 0 in Eq. 5 and X_t does not need to be differenced. Otherwise, X_t is differenced and the KPSS test is used on the new differenced X_t. The differencing continues until the differenced X_t is deemed stationary and d is simply the number of times the data was differenced.

Next, X_t (or the differenced X_t) is used to estimate φ_i and θ_i via maximum likelihood estimation for values of p and q ranging from 0 to the maximum allowable AR and MA model order (pq_{max}). In the case of both G_T or v, we determined that pq_{max} = 3 (Appendix B). As a result, a set of 9 ARIMA time-series models are estimated each for G_T or v.

The optimal ARIMA model is then selected on the basis of yielding the least amount of information loss. Three common measures of model information loss are the Bayesian Information Criteria (BIC), Akaike Information Criteria (AIC), and Corrected Akaike Information Criteria (AICc). The AICc measure for information loss yielded the lowest MSPE for both G_T and v (Appendix B), which agrees well with

---

[19] The optimal sizes of N_{ts} for G_T and v, which resulted in the lowest mean square prediction error (MSPE), were determined to be 210 and 180, respectively (Appendix A).

other information criteria method comparisons in the literature [97–99]. Hence, the AICc was used to determine the optimal ARIMA time-series model for predicting $G_{T,t+1}$ and v_{t+1}, which were obtained from:

$$X_{t+1} = \sum_{i=1}^{p} \varphi_i X_{t-i+1} - \sum_{i=1}^{d} X_{t-i+1} + \sum_{i=1}^{q} \theta_i \varepsilon_{t-i+1} + \varepsilon_{t+1}. \tag{4.61}$$

After predicting $G_{T,t+1}$ and v_{t+1}, they are used to obtain $P_{PV,t+1}$ and $P_{WT,t+1}$, by utilizing steady-state PV and WT power curves (Fig. 4.23 and Fig. 4.24, respectively). The PV and WT steady-state power curves were determined using Simulink models of each respective component (see Section 4.3.3).

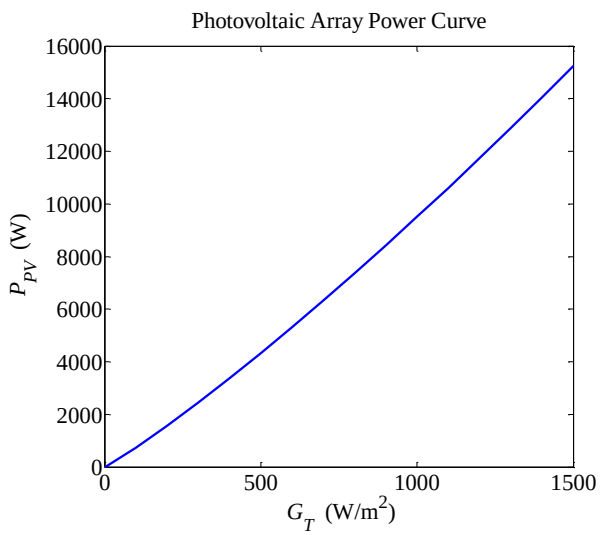

Figure 4.23 PV array power (P_{PV}) as a function of solar irradiance (G_T) at constant ambient temperature (T_a = 301.24 K).

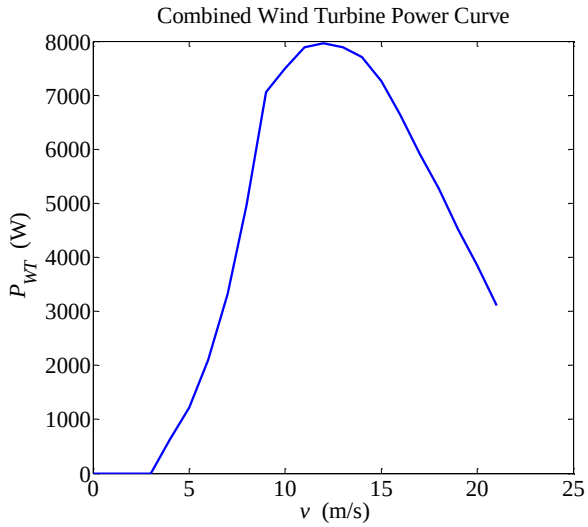

Figure 4.24 Combined power from all three WTs (P_{WT}) as a function of wind speed (v) at constant ambient temperature (T_a = 301.24 K).

Finally, $P_{PV,t+1}$ and $P_{WT,t+1}$ are implemented into the prediction horizon of the model predictive controller. When new solar and wind measurements become available, X_t is updated, the model identification process is repeated, and new P_{PV} and P_{WT} predictions are made. For clarity, the entire adaptive ARIMA time-series modeling procedure is summarized in Fig. 4.25.

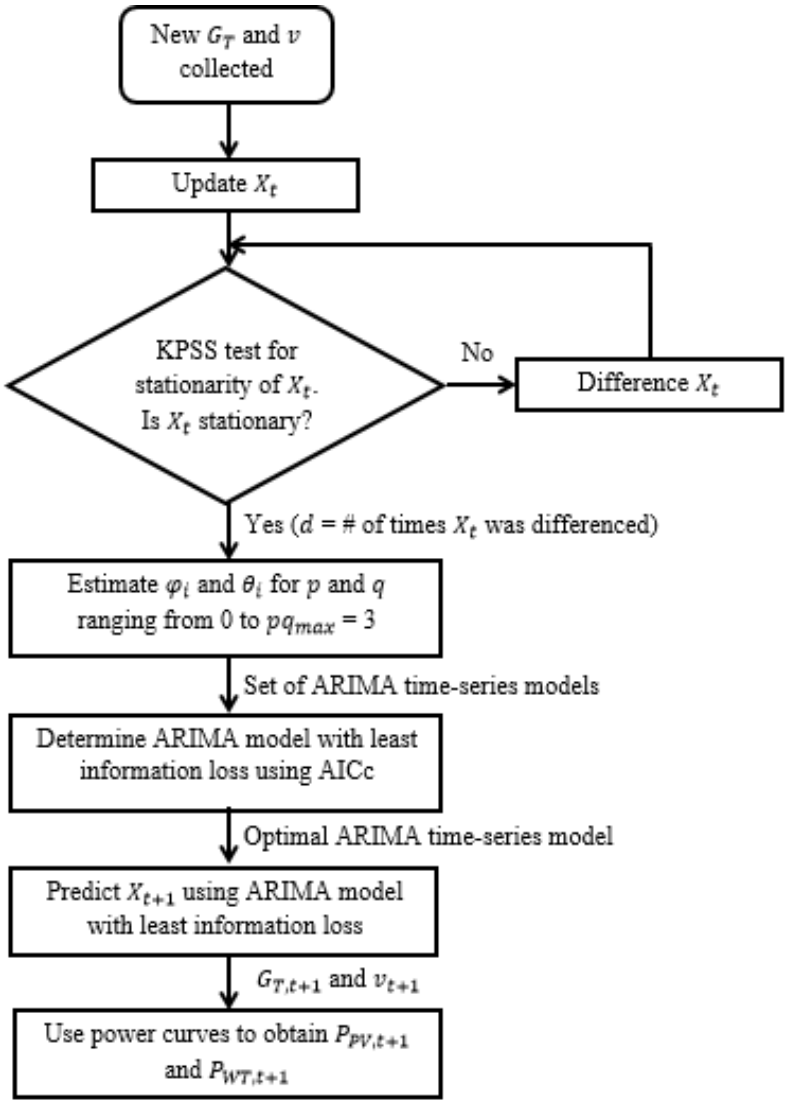

Figure 4.25 Flowchart describing the adaptive ARIMA time-series modeling algorithm for measured disturbance prediction.

4.3.4.3 Model Adaptation

The linear state-space model provided in Eq. 4.23 was updated using a closed-loop version of subspace identification, which uses closed-loop MV and CV data to

determine the new state-space model matrices (SS_{new}) at current operating conditions. Closed-loop subspace identification applies to the closed-loop form of Eq. 4.56:

$$\begin{cases} x(k+1) = \tilde{A}x(k) + \tilde{B}u(k) + Ky(k) \\ y(k) = Cx(k) + Du(k) \end{cases} \tag{4.62}$$

where

$$\begin{aligned} \tilde{A} &= A - KC \\ \tilde{B} &= B - KD' \end{aligned} \tag{4.63}$$

and K is the Kalman filter gain.

To determine A, B, C, D, and K using subspace identification, the $u(k)$, $y(k)$, and $x(k)$ data for $k \in \{0,1,\dots,N\}$ must first be transformed into block Hankel matrices. As an example, the block Hankel matrices of $u(k)$ for $k \in \{1,2,\dots,N\}$ are given as [100]:

$$U_p = \begin{bmatrix} u(1) & u(2) & \cdots & u(N-h-i+1) \\ u(2) & u(3) & \cdots & u(N-h-i+2) \\ \vdots & \vdots & \ddots & \vdots \\ u(i) & u(i+1) & \cdots & u(N-h) \end{bmatrix} \tag{4.64}$$

and

$$U_f = \begin{bmatrix} u(i+1) & u(i+2) & \cdots & u(N-h+1) \\ u(i+2) & u(i+3) & \cdots & u(N-h+2) \\ \vdots & \vdots & \ddots & \vdots \\ u(i+h) & u(i+h+1) & \cdots & u(N) \end{bmatrix} \tag{4.65}$$

where U_p is a matrix of past inputs, U_f is a matrix of future inputs, N is the total number of measurements (2000), i is the number of past measurements (2), and h is the number of future measurements (2). The block Hankel matrices for $y(k)$ (Y_p and Y_f) can be expressed in a similar manner while $x(k)$ can be expressed as:

$$X_p = [x(1) \quad x(2) \quad \cdots \quad x(N-h-i+1)] \tag{4.66}$$

and

$$X_f = [x(i+1) \quad x(i+2) \quad \cdots \quad x(N-h+1)] \tag{4.67}$$

where X_p is a vector of past states and X_f is a vector of future states. The block Hankel matrices are updated with new data when it becomes available and the oldest data is removed. Thus, N remains constant and the black Hankel matrices contain process data at the most current operating conditions.

The block Hankel matrices can then be recursively substituted into Eq. 4.28, resulting in an output prediction model of the following form:

$$Y_f = \tilde{\Gamma} X_f + \tilde{H} U_f + \tilde{H}^s Y_f \tag{4.68}$$

where

$$\tilde{\Gamma} = \begin{bmatrix} C \\ C\tilde{A} \\ \vdots \\ C\tilde{A}^{h-1} \end{bmatrix}, \quad \tilde{H} = \begin{bmatrix} D & 0 & \cdots & 0 \\ C\tilde{B} & D & \cdots & 0 \\ \vdots & \vdots & \ddots & \vdots \\ C\tilde{A}^{h-2}\tilde{B} & C\tilde{A}^{h-3}\tilde{B} & \cdots & D \end{bmatrix}, \quad \text{and}$$

$$\tilde{H}^s = \begin{bmatrix} 0 & 0 & \cdots & 0 \\ CK & 0 & \cdots & 0 \\ \vdots & \vdots & \ddots & \vdots \\ C\tilde{A}^{h-2}K & C\tilde{A}^{h-3}K & \cdots & 0 \end{bmatrix}. \tag{4.69}$$

The state-space matrices are then determined from the SSARX method described in [101], but are only used to update the model predictive controller if the new model achieves better output prediction than the old model according to the adaptive strategy described in [100].

4.3.5 Controller Evaluation

4.3.5.1 Evaluation Design

The data-driven MPC strategy described in Section 4.3.4 was tested by using it to meet the operating objectives of a simulated PV/WT/FC/battery/electrolyzer HRES for a single-family home in Newark, DE during a 24-hour period in the summer. The

HRES was simulated during the 24-hour period using power demand, solar irradiance, wind speed, and ambient temperature (T_a) profiles (Fig. 4.26). The power demand profile of the single-family home (Fig. 4.26a) is a distribution of power intensity based on the approximate daily delivered energy consumption of a home in the United States in the summer (~30 kWh in 2012 [2]). From midnight to 6 a.m., the power demand is only ~700 W since many appliances are not used, lights are turned off, and air conditioning is either low or off. At 6 a.m., appliances and lights may be used as the home occupants prepare for work/school, and air conditioning is used more as temperatures begin to rise. Consequently, the power demand increases to ~1,400 W until 6 p.m., at which time the home occupants return, appliances and lights are used readily, and more air conditioning is needed to cool the occupants. The peak power demand (~2,300 W) occurs at 8 p.m. and then tapers to ~ 900 W by 12 a.m. as the home occupants begin sleeping and outdoor temperatures decline. The solar irradiance, wind speed, and ambient temperature profiles (Fig. 4.26b, 4.26c, and 4.26d, respectively) were obtained by meteorologists at New Castle County Airport on July 15th, 2013 at one minute intervals. Intermittent cloud cover (~6:30 a.m. to ~8:30 a.m. and ~12 p.m. to ~6 p.m.), wind gusts over 8 m/s (~12 a.m., ~3:30 p.m., and ~8 p.m.), and fluctuations in temperature occur during some periods of the day. Such inconsistent weather conditions are useful for evaluating the robustness of the data-driven MPC strategy.

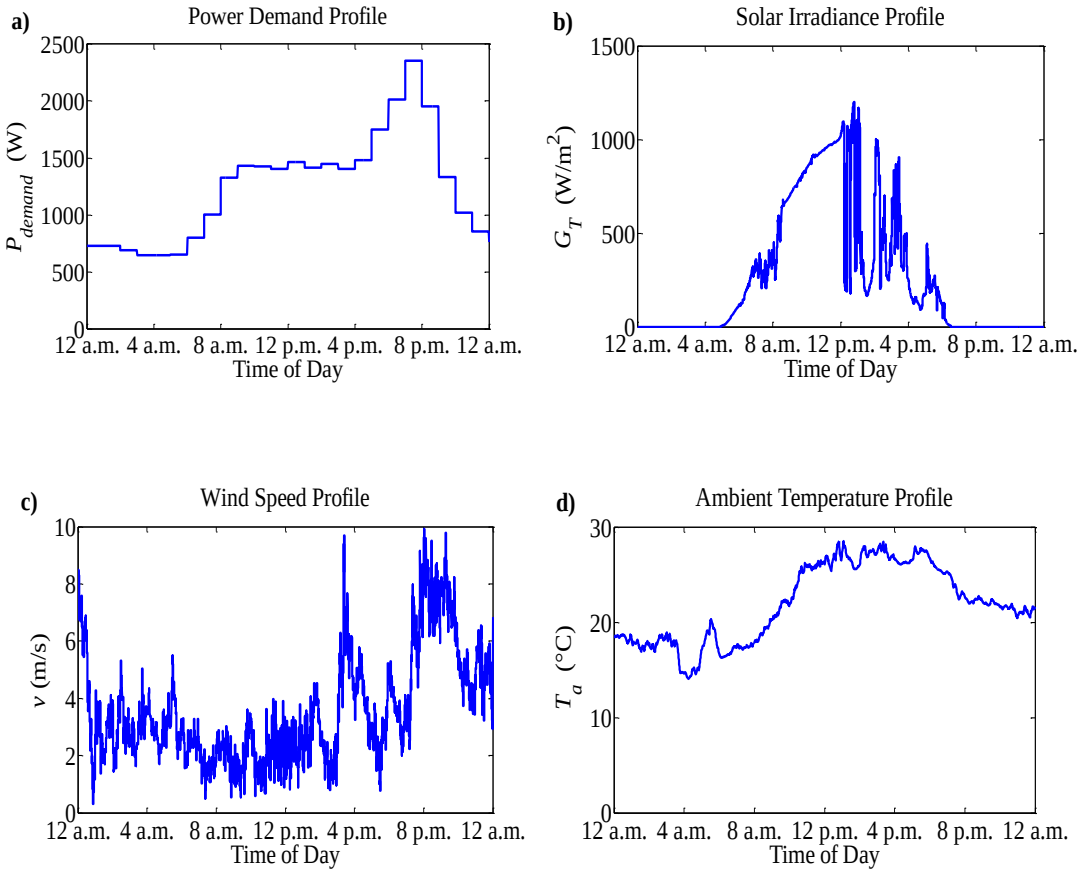

Figure 4.26 Data profiles used to simulate the PV/WT/FC/battery/electrolyzer HRES during a 24-hour period in the summer: **a)** power demand; **b)** solar irradiance; **c)** wind speed; and **d)** ambient temperature.

The effectiveness of the data-driven MPC strategy was evaluated under the following assumptions:

1. Each PV array module is exposed to the same solar irradiance and ambient temperature.

2. Each WT is exposed to the same wind speed, ambient temperature, and atmospheric pressure (101325 Pa).

3. The FC has no parasitic power losses.

4. The AC/AC converter, inverters, and rectifiers operate at steady-state and at 90% efficiency.

5. The battery SOC and H_2 tank level are each initially at 50%.

4.3.5.2 Evaluation Results

4.3.5.2.1 Measured Disturbance Prediction

Predictions of P_{PV} and P_{WT} were obtained using the adaptive ARIMA time-series modeling methodology described in Section 4.3.4.2. We first assessed the P_{PV} and P_{WT} prediction accuracy qualitatively by comparing the next-step-ahead predictions of G_T and v to the actual values of G_T and v (Fig. 4.27 and Fig. 4.28, respectively). Most observed values of G_T and v remain within the 95% prediction interval bounds and accurate predictions of G_T and v were attained despite fluctuations in G_T and v. Our results suggests that accurate P_{PV} and P_{WT} predictions can be derived from our predictions of G_T and v.

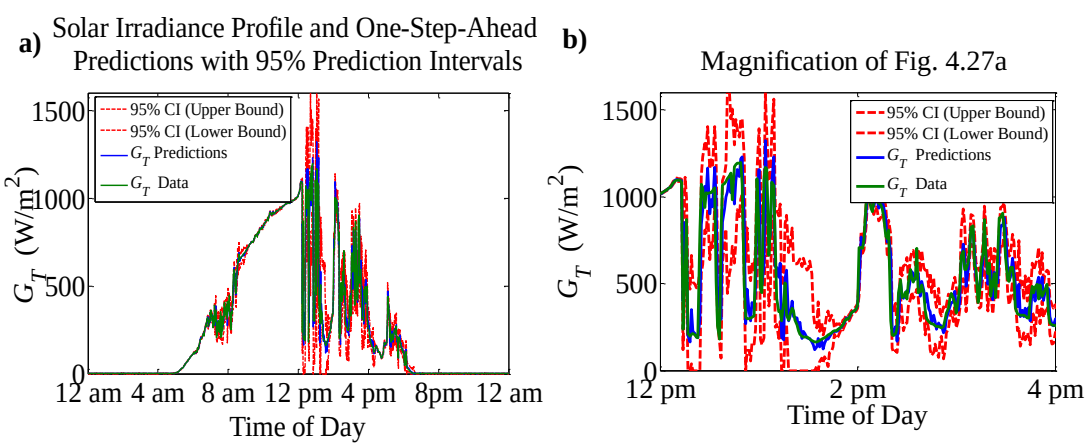

Figure 4.27 **a)** Solar irradiance (G_T) profile (green line) with next-step-ahead predictions (blue line) and 95% prediction interval bounds (red dashed lines) for the 24-hour simulation period; and **b)** a magnification of **a)** from 12 p.m. to 4 p.m.

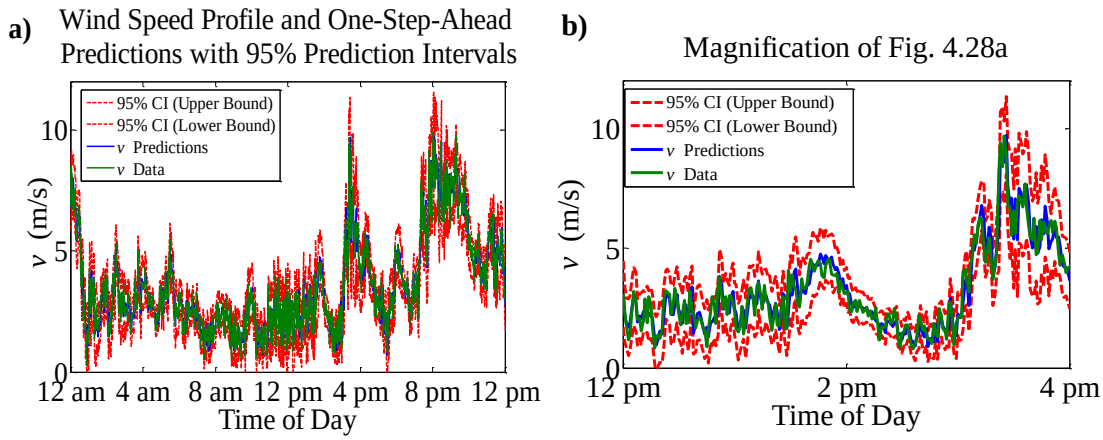

Figure 4.28 **a)** Wind Speed (G_T) profile (green line) with next-step-ahead predictions (blue line) and 95% prediction interval bounds (red dashed lines) for the 24-hour simulation period; and **b)** a magnification of **a)** from 12 p.m. to 4 p.m.

Next, we assessed the P_{PV} and P_{WT} prediction accuracy quantitatively by comparing the mean square prediction error (MSPE) of G_T and v predictions acquired via adaptive ARIMA time-series modeling and a persistence model[20] (Table 4.14). Our results indicate that the adaptive ARIMA time-series model predictions of G_T and v are more accurate than the persistence model predictions of G_T and v (~20% and ~40% reduction in MSPE, respectively). Because the default values of P_{PV} and P_{WT} in the MPC prediction horizon are determined using a persistence model when no external predictions are provided, we expect that using G_T and v predictions from adaptive ARIMA time-series modeling will yield more accurate P_{PV} and P_{WT} predictions, thereby improving control performance.

[20] All persistence model predictions are equal to the most recent measured value.

Table 4.14 MSPE for solar irradiance (G_T) and wind speed (v) predictions obtained from a persistence model and an adaptive ARIMA time-series model.

Variable	Persistence Model MSPE	Adaptive ARIMA Time-series model MSPE
G_T	3174 W^2/m^4	2580 W^2/m^4
v	0.3374 m^2/s^2	0.2050 (m^2/s^2)

The results of simulating the PV/WT/FC/battery/electrolyzer HRES operation with and without measured disturbance prediction are provided in Fig. 4.29 and Fig. 4.30. As shown in Fig. 4.29a, the power demand setpoint was tracked reasonably well with or without measured disturbance prediction when P_{PV} and P_{WT} combined were less than P_{demand} (prominent from ~12:30 a.m. to ~6:00 a.m. and ~4:30 p.m. to ~8:00 p.m.). Fig. 4.29b reveals that under this condition, our measured disturbance prediction approach more often than not improved power demand setpoint tracking. The improved power demand setpoint tracking is a result of changes in P_{FC}^{req} and P_{batt}^{req} (shown in Fig. 4.29c and in detail in Fig. 4.29d) needed to accommodate predicted changes in future P_{PV} and P_{WT}. In some instances, however, better power demand setpoint tracking was achieved without measured disturbance prediction (see ~6:20 p.m. in Fig. 4.29b). Such an event can occur because when no external measured disturbance prediction is supplied, the persistence model predictions used by default in the MPC strategy were occasionally superior to the adaptive ARIMA time-series model predictions. When P_{PV} and P_{WT} were in excess of P_{demand} (prominent from ~6:00 a.m. to ~4 p.m. and from ~8 p.m. to ~10 p.m.), the power demand setpoint was tracked nearly perfectly with or without measured disturbance prediction because P_{PV} and P_{WT} are first used to match P_{demand}, with the remaining excess power stored as hydrogen using the electrolyzer or in the battery.

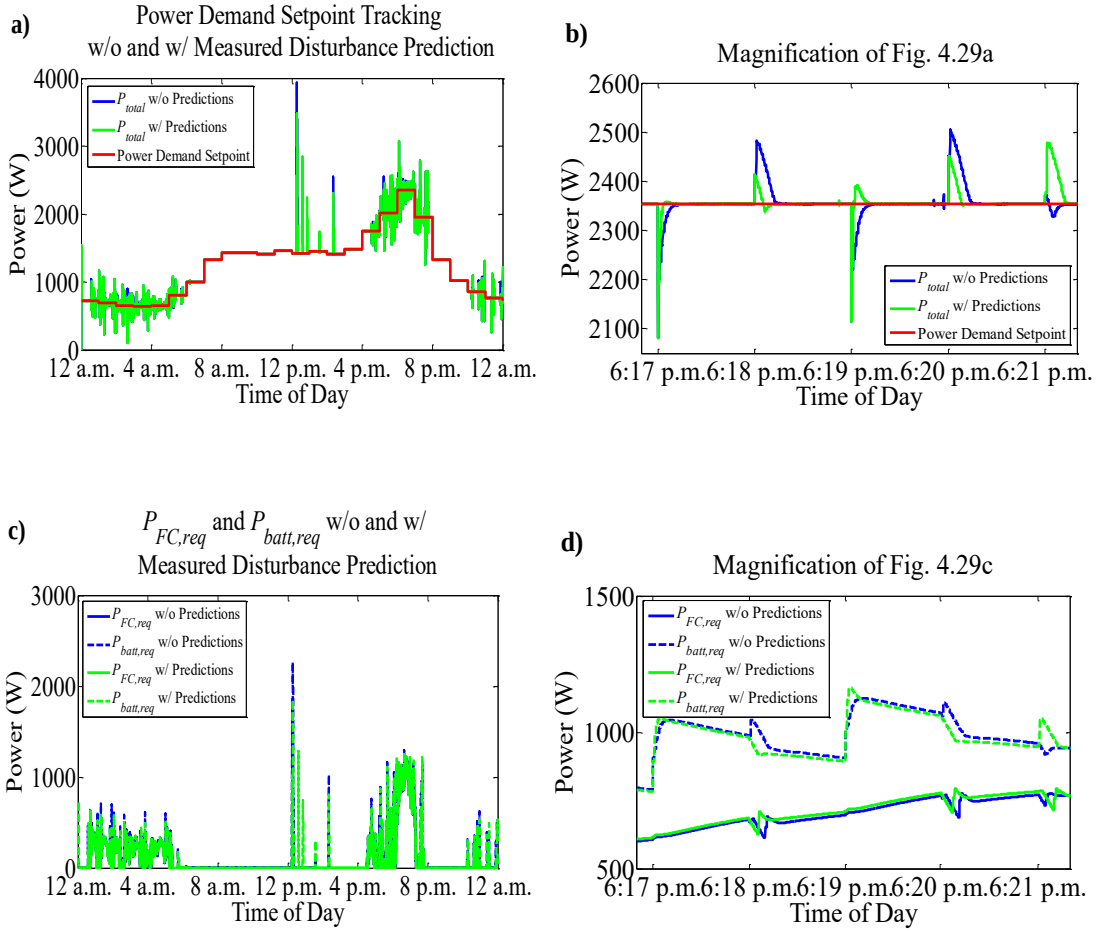

Figure 4.29 **a)** Total power demand setpoint tracking during a 24-hour simulation of the PV/WT/FC/battery/electrolyzer HRES operation with and without measured disturbance prediction; **b)** a magnification of **a)** from 6:17 p.m. to 6:21 p.m.; **c)** requested fuel cell power (P_{FC}^{req}) and battery power (P_{batt}^{req}) during the simulated HRES operation; **d)** a magnification of **c)** from 6:17 p.m. to 6:21 p.m.

The storage capacity setpoint tracking for the battery (SOC_d = 65%) and hydrogen tanks ($L_{H_2,d}$ = 100%), shown in Fig. 4.30a and magnified in Fig. 4.30b, was acceptable given the inconsistent availability of P_{excess}. When P_{excess} was not available, there were no noticeable differences between storage capacity setpoint

tracking with or without measured disturbance prediction because, in each of these cases, there were only minor differences between P_{FC}^{req} and P_{batt}^{req}. When P_{excess} was available, storage capacity setpoint tracking was still not significantly affected by the addition of measured disturbance prediction because P_{elec} and P_{batt}^{ch} are only dependent on P_{excess}, their equal weighting in the MPC strategy, and their respective constraints (Table 4.6). Fig. 4.30c shows that when P_{excess} was available, P_{elec} and P_{batt}^{ch} were equal for most of the 24-hour period and only differed when SOC_m = SOC_d is achieved (from ~10:00am to ~7:00p.m. and from ~8:00 p.m. to ~12:00 a.m.) and when $P_{elec,max}$ is reached (intermittently from ~10:00 a.m. to ~4:00 p.m. and from ~8:00 p.m. to ~10:00 p.m.).

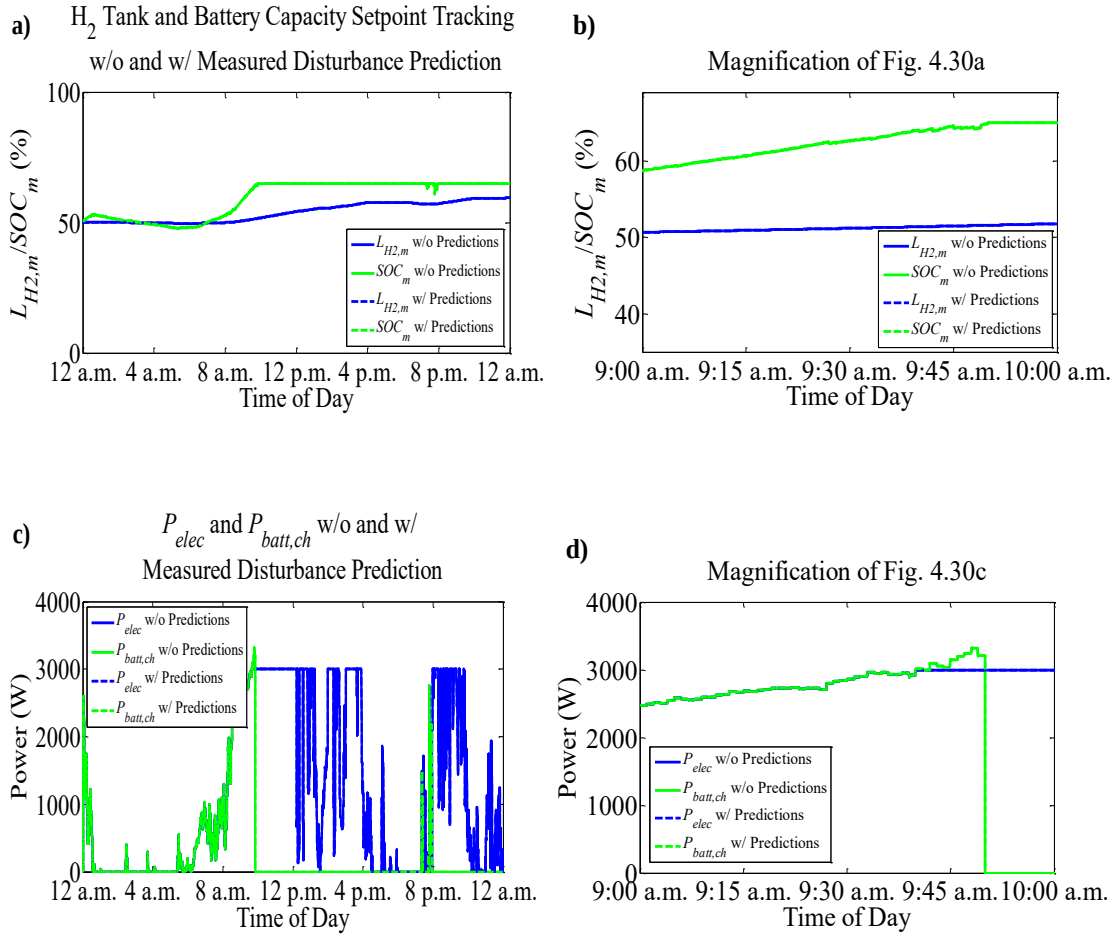

Figure 4.30 **a)** Storage capacity setpoint tracking during a 24-hour simulation of the PV/WT/FC/battery/electrolyzer HRES operation; **b)** a magnification of **a)** from 9:00 a.m. to 10:00 a.m.; **c)** Power delivered to the electrolyzer (P_{elec}) and battery (P_{batt}^{ch}) during the simulated HRES operation; **d)** a magnification of **c)** from 9:00 a.m. to 10:00 a.m.

4.3.5.2.2 Model Adaptation

The MPC's linear state-space model of the non-linear, time-variant HRES was updated using the subspace identification method described in Section 4.3.4.3. Fig. 4.31 shows a comparison between having only measured disturbance prediction and the effect of combined measured disturbance prediction and model adaptation on the

HRES's ability to track the power demand setpoint over the prescribed 24-hour period. For this scenario, it is clear that model adaptation did not provide any practical improvement in power demand setpoint tracking. This is because the FC and battery each output ~500 W to ~1000 W of power, and at such low power outputs each of these systems have an approximately linear relationship with their respective inputs.

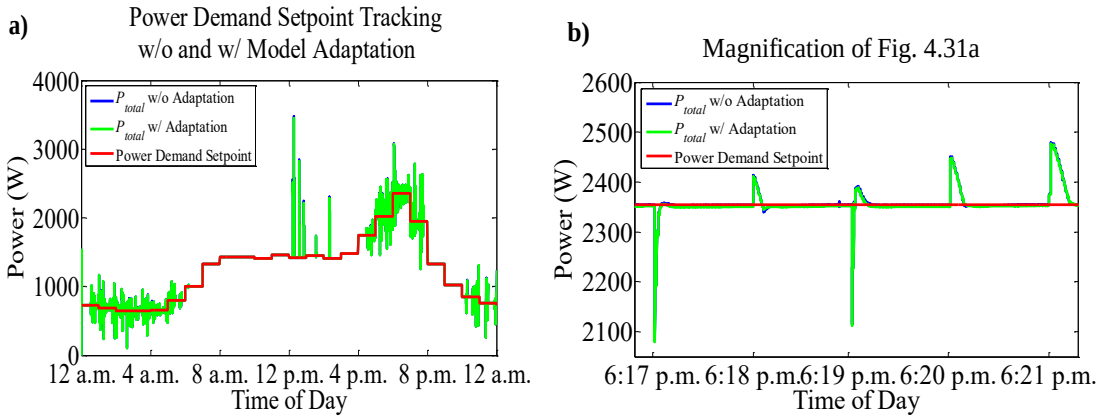

Figure 4.31 **a)** Total power demand setpoint tracking during a 24-hour simulation of the PV/WT/FC/battery/electrolyzer HRES operation with and without model adaptation; and **b)** a magnification of **a)** from 6:17 p.m. to 6:21 p.m.

However, if the FC catalyst activity degrades by 40% after continues use (i.e., the FC catalyst active area decreases by 40%), the non-linear relationship between FC power output and hydrogen flowrate becomes significant, especially at higher power outputs (Fig. 4.32). Because the non-linear FC relationship becomes more prominent, we expect model adaptation to improve the control performance significantly following substantial catalyst degradation.

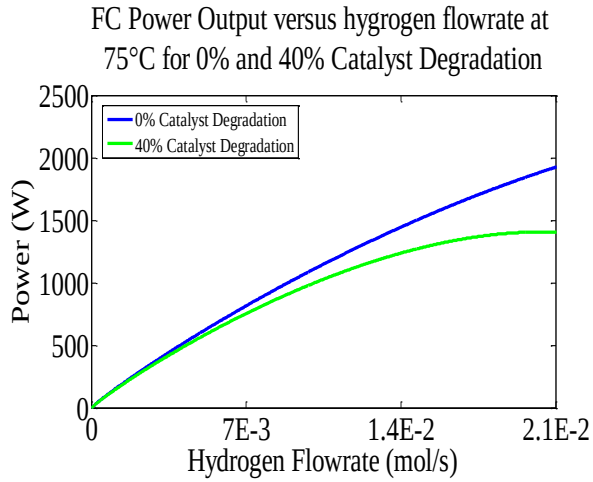

Figure 4.32 Fuel cell power output at 75°C as a function of hydrogen flowrate for 0% catalyst degradation (blue line) and 40% catalyst degradation (green line).

As an example of such a case, consider a hypothetical situation where the power demand profile is that shown in Fig. 4.33, $P_{PV} + P_{WT} = 0$, and 40% of the FC catalyst has degraded. Fig. 4.34 shows the results of simulating the HRES operation under these conditions. Power demand setpoint tracking is nearly identical until the final step increase in power demand from 2000 W to 5000 W (Fig. 4.34a). During the final step increase in power demand, notice that there is much less overshoot of the power demand setpoint when model adaptation was used (Fig. 4.34b), which results in increased HRES efficiency and reduced energy consumption. The advantage of model adaptation becomes apparent because P_{batt}^{req} reaches its upper constraint of 3660 W and the remaining 1340 W of power demand must be met by the FC, forcing P_{FC}^{req} much closer to the FC maximum power output (Fig. 4.34c). As a result, the fuel cell power output was forced into a significantly non-linear operating region where model adaptation was beneficial.

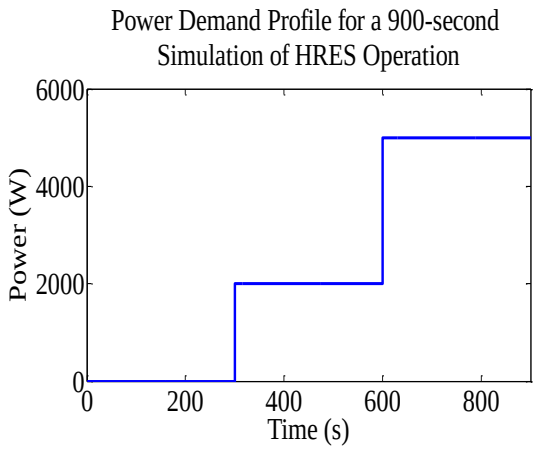

Figure 4.23 Hypothetical 900-second power demand profile used to observe the advantage of incorporating model adaptation into the MPC framework.

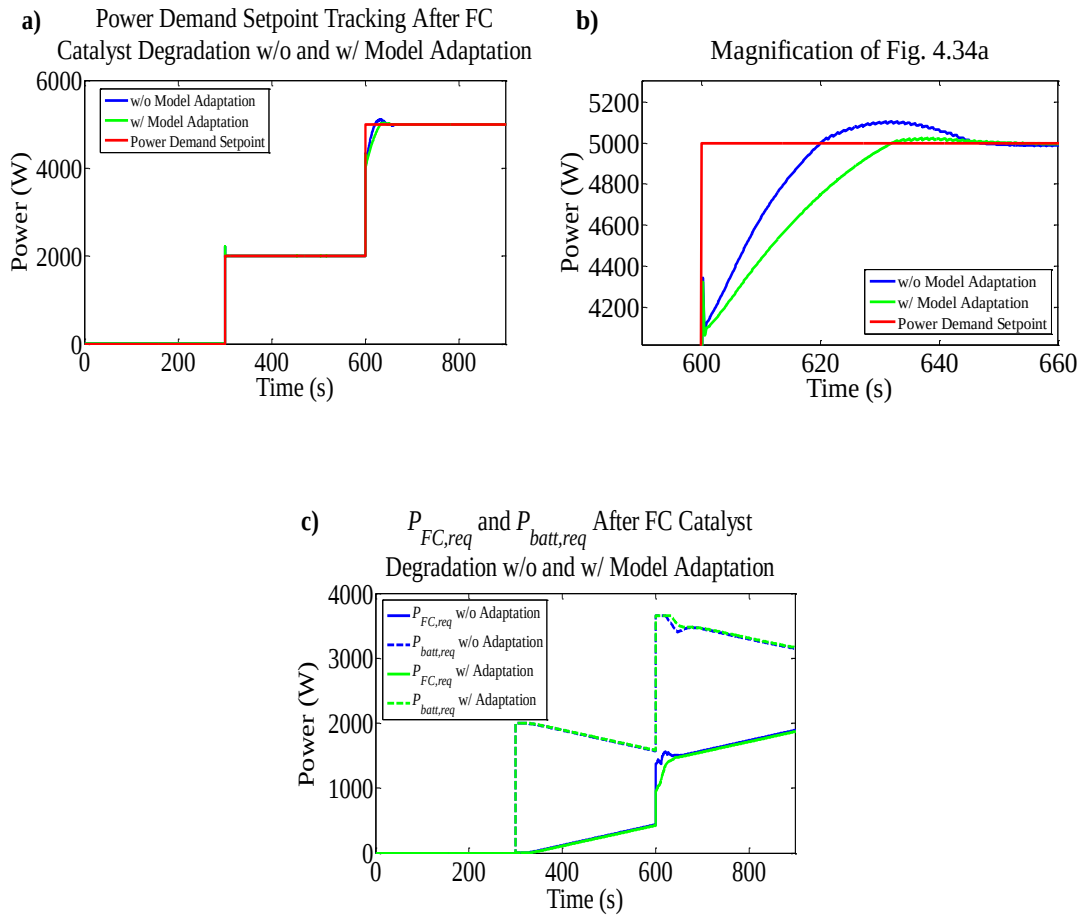

Figure 4.24 **a)** Total power demand setpoint tracking during a 900-second simulation of the PV/WT/FC/battery/electrolyzer HRES operation after FC catalyst degradation with and without model adaptation; **b)** a magnification of **a)** from 590 s to 660 s; and **c)** FC and battery power output during the simulated HRES operation with and without model adaptation.

4.4 Chapter Summary and Conclusions

This Chapter established a HRES advanced control principle, which states that "*Information-rich data should be used to assist in the intelligent coordination of HRES components in meeting its operating objectives when additional computation can be afforded and significant benefits can be realized.*" This principle can be applied

to both decentralized control (e.g., PID control) and centralized control (e.g., MPC) of various systems, as we have shown using two separate case studies.

In the first case study, we present an online procedure for determining a control loop configuration (CLC) in decentralized control schemes that minimizes control loop interactions of a process using collected process data. The procedure first requires adding white Gaussian noise to each process input and output and subsequently fitting collected process data to a structural vector autoregressive (SVAR) time-series model. Next, the SVAR model coefficients are used to estimate connection strength between process variables. In turn, these connection strength estimates are used to obtain the interaction factor of each process output. Finally, in descending value of interaction factor, each process output is paired one at a time with an unpaired process input corresponding to the highest connection strength of the process output under consideration. The pairing procedure continues until no further input-output control loop pairs can be generated.

The procedure was evaluated using a simulated 3-input, 3-output stirred mixing tank process under changing operating conditions. We found that after changing the desired liquid temperature from 30°C to 51°C control system performance degraded as a consequence of having a fixed CLC and controller tuning. Our procedure was able to correctly identify the most appropriate CLC of the simulated stirred mixing tank at the new desired liquid temperature using collected process data. After reconfiguring to the new CLC and retuning the controllers, the simulated stirred mixing tank control system performance was improved. Such results suggest that our procedure warrants further testing on the Tennessee-Eastman process, a simulation process used to benchmark novel control schemes. If proven successful,

our procedure can then be used for actual processes that typically employ decentralized multivariable control schemes.

In the second case study, we presented a novel data-driven MPC framework designed to meet the operating objectives of an off-grid PV/WT/FC/battery/electrolyzer HRES for a single-family home in Newark, DE. The data-driven MPC framework includes a model predictive controller that is assisted by measured disturbance prediction and model adaptation. Accurate measured disturbance prediction (i.e., prediction of P_{PV} and P_{WT}) was achieved using adaptive ARIMA time-series modeling of G_T and v, which was shown to enable the HRES to track more effectively a typical single-family 24-hour power demand setpoint. Model adaptation was accomplished by updating a linear state-space model of the HRES in the model predictive controller using subspace identification of the closed-loop HRES MV and CV data. Our results indicate that model adaptation for this particular HRES is only advantageous when two conditions are met: 1) the FC is forced to output power close to its maximum rated power output; and 2) after significant catalyst degradation has occurred. When these conditions are met, the relationship between FC power and hydrogen flowrate is significantly non-linear, and model adaptation enables the HRES to better track a power demand setpoint.

Chapter 5

EXPERIMENTAL IMPLEMENTATION OF A DESIGNED HRES

5.1 Introduction

Although Chapters 3 and 4 present convincing results of control strategy design and performance for HRESs, these results are purely computational. Therefore, to reinforce these results, we wish to demonstrate the experimental performance of a real controller designed for a HRES.

The HRES under investigation in this Chapter is called an "OMNi-Charger" (Fig. 5.1). Developed by Heliothermal, the OMNi-Charger is a PV/WT/battery HRES for small-scale (~1 W), self-sufficient remote power applications. The OMNi-Charger is a versatile HRES in that it can be simultaneously augmented with an additional renewable energy system (e.g. piezoelectric devices or tidal energy), and a load demand (e.g., cell phone batteries or light bulbs) using multiple USB connections. For example, the OMNi-Charger can be used as a cell phone charging station in a park supplemented by a piezoelectric walking path, which generates electric power when walked on. The OMNi-Charger can also be used to power a lighted Coast Guard buoy augmented with tidal energy, which generates electric power from the energy of ocean tides.

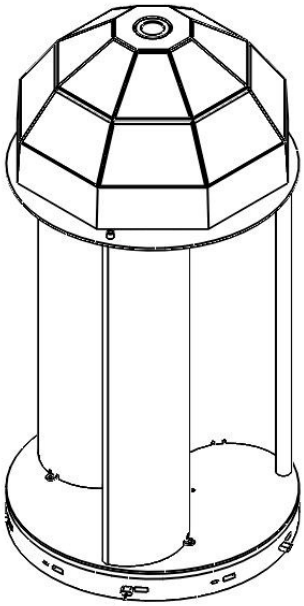

Figure 5.1 Schematic of the initial OMNi-Charger prototype designed by Heliothermal. The device, approximately 2 feet tall, consists of a dome-shaped PV array, a vertical-axis WT, a battery (housed underneath the PV array), and multiple USB ports extruding radially from the base.

Whether augmented with an additional power input or not, the operating objectives of the OMNi-Charger are two-fold: (1) satisfy any power demand instantly; and (2) store any excess charge for later use in the battery. These objectives are challenging to meet in practice primarily because of unexpected changes in PV, WT, or auxiliary power input, which is characterized by capriciously available renewable energy resources (e.g., wind and solar irradiance). Furthermore, potentially frequent changes in cell phone charging or desired light brightness will cause changes in power demand, thus adding more difficulty in meeting the prescribed operating objectives. Because these challenges may be met with appropriately designed control systems, our goal in this Chapter is to design and experimentally evaluate a controller that will

enable the OMNi-Charger to satisfy a power demand while storing any excess power in the battery, in spite of uncontrollable fluctuations in renewable energy resources and power demand.

5.2 OMNi-Charger Description

The OMNi-Charger used during these experiments consists of a PV array, a WT, and a battery (Fig. 5.2). The 3 W-rated monocrystalline silicon PV array provides power from sunlight (P_{PV})[21], while the 3 W-rated vertical-axis savonius WT provides power (P_{WT}) from wind exceeding 3 m/s. The power demand (P_{demand}) is first met using power from either the PV or the WT (P_{input}), whichever is greater. This selection method is used instead of using relatively expensive DC/DC converters to combine P_{PV} and P_{WT}. If there is power remaining after the power demand is satisfied, it is stored in a 42 Wh $LiFePO_4$ battery (P_{batt}^{ch}). Otherwise, power is requested from the battery (P_{batt}^{req}) to meet the remaining power demand.

[21] The PV array used in this work has a flat panel, but a fully-functioning OMNi-Charger will use a half truncated icosahedron-shaped (i.e., dome-shaped) PV array.

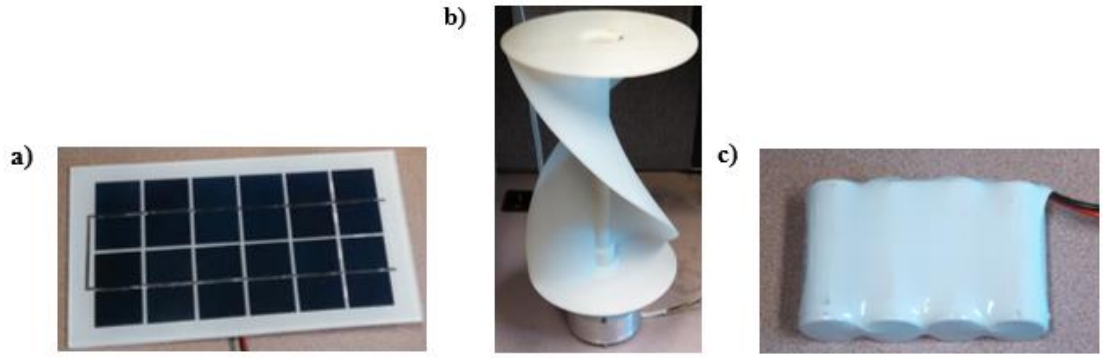

Figure 5.2 Photographs of the OMNi-Charger components: **a)** the PV; **b)** the WT; and **c)** the battery.

5.3 Controller Development

The control objectives of the OMNi-Charger are to satisfy the required power demand and store any excess power in the battery. Battery SOC maintenance (As discussed for the NiCd battery in Chapter 3) is not an operating objective for this system for two reasons: 1) $LiFePO_4$ battery lifetime does not significantly degrade if a specific SOC is not maintained; and 2) given the desired end-use of the OMNi-Charger (self-sufficient remote power applications) we only want the battery to remain as fully charged as possible. Therefore, the only control variable (CV) for this system is the battery discharge power (P_{batt}^{dis}), while the only available manipulated variables (MV) is a signal requesting battery power (P_{batt}^{req}). The disturbance variables (DVs) in this system, which affect the CVs but cannot be manipulated, are P_{PV} and P_{WT}.

The objective of the control strategy design is to use the MV to drive the CV to its desired setpoint despite any uncontrollable fluctuations in the DVs. A control block diagram of the OMNi-Charger system is provided in Fig. 5.3. The OMNi-Charger controller board, shown in Fig. 5.4, is responsible for meeting the control objectives of the system by managing the flow of power between different OMNi-Charger

components as described in Section 5.2. The primary components of the control board consist of auxiliary (e.g., piezoelectric or hydroelectric power), PV, WT, battery, and power demand input sockets and an LTC®4020 power manager.

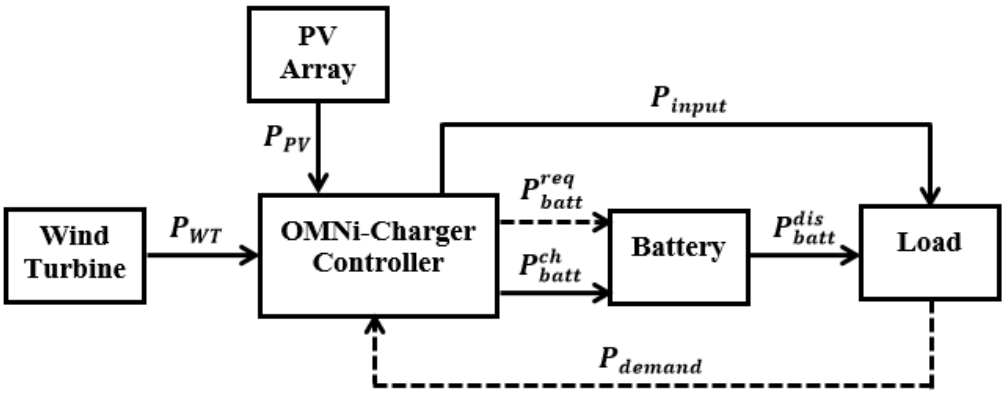

Figure 5.3 OMNi-Charger control block diagram. Solid black lines represent the flow of power while dashed black lines represent flow of information

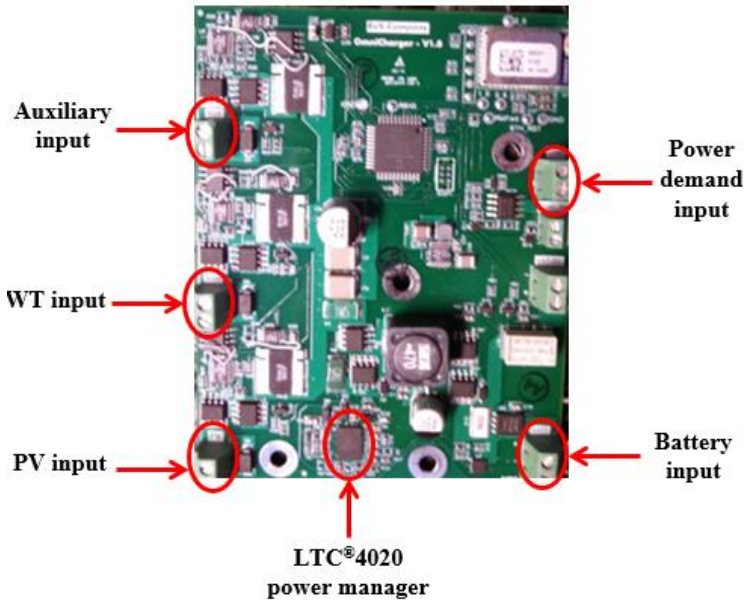

Figure 5.4 Photograph of the OMNi-Charger controller. The location of the LTC®4020 power manager and the PV, WT, battery, power demand, and auxiliary inputs are all indicated above.

The LTC®4020 power manager has three responsibilities. First, it is used for PV array MPPT by maintaining the PV array output voltage at ~6.5 V. Although this simple constant voltage MPPT method is currently used, a more sophisticated perturb and observe method, which will likely outperform the constant voltage method [30], may be implemented in future versions of the OMNi-Charger. Second, the LTC®4020 power manager is used as the battery charge controller and matches the voltage of P_{input} to a nominal value for the battery when the battery is being charged. The battery voltage is typically 13.3 V, but can vary depending on the battery charge state (either precondition, float, or recharge). Finally, the LTC®4020 power manager behaves as the overall state controller that dictates where and how power is directed based on the system state. The state controller logic flowchart along with the control

action for each controller state is provided in Fig. 5.5. When states 1 or 3 occur (i.e., when the battery is needed to meet the power demand unmet by P_{PV} or P_{WT}), the controller requests power from the battery as follows:

$$P_{batt}^{req} = P_{demand} - P_{input}. \tag{5.1}$$

When states 2 or 4 occur (i.e., when P_{PV} or P_{WT} are in excess of P_{demand}) the excess power is stored in the battery:

$$P_{batt}^{ch} = P_{input} - P_{demand}. \tag{5.2}$$

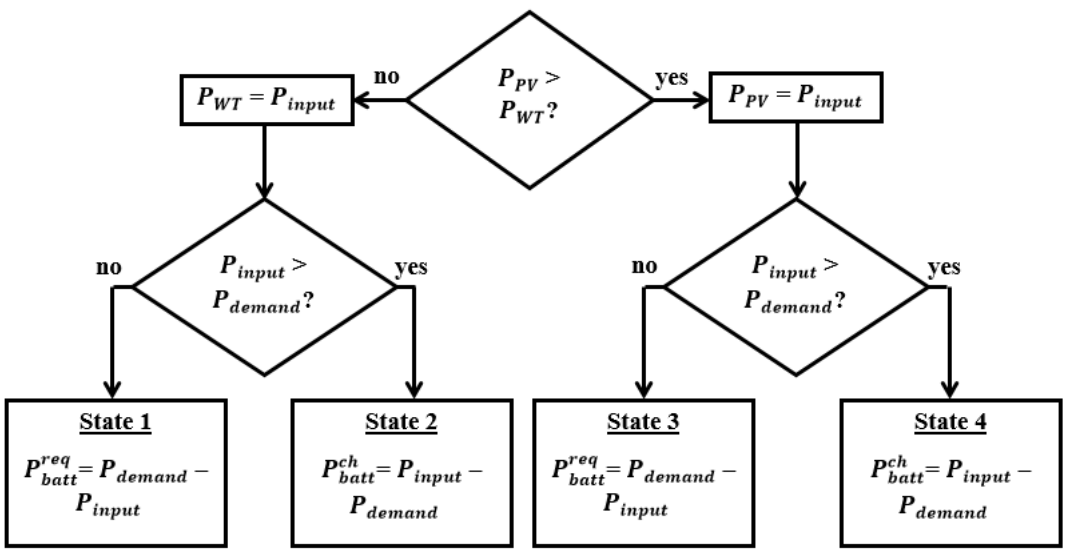

Figure 5.5 Logic flowchart used for state control in the OMNi-Charger controller. For each of the four states, there is a pre-defined control action that occurs when the state is observed.

5.4 Power Data Acquisition

In order to evaluate the OMNi-Charger controller performance under various conditions, it is necessary to collect power data from the PV, WT, battery, and the load. Power data from each input were acquired and stored using two separate Rigol®

DS1054Z oscilloscopes—one responsible for obtaining voltage data and another for collecting current data. Four separate RP2200 passive oscilloscope probes were used to measure the voltage across each positive and negative terminal, while another four Cal Test® CT2593-2 differential oscilloscope probes were used to measure the voltage across a 1 Ω resistor placed in series with the positive terminal of each input. The differential oscilloscope probes, therefore, produce a measurement of the current of each input. The power is then simply the voltage multiplied by the current.

5.5 Controller Evaluation

5.5.1 Controlled Experiments

The OMNi-Charger controller performance was first evaluated under ideal conditions by using two controlled levels (high and low) of three factors (P_{demand}, G_T, and v). Table 5.1 lists the physical interpretations of low and high levels for each factor, which were obtained from various testing equipment. The low and high P_{demand} were produced using a 0.25 W light-emitting diode (LED) bulb and a 1 W LED bulb, respectively (Fig. 5.6). The high level of G_T (1000 W/m^2) was imitated using a Sylvania 1000 W high intensity discharge (HID) metal halide lamp placed 20 inches from the PV array (Fig. 5.7), while a low level of G_T (250 W/m^2) was imitated by placing a 3 mm thick wire mesh attenuation screen 6 inches in front of the PV array while the HID lamp was in use. The high level of v (6 m/s) was produced using a Global Industrial 24-inch portable tilt blower fan on a “high” setting. The fan was tilted upwards by 20° with the WT placed 7 inches above the ground and 9 inches left of the center of the blower fan (Fig. 5.8).

Table 5.1 Design of experiments (DoEs) for controlled testing of the OMNi-Charger Controller. A plus sign indicates a high level of the listed factor while a minus sign indicates a low level. Dynamic DoEs have one changing factor indicated by arrows (DoEs 9-20).

Factor	Low level (-)	High level (+)
P_{demand}	0.25 W	1 W
G_T	250 W/m^2	1000 W/m^2
v	0 m/s	6 m/s

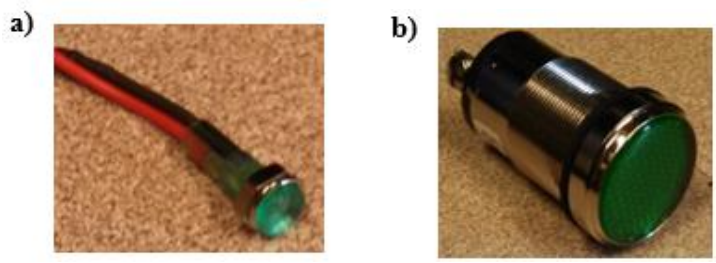

Figure 5.6 Images of the LED used for low and high levels of P_{demand}: **a)** 0.25 W LED bulb and **b)** a 1 W LED bulb.

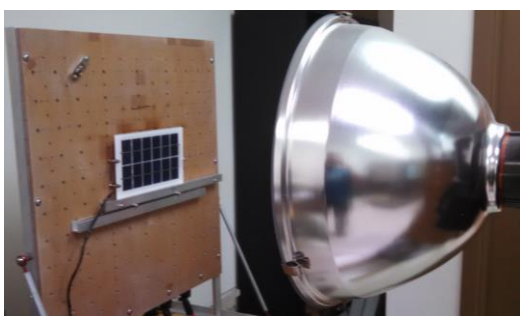

Figure 5.7 Image of the 1000 W HID lamp and PV array mounting apparatus used to produce low and high levels of G_T.

Figure 5.8 Image of the 24-inch blower fan and WT placement used to imitate the high level of wind speed (6 m/s).

To observe the controller performance only within a single state, a 2^3 factorial design of experiments (DoEs) were completed with each level remaining constant. Each of these static experiments consists of all possible combinations of high and low levels of P_{demand}, G_T, and v (8 total experiments). To observe the controller performance when changes between states occur, 3 separate 2^2 factorial DoEs (12 total experiments) were also completed, with each of these experiments having a single dynamic factor and two constant factors. All static and dynamic experiments are listed in Table 5.2.

Table 5.2 Design of experiments (DoEs) for controlled testing of the OMNi-Charger Controller. A plus sign indicates a high level of the listed factor while a minus sign indicates a low level. Dynamic DoEs have one changing factor indicated by arrows (DoEs 9-20).

DoE number	P_{demand}	G_T	v
1	+	+	+
2	-	+	+
3	+	+	-

4	-	+	-
5	+	-	+
6	-	-	+
7	+	-	-
8	-	-	-
9	+	+ → -, - → +	+
10	-	+ → -, - → +	+
11	+	+ → -, - → +	-
12	-	+ → -, - → +	-
13	+	+	+ → -, - → +
14	-	+	+ → -, - → +
15	+	-	+ → -, - → +
16	-	-	+ → -, - → +
17	+ → 0, 0 → -	+	+
18	+ → 0, 0 → -	+	-
19	+ → 0, 0 → -	-	+
20	+ → 0, 0 → -	-	-

The results of two static experiments (DoE 1 and DoE 7) and two dynamic experiments (DoE 9 and DoE 19) are provided in Fig. 5.9, with the remaining static and dynamic DoE results provided in Appendix C. During DoE 1 (Fig. 5.9a), it is clear that the OMNi-Charger is in state 4 (see Fig. 5.4) because P_{PV} (cyan) > P_{demand} (green) > P_{WT} (red). Thus, P_{PV} is selected as P_{input} and the excess power is used to charge the battery (blue) while P_{demand} is satisfied completely. The battery charging (indicated by a negative value of P_{batt}) was not 100% efficient due to inefficiencies within the circuit board (primarily the LTC®4020 power manager), but otherwise the controller behaved as it was designed. The desired controller behavior was also attained for DoE 7 (Fig. 5.9b), where the OMNi-Charger was in state 3 because $P_{demand} > P_{PV} > P_{WT}$. During this state, P_{PV} is again selected as P_{input}, but the battery must now discharge enough power (indicated by a positive value of P_{batt}) to meet the remaining power demand unmet by P_{PV}. Successful controller performance can also

be observed for DoE 9, where the OMNi-Charger transitions from state 4 to state 1 ($P_{demand} > P_{WT} > P_{PV}$) after placing the attenuation screen in front of the HID lamp at 20 seconds, and switches back to state 4 after removing the attenuation screen at 50 seconds (Fig. 5.9c). Throughout this experiment, the correct corresponding control action was completed at each state and between states; first, the battery was charged using excess P_{PV}, then the battery was discharged to meet the remaining power demand unmet by P_{WT}, and once again the battery was charged with excess P_{PV}. Additionally, we can also observe that the controller performed as expected during DoE 19 (Fig. 5.9d). During this experiment, the OMNI-Charger transitions from state 1 to state 2 ($P_{WT} > P_{PV} > P_{demand}$) at 20 seconds after removing the 1 W LED bulb, and remains in state 2 after adding the 0.25 W LED bulb at 40 seconds. During the transition from state 1 to state 2 at 20 seconds, notice that the controller seamlessly dictates a required change between discharging and charging the battery.

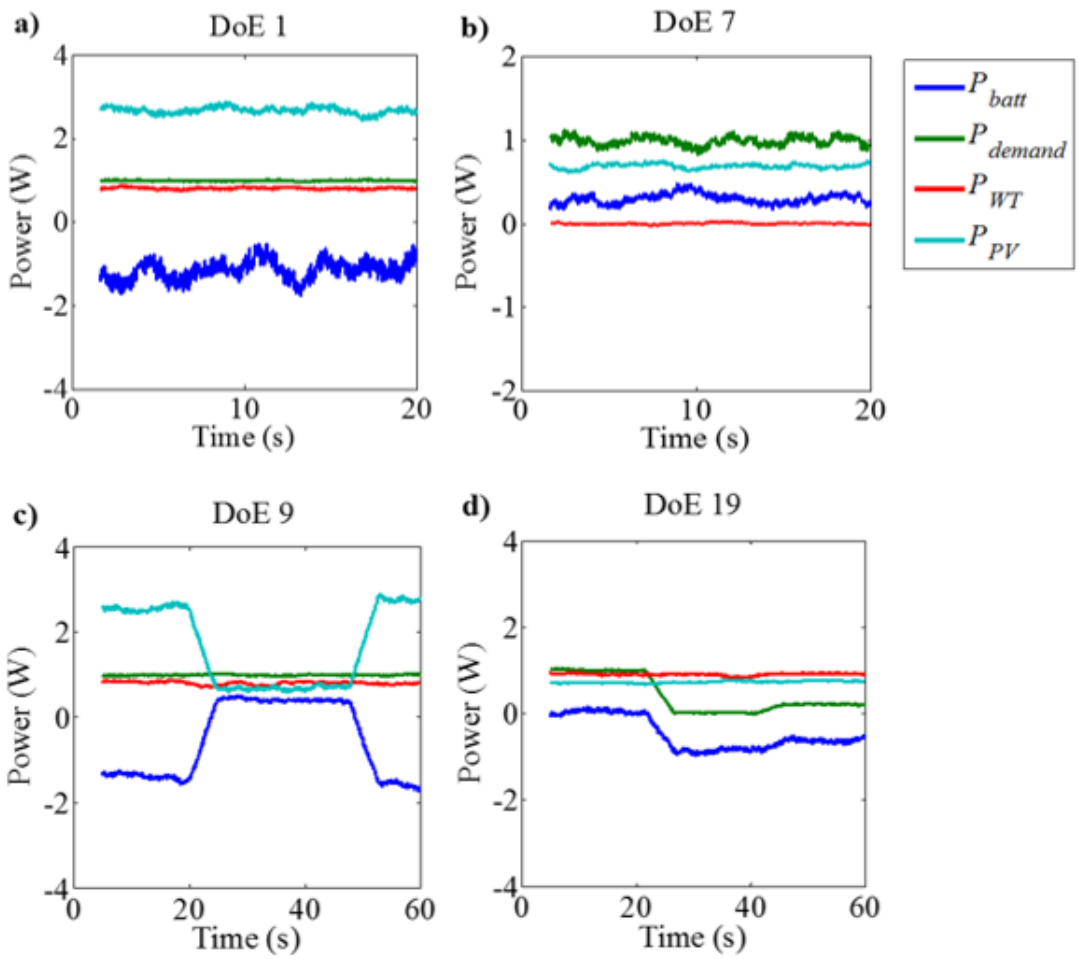

Figure 5.9 One hundred sample time averaged power profiles resulting from **a)** DoE 1, **b)** DoE 7, **c)** DoE 9, and **d)** DoE 19. Figs. **a)** and **b)** are 20-second static profiles, while Figs. **c)** and **d)** are 60-second dynamic profiles. In Fig. **c)**, solar irradiance is changed from a high level to a low level at 20 seconds and back to a high level at 50 seconds. In Fig. **d)**, the power demand is changed from a high level to zero at 20 seconds, then to a low level at 40 seconds. During each DoE, the controller enabled the system to satisfy required power demands and store excess energy in the battery.

5.5.2 Field Testing

To observe the OMNi-Charger controller performance under real conditions, the OMNi-Charger was subject to naturally-occurring levels of G_T from 2:30 p.m.to

3:30 p.m. on April 16th, 2015 on the Green Roof of Colburn Laboratory at the University of Delaware. The solar irradiance was measured at 10-second intervals during the test using an Apogee MP-100 pyranometer. The pyranometer sensor was placed perpendicular to the PV array, which itself was fixed at a 35° incline facing directly south (Fig. 5.10). At 3 p.m., the LED light was changed from the 0.25 W bulb to the 1 W bulb (i.e., P_{demand} was changed from the low to high level). Because the wind was often below the WT cut-in wind speed (3 m/s), v was maintained at its high level using the high-speed drum fan (same orientation as in Fig. 5.7), with ambient wind speed occasionally contributing contributed towards powering the WT. The wind speed was collected at 2-second intervals using a Digi-Sense data logging vane anemometer placed directly between the blower fan and the WT.

Figs. 5.10a - 5.10c provide the solar irradiance profile, wind speed profile, and OMNi-Charger power responses recorded during the 60-minute field test, respectively. During the first 30 minutes of the field test, the system is almost always in state 4, where the controller diverts P_{PV} first towards the power demand and any excess power to charging the battery. Notice how rapid changes in solar irradiance drive the amount of power used to charge the battery while the power demand is satisfied consistently at 0.25 W. After P_{demand} was changed from its low to high level at 30 minutes, some could cover occurred and P_{PV} reduced from ~1.5 W to ~1 W. As a result, the battery observed a consistent switching between state 4 and state 3, depending on the amount of P_{PV} available. Nevertheless, the power demand was met reasonably well at 1 W during the final 30 minutes of the field test.

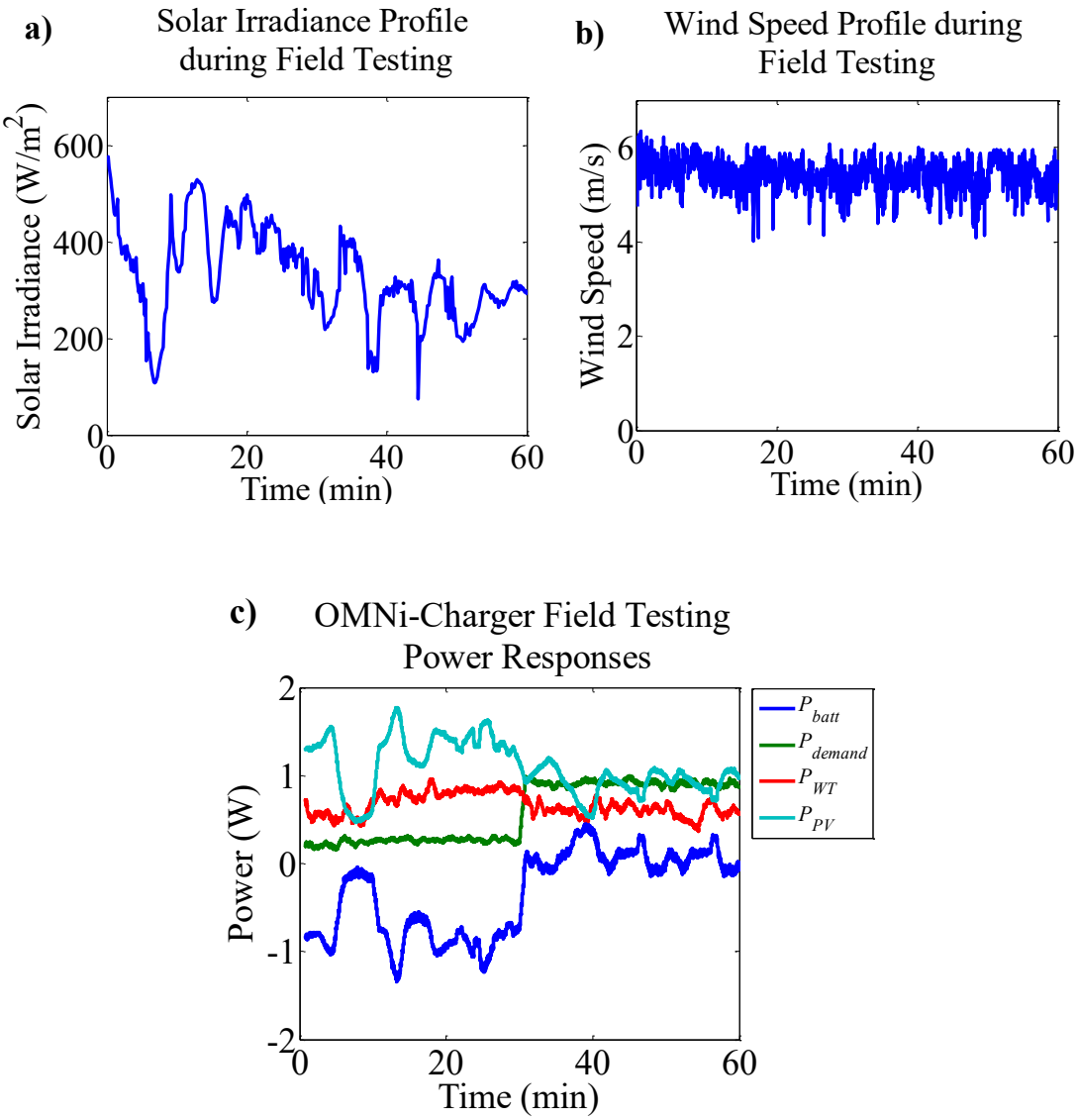

Figure 5.10 OMNi-Charger field testing results completed from 2:30 p.m. to 3:30 p.m. on April 16th, 2015 on the Green Roof of Colburn Laboratory in Newark, DE : **a)** solar irradiance profile; **b)** wind speed profile; and **c)** power responses. Throughout the 60-minute experiment, power demands (low and high) appear to be satisfied mostly by the PV array, with excess energy being stored effectively in the battery.

5.6 Chapter Summary and Conclusions

This Chapter presents a description and evaluation of an experimental PV/WT/battery HRES called an OMNi-Charger. Power management in the OMNi-Charger is accomplished using a simple state controller that dictates the flow of power in the device based on instantaneous measurements of PV and WT power. The OMNi-Charger controller's ability to meet a required power demand and store any excess power in the battery was first evaluated under static and dynamic levels of controlled conditions (namely, solar irradiance, wind speed, and power demand) and then under real environmental conditions. We found that under controlled and real conditions, the OMNi-Charger controller performed adequately, recognizing the state the system was experiencing and completing the desired control action in a timely manner. It is important to note that even when rapid changes between states occurred during the controlled tests and field test, the controller was still capable of meeting the required power demand and storing excess power in the battery. Although the OMNi-Charger controller performance was satisfactory, we recommend that the controller be improved by being augmented with DC/DC converters such that PV and WT power can be utilized simultaneously.

Chapter 6

DISSERTATION CONCLUSIONS AND FUTURE WORK

6.1 Dissertation Conclusions

Low-emission and affordable renewable energy systems are needed to meet a rapidly growing global energy demand without producing greenhouse gases or further diminishing the availability of non-renewable resources. Here, we are specifically concerned with the design, operation, and control of hybrid renewable energy systems (HRESs)—systems consisting of two or more renewable energy systems utilized simultaneously to meet an energy demand. The work presented in this dissertation was completed with the intention of establishing the principles governing the design, operation, and control of HRESs that will result in cost-effective and reliable energy solutions for stationary and mobile applications. The literature on this subject, although useful, is sporadic and lacks a single, systematic study that addresses each of the following research questions:

1. *How should HRES components and their sizes be selected to meet specified operating objectives?*
2. *How should HRESs be designed to meet the operating objectives consistently?*
3. *What types of control strategies are best for meeting a HRES's operating objectives?*
4. *Can data collected from a HRES be used to meet its operating objectives more effectively?*

The first principle presented in this dissertation, presented in Chapter 2, conveys an answer to the first research question:

Principle 1: *HRES components and their sizes should be rationally selected using knowledge of component costs, availability of renewable energy resources, and expected power demands of the application.*

To establish principle 1, we used an economic and feasibility analysis software called HOMER to ascertain the economically optimal HRES types and sizes for a range of possible wind speed, solar irradiance, minimum renewable fraction, and power demand. Under some conditions, we found that after obeying principle 1, HRESs are cost-competitive to stand-alone renewable energy systems and grid-supplied energy. Having shown that HRESs can have a financial advantage over traditional, non-renewable energy is the first step in widespread implementation of clean and affordable renewable energy.

The next step is the development of appropriately designed HRESs and their control systems that guarantee reliable and efficient performance in meeting a power demand and storing excess power. These issues are addressed in Chapters 3, where we answer the second and third research questions. These answers led to the development of principles 2 and 3, respectively:

Principle 2: *By default, the components of a HRES should be arranged in parallel for increased efficiency and reliability. However, a series HRES design may be preferred depending on the operational considerations of the HRES components.*

Principle 3: *Choice of control strategy for a HRES (e.g., state control, PID control, or MPC) depends on the dynamics of HRES components, their operational considerations, and the practical limitations of the HRES end-use.*

Principles 2 and 3 were demonstrated by way of a FC/battery bus augmented with a roof-installed PV array (principle 1 was also demonstrated by evaluating the economics of the PV array modification). A series arrangement of the FC and the battery, where the FC is dedicated to maintaining a desired state of charge (SOC) of the battery and the battery meets most of the power demand, was best suited for this system due to the sensitive nature of the battery lifetime to SOC maintenance. The bus' PV array was arranged in parallel with the battery in meeting the power demand, but could be used to charge the battery when in excess of the bus power demand. We found that the bus' operating objectives (satisfying power demand and maintaining a desired battery SOC) were satisfied best under a variety of operating conditions using a PID control strategy. Furthermore, we recommend that the PV array be installed on the bus because the PV array more than pays for itself over the bus' lifetime in Newark, DE.

Although standard control paradigms for HRESs can function reasonably well, HRES reliability and efficiency in meeting its operating objectives can be improved using adaptive control systems driven by informative data. In Chapter 4, we discussed this answer to our fourth research question and formulated the following principle:

Principle 4: *Information-rich data should be used to assist in the intelligent coordination of HRES components in meeting its operating objectives when additional computation can be afforded and significant benefits can be realized.*

Principle 4 was demonstrated using two separate case studies. The first case study shows improved performance in a decentralized control scheme for a stirred mixing tank following reconfiguration of the separate control loops using directed spectral decomposition of collected process data. The second case study signifies enhanced power demand setpoint tracking of a PV/WT/FC/battery HRES for a single-family home using a centralized control strategy (MPC) augmented with measured disturbance prediction and model adaptation. It is important to note that although the data-driven modifications improved control performance in each case study, each incurs a computational cost which must be considered before implementation.

Experimental implementation of a designed HRES is the focus of Chapter 5. In this Chapter, we described a PV/WT/battery HRES called an OMNi-Charger that can be used for small-scale (~1 W) remote power applications. The state controller designed for this system satisfied a required power demand nearly instantaneously regardless of the prevailing environmental conditions (i.e. wind speed and solar irradiance). Our results suggest that the OMNi-Charger, without an auxiliary power input (since this aspect of the controller has not yet been tested), is prepared for its desired end use as a cell phone charging station or as a power source for a lighted ocean buoy.

6.2 Future Work

6.2.1 Other Renewable Energy Systems in HRESs

Despite the extensive work on the design, operation, and control of HRESs presented throughout this dissertation, there are still other types of low-emission renewable energy systems that can be used as HRES components. For example, hydroelectric, tidal, geothermal, and piezoelectric energy systems can harvest capriciously available renewable energy from dams, oceans, the Earth's crust, and physical pressure, respectively. Furthermore, ultracapacitors, flywheels, and compressed air storage can replace the battery to store excess energy and release this energy when needed. When used as part of a HRES, each of these systems have their own advantages that can offset the disadvantages of other HRES components. Likewise, their own nuances that can be mitigated using the system as part of a HRES. Overall, expanding our array of options for hybridization may allow for a potentially superior and more applicable HRES compared to those that can only consist of PVs, WTs, FCs, electrolyzers, and batteries.

6.2.2 Future OMNi-Charger Experiments

In Chapter 5, we presented the results of an extensive set of experiments for the OMNi-Charger. However, further OMNi-Charger testing is needed to ensure completely proper functionality. Future OMNi-Charger testing should be conducted after making at least three modifications to the device. First, DC/DC converters should be added to each energy input such that multiple renewable energy resources can be taken advantage of simultaneously. Despite the additional cost of adding converters and their associated efficiency losses (~10%), we expect that under some conditions the system efficiency will improve overall since multiple renewable energy resources

can be used concurrently. Second, the dome-shaped PV array, once it is constructed appropriately, should be incorporated into the OMNi-Charger system. Doing so will ensure that the system being tested is as similar to the final product as possible. Finally, an auxiliary power input, most likely a piezoelectric device, should be added to the system as a third energy input. This modification will guarantee that the OMNi-Charger controller can manage a third input in addition the PV and WT input.

6.2.3 Demonstration of a Large-scale Experimental HRES

Although the OMNi-Charger represents an inventive breakthrough in renewable energy technology, it is limited in its applicability due to its small size. However, constructing and demonstrating an experimental HRES for large-scale applications would lead to more ubiquitous use of HRESs. We propose that a large-scale HRES could be implemented at the University of Delaware using the 1.5 MW WT (located at the Lewes Campus in Lewes, DE) in combination with a PV array, a Bloom Energy® SOFC (manufactured in Newark, DE), a battery (an array of Tesla® Power Walls), and an electrolyzer. Because this a PV/WT/FC/battery/electrolyzer HRES contains components with difficult dynamics (e.g., dead times and large transient responses), such a system would likely benefit from a modification of the data-driven MPC strategy proposed in Section 4.3.

REFERENCES

1. Conti, J. J.; Holtberg, P. D.; Beamon, J. A.; Napolitano, S. A.; Schaal, M. A.; Turnure, J. T.; Westfall, L. D. *International Energy Outlook 2013*; Washington D.C., 2013.

2. Conti, J. J.; Holtberg, P. D.; Diefenderfer, J. R.; Napolitano, S. A.; Schaal, M. A.; Turnure, J. T.; Westfall, L. D. *Annual Energy Outlook 2014*; Washington, D.C., 2014.

3. Hable, V. Analysis And Price Projection Of The Uranium Market http://www.marketoracle.co.uk/Article47338.html (accessed Dec 4, 2014).

4. Ramanathan, V.; Feng, Y. Air pollution, greenhouse gases and climate change: Global and regional perspectives. *Atmos. Environ.* **2009**, *43*, 37–50.

5. The Cost of Wind Energy in the U.S. http://www.awea.org/Resources/Content.aspx?ItemNumber=5547 (accessed Mar 31, 2015).

6. Lantz, E.; Hand, M.; Wiser, R. The Past and Future Cost of Wind Energy Preprint. In *2012 World Renewable Energy Forum*; National Renewable Energy Laboratory: Denver, Colorado, 2012; pp. 1–8.

7. Shahan, Z. How Much Do Solar Panels Cost… On My Roof? http://cleantechnica.com/2014/02/04/current-cost-solar-panels/ (accessed Mar 31, 2015).

8. Feldman, D.; Barbose, G.; Margolis, R.; James, T.; Weaver, S.; Darghouth, N.; Fu, R.; Davidson, C.; Booth, S.; Wiser, R. *Photovoltaic System Pricing Trends: Historical, Recent, and Near-Term Projections 2014 Edition*; 2014.

9. Adamson, K.-A. Fuel Cells and the Cost Curve https://www.navigantresearch.com/blog/fuel-cells-and-the-cost-curve (accessed Mar 31, 2015).

10. Givler, T.; Lilienthal, P. *Using HOMER Software, NREL ' s Micropower Optimization Model, to Explore the Role of Gen-sets in Small Solar Power Systems; Case Study : Sri Lanka*; Golden, Colorado, 2005.

11. Hansen, C. J.; Bower, J. An Economic Evaluation of Small-scale Wind-diesel Hybrid Systems in Kachchh, India. In *World Renewable Energy Congress VIII*; Denver, Colorado, 2004.

12. Isherwood, W.; Smith, J. R.; Aceves, S. M.; Berry, G.; Clark, W.; Johnson, R.; Das, D.; Goering, D.; Seifert, R. Remote power systems with advanced storage technologies for Alaskan villages. *Energy* **2000**, *25*, 1005–1020.

13. Kamel, S. The economics of hybrid power systems for sustainable desert agriculture in Egypt. *Energy* **2005**, *30*, 1271–1281.

14. Muslih, I. M.; Abdellatif, Y. N. Hybrid Micro-Power Station; Output Power Analysis, Cost Analysis, and Environmental Impact by using HOMER Modeling Software. In *Computational Intelligence and Bioinformatics / 755: Modelling, Identification, and Simulation*; ACTAPRESS: Calgary,AB,Canada, 2011.

15. Greacen, C.; Prasitpianchai, S.; Suwannakum, T.; Menke, C. *Renewable energy options on islands in the Andaman Sea: hybrid solar/wind/diesel systems*; Chiang Mai, Thailand, 2007.

16. Khan, M. J.; Iqbal, M. T. Pre-feasibility study of stand-alone hybrid energy systems for applications in Newfoundland. *Renew. Energy* **2005**, *30*, 835–854.

17. Nelson, D. B.; Nehrir, M. H.; Wang, C. Unit sizing and cost analysis of stand-alone hybrid wind/PV/fuel cell power generation systems. *Renew. Energy* **2006**, *31*, 1641–1656.

18. Manwell, J. F.; McGowan, J. G.; Rogers, A.; Blanco, G.; Dua, M. *Potential for Wind Energy Development on New England Islands*; Amherst, Massachusetts, 2003.

19. Rehman, S.; El-Amin, I. M.; Ahmad, F.; Shaahid, S. M.; Al-Shehri, A. M.; Bakhashwain, J. M.; Shash, A. Feasibility study of hybrid retrofits to an isolated off-grid diesel power plant. *Renew. Sustain. Energy Rev.* **2007**, *11*, 635–653.

20. Shaahid, S. M.; El-Amin, I.; Rehman, S.; Al-Shehri, A.; Bakashwain, J.; Ahmad, F. Potential of Autonomous/Off-grid Hybrid Wind-Diesel Power System for Electrification of a Remote Settlement in Saudi Arabia. *Wind Eng.* **2004**, *28*, 621–627.

21. Levene, J.; Kroposki, B.; Sverdrup, G. Wind Energy and Production of Hydrogen and Electricity — Opportunities for Renewable Hydrogen. In *2006 POWER-GEN Renewable Energy and Fuels Technical Conference*; IEEE: Las Vegas, NV, 2006.

22. Devine, M.; Manwell, J.; Baring-Gould, E. I.; Petrie, B. *Wind-Diesel Hybrid Options for Remote Villages in Alaska*; Amherst, MA, 2003.

23. Trifkovic, M.; Sheikhzadeh, M.; Nigim, K.; Daoutidis, P. Modeling and Control of a Renewable Hybrid Energy System With Hydrogen Storage. *IEEE Trans. Control Syst. Technol.* **2014**, *22*, 169–179.

24. Wu, W.; Xu, J. P.; Hwang, J. J. Multi-loop nonlinear predictive control scheme for a simplistic hybrid energy system. *Int. J. Hydrogen Energy* **2009**, *34*, 3953–3964.

25. Wang, C. Modeling and control of hybrid wind/photovoltaic/fuel cell distributed generation systems, Montana State University, 2006.

26. Kassem, A. M.; Yousef, A. M. Voltage and frequency control of an autonomous hybrid generation system based on linear model predictive control. *Sustain. Energy Technol. Assessments* **2013**, *4*, 52–61.

27. Torreglosa, J. P.; García, P.; Fernández, L. M.; Jurado, F. Energy dispatching based on predictive controller of an off-grid wind turbine/photovoltaic/hydrogen/battery hybrid system. *Renew. Energy* **2015**, *74*, 326–336.

28. Knier, G. How Do Photovoltaics Work? http://science.nasa.gov/science-news/science-at-nasa/2002/solarcells/ (accessed Apr 6, 2015).

29. Solar Photovoltaics (PV): PV Cell types http://www.b-es.org/sustainability/sustainable-technology-briefing-sheets/solar-pv-guidance/ (accessed Apr 6, 2015).

30. Faranda, R.; Leva, S. Energy comparison of MPPT techniques for PV Systems. *WSEAS Trans. power Syst.* **2008**, *3*, 446–455.

31. Wind Energy http://www.energyland.emsd.gov.hk/en/energy/renewable/wind.html (accessed Apr 6, 2015).

32. AK, S. Wind Energy Market and Wind Turbine Market: Global Industry Size, Share, Trends, Analysis and Forecasts 2011 - 2016 http://www.redorbit.com/news/science/1113173201/wind-energy-market-and-wind-turbine-market-global-industry-size/ (accessed Apr 7, 2015).

33. Dvorak, P. Why not more vertical-axis wind turbines? http://www.windpowerengineering.com/design/vertical-axis-wind-turbines/ (accessed Apr 7, 2015).

34. Islam, M.; Fartaj, A.; Ting, D. S. K. Current utilization and future prospects of emerging renewable energy applications in Canada. *Renew. Sustain. Energy Rev.* 2004, *8*, 493–519.

35. McNiff, B. P.; Errichello, R. L. New guidelines promise reliable wind-turbine gearboxes: What they mandate http://machinedesign.com/sustainable-engineering/new-guidelines-promise-reliable-wind-turbine-gearboxes-what-they-mandate (accessed Apr 6, 2015).

36. Hau, E. *Wind turbines: Fundamentals, technologies, application, economics*; 2nd ed.; Springer Berlin Heidelberg: Berlin, Heidelberg, Germany, 2006.

37. Savino, K. Microstructural Engineering of Hydroxyapatite Membranes for Fuel Cell Applications http://www.optics.rochester.edu/workgroups/cml/opt307/spr09/keith/index.htm (accessed Apr 7, 2015).

38. *The Fuel Cell Industry Review 2013*; London, England, 2013.

39. Rayment, C.; Sherwin, S. *Introduction to Fuel Cell Technology*; Notre Dame, IN, 2003.

40. Suh, K. W. Modeling , Analysis and Control of Fuel Cell Hybrid Power Systems, The University of Michigan, 2006.

41. Rechargable Battery Diagrams http://electrochemsolutions.com/battery/resources.aspx (accessed Apr 9, 2015).

42. Deep Cycle Battery FAQ http://www.solar-electric.com/deep-cycle-battery-faq.html#Starting, Marine, and Deep-Cycle Batteries (accessed Apr 9, 2015).

43. What's the Best Battery? http://batteryuniversity.com/learn/article/whats_the_best_battery (accessed Apr 9, 2015).

44. García-Valverde, R.; Espinosa, N.; Urbina, A. Simple PEM water electrolyser model and experimental validation. *Int. J. Hydrogen Energy* **2012**, *37*, 1927–1938.

45. Carmo, M.; Fritz, D. L.; Mergel, J.; Stolten, D. A comprehensive review on PEM water electrolysis. *Int. J. Hydrogen Energy* **2013**, *38*, 4901–4934.

46. Hydrogen storage http://hydropole.ch/en/hydrogen/storage/ (accessed Apr 10, 2015).

47. Federal Incentives/Policies for Renewables and Efficiency – Residential Renewable Energy Tax Credit http://www.dsireusa.org/incentives/incentive.cfm?Incentive_Code=US37F&re=0&ee=0 (accessed Feb 2, 2015).

48. Delaware Incentives/Policies for Renewables and Efficiency – Delaware Electric Cooperative - Green Energy Program Incentives (SRECs) http://www.dsireusa.org/incentives/incentive.cfm?Incentive_Code=DE20F&re=0&ee=0 (accessed Feb 2, 2015).

49. Operational and Maintenance Costs for Wind Turbines http://www.windmeasurementinternational.com/wind-turbines/om-turbines.php (accessed Apr 23, 2015).

50. Lambert, T.; Gilman, P.; Lilienthal, P. Micropower System Modeling with Homer. In *Integration of Alternative Sources of Energy*; 2006; pp. 379–418.

51. Breakthrough Technologies Institute *2010 Fuel Cell Technologies Market Report*; Golden, CO (United States), 2011.

52. Basi, J.; Farquharson, N. *PEM Fuel Cells Make a Powerful Case for Small Business Backup*; 2014.

53. Mekhilef, S.; Saidur, R.; Safari, a. Comparative study of different fuel cell technologies. *Renew. Sustain. Energy Rev.* **2012**, *16*, 981–989.

54. Kordesch, K. V.; Simader, G. R. Environmental Impact of Fuel Cell Technology. *Chem. Rev.* **1995**, *95*, 191–207.

55. Bubna, P.; Brunner, D.; Gangloff Jr., J. J.; Advani, S. G.; Prasad, A. K. Analysis, operation and maintenance of a fuel cell/battery series-hybrid bus for urban transit applications. *J. Power …* **2010**, *195*, 3939–3949.

56. Divya, K. C.; Østergaard, J. Battery energy storage technology for power systems—An overview. *Electr. Power Syst. Res.* **2009**, *79*, 511–520.

57. Nelson, R. F. Power requirements for batteries in hybrid electric vehicles. *J. Power Sources* **2000**, *91*, 2–26.

58. Bergveld, H. J.; Kruijt, W. S.; Notten, P. H. L. *Battery Management Systems: Design by Modelling*; Toolenaar, F., Ed.; Springer: Eindhoven, The Netherlands, 2002.

59. Duffie, J. A.; Beckman, W. A. *Solar Engineering of Thermal Processes*; 4th ed.; John Wiley & Sons: Hoboken, NJ, United States, 2013.

60. Ro, K.; Rahman, S. Two-loop controller for maximizing performance of a grid-connected photovoltaic-fuel cell hybrid power plant. *IEEE Trans. Energy Convers.* **1998**, *13*, 276–281.

61. Bubna, P. Modeling , Simulation and Optimization of Fuel Cell/Battery Hybrid Powertrains, University of Delaware, 2010.

62. Ogunnaike, B. A.; Ray, W. H. *Process Dynamics, Modeling, and Control*; Oxford University Press: New York, NY, 1994.

63. Bourbon, E. *Clean Cities Alternative Fuel Price Report*; Washington, D.C., 2014.

64. Eudy, L.; Post, M.; Gikakis, C. *Fuel Cell Buses in U. S. Transit Fleets: Current Status 2014*; Golden, CO, 2014.

65. Anderson, C.; Bartholdi, J. J. Centralized versus decentralized control in manufacturing: Lessons from social insects. In *Complexity and Complex Systems in Industry*; The University of Warwick: Warwick, U.K., 2000; pp. 92–105.

66. Bristol, E. On a new measure of interaction for multivariable process control. *IEEE Trans. Automat. Contr.* **1966**, *11*, 133–134.

67. McEvoy, T. J.; Witcher, M. Interacting control systems: steady state and dynamic measurement of interaction. *ISA Trans.* **1977**, *16*, 35–41.

68. Gigi, S.; Tangirala, A. K. Reconstructing Plant Connectivity Using Directed Spectral Decomposition. In *8th IFAC Symposium on Advanced Control of Chemical Processes*; Vinay, K., Ed.; The International Federation of Automatic Control: Furama Riverfront, Singapore, 2012; pp. 481–486.

69. Gigi, S.; Tangirala, A. K. Quantitative analysis of directional strengths in jointly stationary linear multivariate processes. *Biol. Cybern.* **2010**, *103*, 119–133.

70. Lütkepohl, H. *New Introduction to Multiple Time Series Analysis*; Springer Berlin Heidelberg: Berlin, Heidelberg, Germany, 2005.

71. Smith, S. W. *Digital Signal Processing: A Practical Guide for Engineers and Scientists*; Newnes: Burlington, MA, 2003.

72. Gervers, M. R.; Anderson, B. D. O. Representations of jointly stationary stochastic feedback processes. *Int. J. Control* **1981**, *33*, 777–809.

73. *Applied Time Series Econometrics*; Lütkepohl, H.; Krätzig, M., Eds.; Cambridge University Press: Cambridge, 2004.

74. Sharma, J. K. *Business Statistics*; 1st Editio.; Dorling Kindersley Pvt Ltd: Patpargani, Delhi 110 092, India, 2006.

75. Gigi, S. Reconstruction and quantification of interaction pathways in multivariate systems using directed spectral analysis, Indian Institute of Technology, 2013.

76. Theiler, J.; Eubank, S.; Longtin, A.; Galdrikian, B.; Doyne Farmer, J. Testing for nonlinearity in time series: the method of surrogate data. *Phys. D Nonlinear Phenom.* **1992**, *58*, 77–94.

77. Yerramalla, S.; Davari, A.; Feliachi, A.; Biswas, T. Modeling and simulation of the dynamic behavior of a polymer electrolyte membrane fuel cell. *J. Power Sources* **2003**, *124*, 104–113.

78. De Bruijn, F. a.; Dam, V. a. T.; Janssen, G. J. M. Review: Durability and Degradation Issues of PEM Fuel Cell Components. *Fuel Cells* **2008**, *8*, 3–22.

79. Yin, M.; Li, G.; Zhou, M.; Zhao, C. Modeling of the Wind Turbine with a Permanent Magnet Synchronous Generator for Integration. *2007 IEEE Power Eng. Soc. Gen. Meet.* **2007**.

80. Hua, T.; Ahluwalia, R.; Peng, J.-K.; Kromer, M.; Lasher, S.; McKenney, K.; Law, K.; Sinha, J. *Technical Assessment of Compressed Hydrogen Storage Tank Systems for Automotive Applications*; Argonne, Illinois, 2010.

81. Sun, T.; Chen, Z.; Blaabjerg, F. Voltage recovery of grid-connected wind turbines with DFIG after a short-circuit fault. In *PESC Record - IEEE Annual Power Electronics Specialists Conference*; 2004; Vol. 3, pp. 1991–1997.

82. Heier, S. *Grid Integration of Wind Energy Conversion Systems*; 2nd ed.; John Wiley & Sons, 2006.

83. Rolan, A.; Luna, A.; Rocabert, J.; Aguilar, D.; Vazquez, G. An approach to the Performance-Oriented Model of Variable-Speed Wind turbines. In *2010 IEEE International Symposium on Industrial Electronics*; IEEE, 2010; pp. 3853–3858.

84. Yin, M.; Li, G.; Zhou, M.; Zhao, C. Modeling of the Wind Turbine with a Permanent Magnet Synchronous Generator for Integration. In *2007 IEEE Power Engineering Society General Meeting*; IEEE, 2007; pp. 1–6.

85. Bumby, J. R.; Stannard, N.; Martin, R. *A Permanent Magnet Generator for Small Scale Wind Turbines*; Al Majma'ah, Saudi Arabia, 2006.

86. Ouassaid, M.; Cherkaoui, M.; Nejmi, A.; Maaroufi, M. Nonlinear Control of Interior PMSM Using Control Lyapunov Functions. *World Acad. Sci. Eng. Technol.* **2014**, *2*, 17–26.

87. Khan, M. J.; Iqbal, M. T. Modelling and analysis of electrochemical, thermal, and recetant flow dynamics for a PEM fuel cell system. *Fuel Cells* **2005**, *5*, 463–475.

88. Amphlett, J. C.; Baumert, R. M.; Mann, R. F.; Peppley, B. a; Roberge, P. R.; Harris, T. J. Performance Modeling of the Ballard Mark IV Solid Polymer Electrolyte Fuel Cell I. Mechanistic Model Development. *J. Electrochem. Soc.* **1995**, *142*, 1–8.

89. Ceraolo, M. New dynamical models of lead-acid batteries. *IEEE Trans. Power Syst.* **2000**, *15*, 1184–1190.

90. Roy, A.; Watson, S.; Infield, D. Comparison of electrical energy efficiency of atmospheric and high-pressure electrolysers. *Int. J. Hydrogen Energy* **2006**, *31*, 1964–1979.

91. Broom, D. P. *Hydrogen Storage Materials*; Green Energy and Technology; Springer London: London, England, 2011.

92. Schmittinger, W.; Vahidi, A. A review of the main parameters influencing long-term performance and durability of PEM fuel cells. *J. Power Sources* 2008, *180*, 1–14.

93. Reikard, G. Predicting solar radiation at high resolutions: A comparison of time series forecasts. *Sol. Energy* **2009**, *83*, 342–349.

94. Diagne, H. M.; David, M.; Lauret, P.; Boland, J. Solar Irradiation Forecasting : State-of-the-Art and Proposition for Future Developments for Small-scale Insular Grids. In *World Renewable Energy Forum*; American Solar Energy Society: Denver, Colorado, 2012; pp. 1–8.

95. Gomes, P.; Castro, R. Wind Speed and Wind Power Forecasting using Statistical Models : AutoRegressive Moving Average (ARMA) and Artificial Neural Networks (ANN). *Int. J. Sustain. Energy Dev.* **2012**, *1*, 36–45.

96. Kwiatkowski, D.; Phillips, P. C. B.; Schmidt, P.; Shin, Y. Testing the Null Hypothesis of Stationarity Against the Alternative of a Unit Root : How Sure Are We That Economic Time Series Are Nonstationary? *J. Econom.* **1992**, *52*, 159–178.

97. Burnham, K. P.; Anderson, D. R. Multimodel Inference: Understanding AIC and BIC in Model Selection. *Sociol. Methods Res.* **2004**, *33*, 261–304.

98. Hurvich, C. M.; Tsai, C. Regression and Time Series Model Selection in Small Samples. *Biometrika* **1989**, *76*, 297–307.

99. Shono, H. Efficiency of the finite correction of Akaike's Information Criteria. *Fish. Sci.* **2000**, *66*, 608–610.

100. Luo, X.; Song, Y. Adaptive predictive control: A data-driven closed-loop subspace identification approach. *Abstr. Appl. Anal.* **2014**, *2014*.

101. Jansson, M. Subspace Identification and ARX Modeling. In *13th IFAC Symp on System Identification*; Rotterdam, The Netherlands, 2003.

102. Comrey, A. L.; Lee, H. B. *Elementary Statistics: A Problem Solving Approach 4th Edition*; Lulu.com, 2006.

103. Rodríguez, A. G. G.; Rodríguez, A. G.; Payán, M. B. Estimating Wind Turbines Mechanical Constants. In *International Conference on Renewable Energies and Power Quality*; Seville, Spain, 2007.

104. Siracusano, S.; Baglio, V.; Briguglio, N.; Brunaccini, G.; Di Blasi, A.; Stassi, A.; Ornelas, R.; Trifoni, E.; Antonucci, V.; Aricò, A. S. An electrochemical study of a PEM stack for water electrolysis. In *International Journal of Hydrogen Energy*; 2012; Vol. 37, pp. 1939–1946.

Appendix A

PEARSON CORRELATION COEFFICIENT STATISTICAL HYPOTHESIS TEST FOR WHITE NOISE SEQUENCES

A statistical hypothesis test for the Pearson correlation coefficient (ρ) was used in this work to determine if the correlation between two white noise sequences is significantly different from zero. The hypothesis test evaluates the following two-tailed hypotheses:

$$\begin{aligned} H_0&: \rho = 0 \\ H_A&: \rho \neq 0' \end{aligned} \tag{A.1}$$

where H_0 is the null hypothesis that ρ between two white noise sequences is zero and H_A is the alternative hypothesis that ρ between two white noise sequences is different from zero. The hypotheses were evaluated at the 95% significance level using the following test statistic for the Pearson correlation coefficient [102]:

$$t = \rho\sqrt{\frac{N-2}{1-\rho^2}}, \tag{A.2}$$

where t is the t score of ρ and N is the number of elements in each white noise sequence. If the t score is less than the t score critical value at a given confidence level (found in [102]), then there is no evidence to reject H_0 at that confidence level, and the white noise sequences are insignificantly correlated.

Appendix B

DETERMINING APPROPRIATE ARIMA TIME-SERIES MODEL SELECTION CRITERIA, DATA WINDOW SIZE, AND MAXIMUM ALLOWABLE MODEL ORDERS

The appropriate ARIMA time-series model selection criteria (BIC, AIC, or AICc), optimal data window size (N_{ts}^{opt}), and maximum allowable ARIMA model orders (pq_{max}) were needed to ensure that our adaptive ARIMA time-series modeling methodology yielded solar irradiance (G_T) and wind speed (v) predictions having a minimum mean square prediction error (MSPE). This was accomplished by comparing the MSPE of G_T and v for varying model selection criteria, N_{ts}^{opt} from 30 to 240 at 30-sample increments, and pq_{max} (1, 2, and 3).

Fig. B.1 shows the MSPEs of G_T and v for varying model selection criteria, varying N_{ts}^{opt}, and pq_{max} = 3. Observe that the lowest MSPE for G_T is achieved using AICc and N_{ts}^{opt} = 210 (Fig. B.1a), while for v, the lowest MSPE is achieved using the AICc and N_{ts}^{opt} = 180 (Fig. B.1b). The AICc model selection criteria yielded the lowest MSPE, which was expected after reviewing literature that compares model selection criteria [97–99]. There is an optimal N_{ts} because if N_{ts} is too low, predictions are based partially on local variations that may be due to noise, while if N_{ts} is too large, predictions are based on past data characteristics that may not accurately represent present data characteristics.

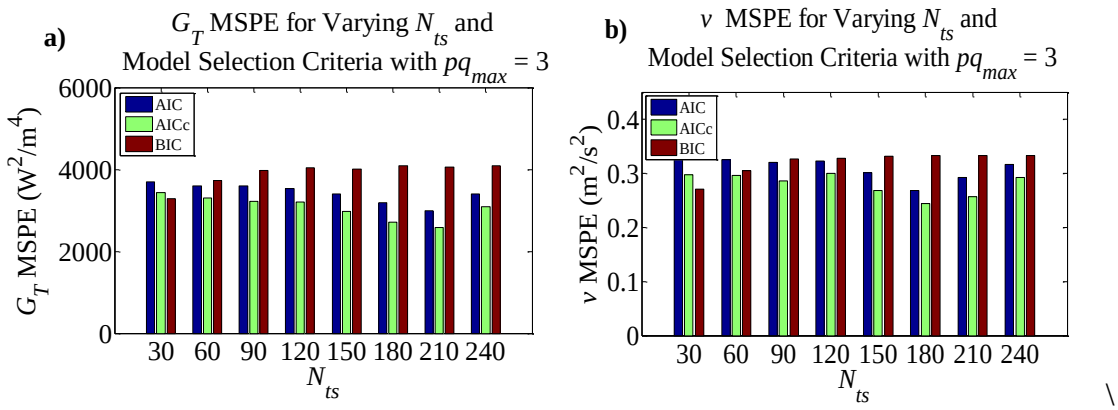

Figure B.1 Mean square prediction error (MSPE) after varying model selection criteria (BIC, AIC, and AICc) and data window size (N_{ts}) with the maximum allowable ARIMA model orders (pq_{max}) fixed to 3 for **a)** Solar irradiance (G_T); and **b)** wind speed (v). The best model selection criteria for G_T and v ARIMA predictive models is AICc, and the optimal data window size is 210 and 180 for G_T and v, respectively.

Fig. B.2 shows the MSPEs of G_T (Fig. B.2a) and v (Fig. B.2b) for varying N_{ts}^{opt}, varying pq_{max}, and using the AICc model selection criteria. Setting pq_{max} = 3 results in the lowest MSPE for both G_T and v. If pq_{max} < 3, the MSPE increases because having fewer allowable model orders can result in an under-fit ARIMA model. When a model is under-fit to data, not all characteristics of the data are captured by the model, and predictions based on an under-fitted model can therefore be less accurate. If pq_{max} > 3, we expect only a slightly lower MSPE with an exponentially increasing computational cost, which may lead to sluggish predictions. Hence, we only consider up to pq_{max} = 3 in this work.

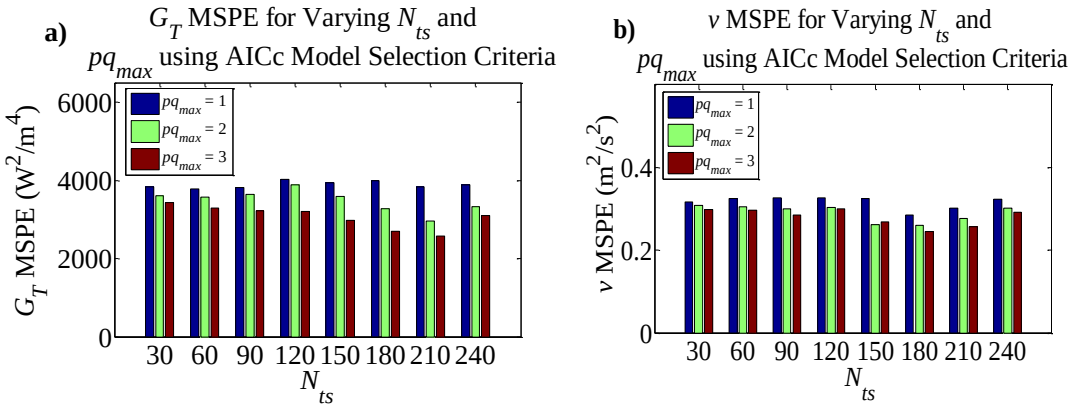

Figure B.2 Mean square prediction error (MSPE) after varying the maximum allowable ARIMA model orders (pq_{max}) and data window size (N_{ts}) with the AICc model selection criteria for **a)** Solar irradiance (G_T); and **b)** wind speed (v). The best pq_{max} for G_T and v ARIMA predictive models is 3.

Appendix C

CATALOG OF STATIC AND DYNAMIC OMNI-CHARGER DOE RESULTS

Fig. C.1 provides all 16 of the remaining static and dynamic OMNi-Charger DoE results not mentioned in Section 5.5. Note that some tests may be redundant (i.e., they show similar controller behavior since the same state was observed), but all tests confirm our conclusion that the OMNi-Charger controller performs adequately as expected under each state and when changes between states occur.

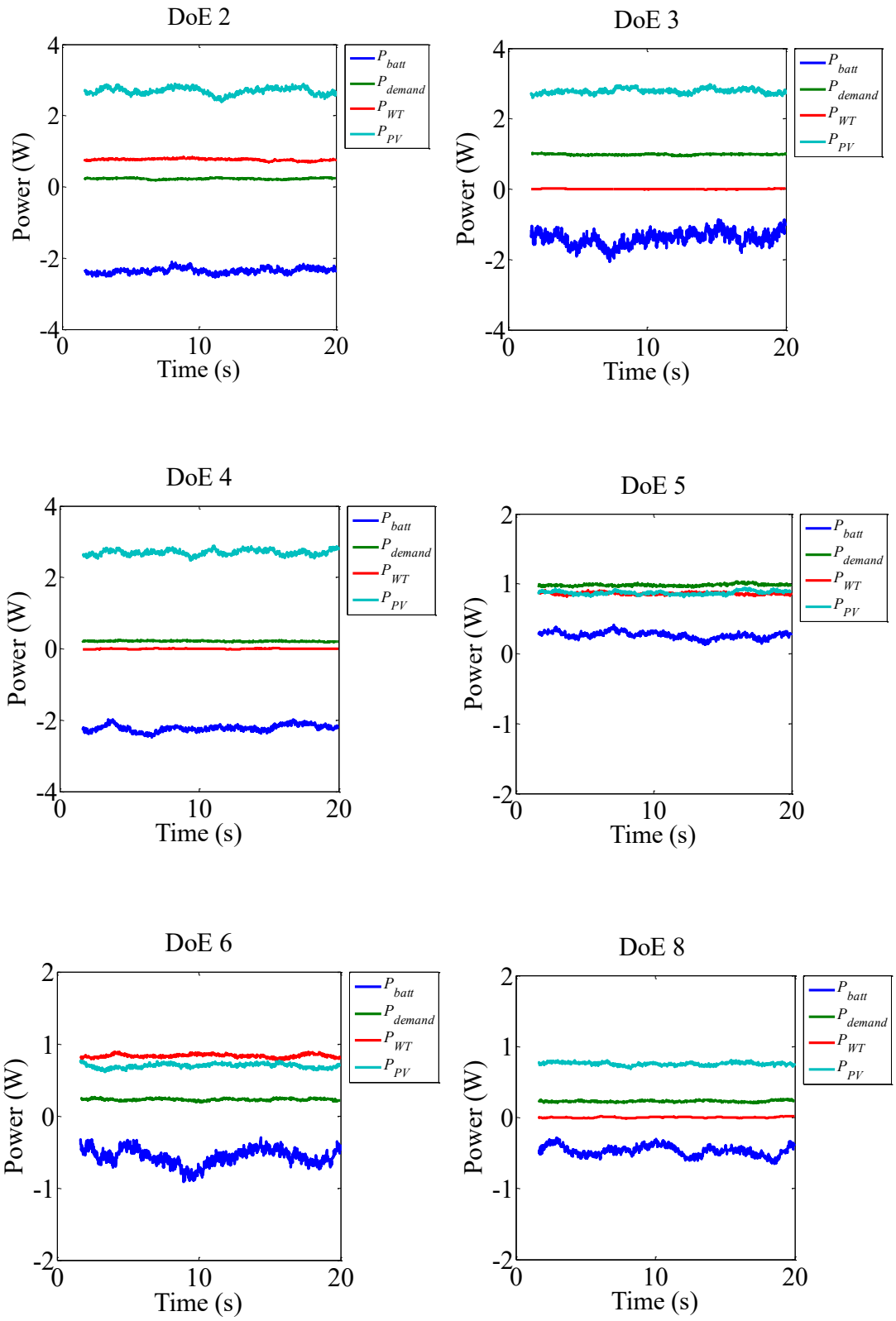
DoE 2
DoE 3
DoE 4
DoE 5
DoE 6
DoE 8
Power (W)
Time (s)
P_{batt}
P_{demand}
P_{WT}
P_{PV}

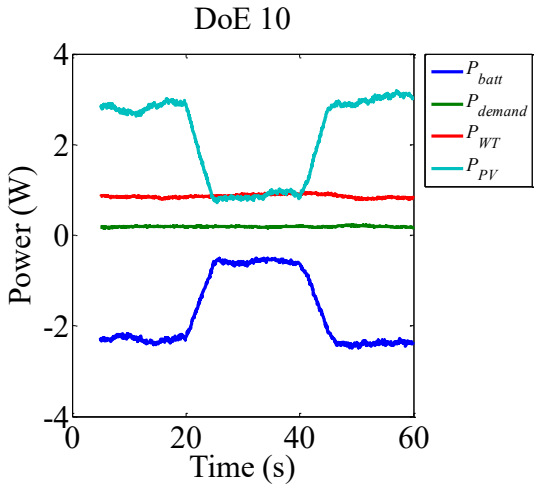
DoE 10
Power (W)
Time (s)
P_{batt}
P_{demand}
P_{WT}
P_{PV}

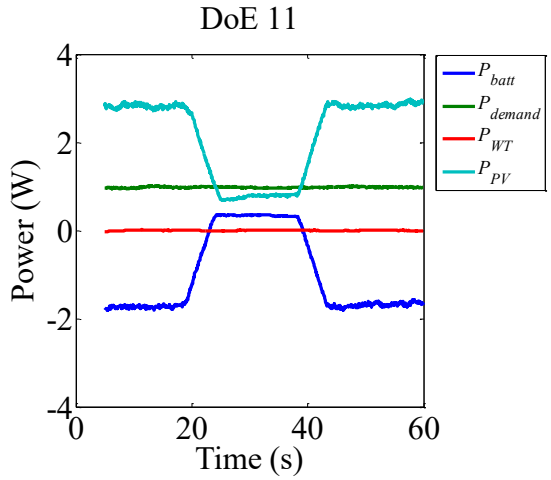
DoE 11
Power (W)
Time (s)
P_{batt}
P_{demand}
P_{WT}
P_{PV}

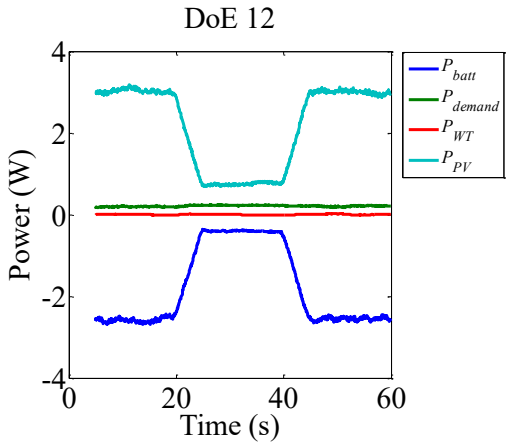
DoE 12
Power (W)
Time (s)
P_{batt}
P_{demand}
P_{WT}
P_{PV}

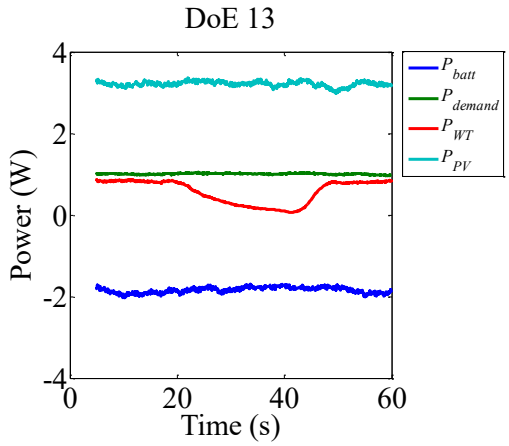
DoE 13
Power (W)
Time (s)
P_{batt}
P_{demand}
P_{WT}
P_{PV}

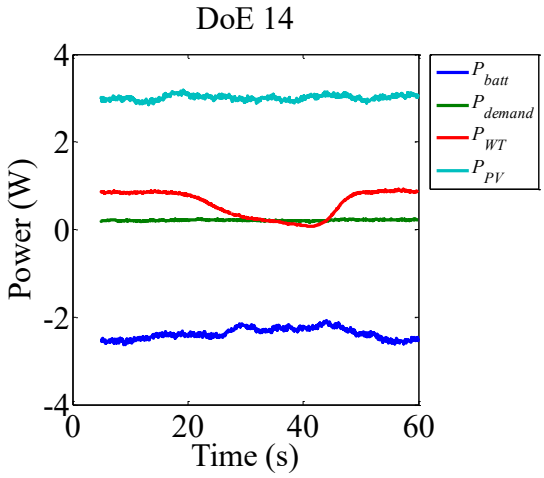
DoE 14
Power (W)
Time (s)
P_{batt}
P_{demand}
P_{WT}
P_{PV}

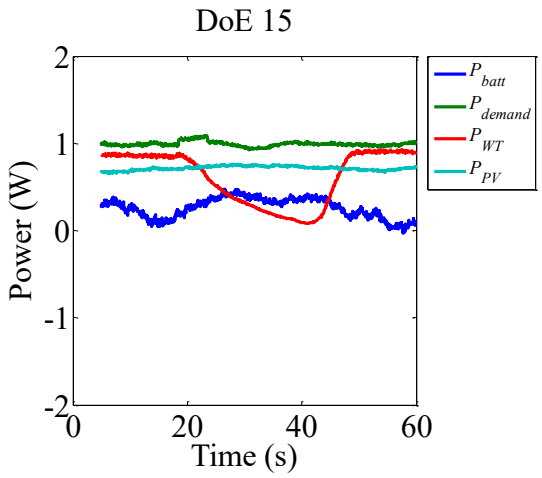
DoE 15
Power (W)
Time (s)
P_{batt}
P_{demand}
P_{WT}
P_{PV}

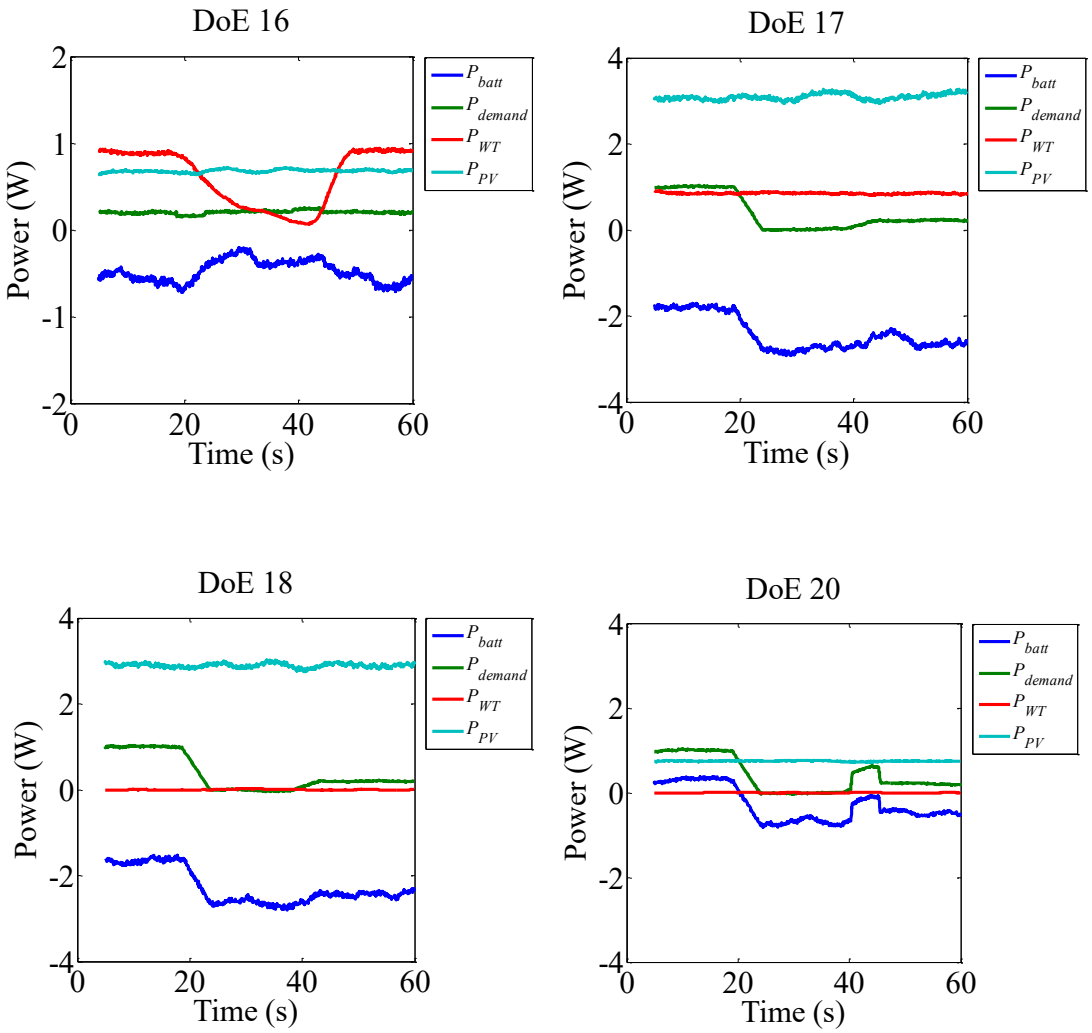

Figure C.1 Remaining static and dynamic OMNi-Charger DoE results. All results show that the power demand is satisfied and excess power, when available, is stored in the battery. Therefore, the OMNi-Charger controller functionality was successfully proven.